

FIBER BASED TOOLS FOR POLISHING OPTICAL MATERIALS

by

Hossein Shahinian

A dissertation submitted to the faculty of
The University of North Carolina at Charlotte
in partial fulfillment of the requirements
for the degree of Doctor of Philosophy in
Mechanical Engineering

Charlotte

2018

Approved by:

Dr. Brigid Mullany

Dr. Christopher Evans

Dr. Harish Cherukuri

Dr. Wesley Williams

Dr. Mohammad Kazemi

©2018
Hossein Shahinian
ALL RIGHTS RESERVED

ABSTRACT

HOSSEIN SHAHINIAN. Fiber based tools for polishing optical materials. (Under the direction of Dr. BRIGID MULLANY)

In this dissertation, the development of alternative fiber based polishing tools for the finishing of precision freeform and aspherical optics is introduced. Freeform and aspherical optics, i.e. optics with varying radius of curvatures (ROC), are the current forefront for solutions for modern optical systems, enabling more compact and higher performance designs than possible with systems composed of classical optical components, i.e. planar and spherical optics. The technological challenges associated with the fabrication of freeform optics include; (1) identification of suitable tooling capable of accommodating the different ROC's, and (2) achieving surfaces with low mid spatial frequency (MSF) error content. The mainstream fabrication techniques for freeform optics heavily rely on a process called sub-aperture polishing, whereby a tool (down to 1/10th of the optic size), is programmatically traversed across the surface to finish the part. This technique, due to the remnant tool path marks, results in MSF errors on the optic's surface. Removal of MSF errors is an ongoing challenge in the optics industry. As the main contribution of this work, it will be shown that fiber based tools, which have the flexibility to conform to varying ROCs, have the potential to remove preexisting MSF errors. The other contributions of this work are as follows: (1) Favorable fiber characteristics for use in the proposed fiber based tools are isolated. (2) The material removal mechanism associated with fiber based tools is described. (3) Finite element models (FEM) are created to gain insights on the fundamental fiber-workpiece interaction, and on the fiber properties and geometries most suited for MSF reduction. (4) The initial steps of implementing fiber

based tools in commercial, multi axis optic finishing machines are completed and the associated challenges identified.

In summary, this work lays the foundation for using fiber based tools to reduce MSF's on freeform surfaces, and in doing so, the work addresses a critical need as identified by the optical fabrication community.

ACKNOWLEDGMENTS

Throughout my 3 years of work upon completion of this dissertation a lot of great people have contributed that I feel in full debt of them and I would like to take this opportunity to acknowledge their contributions. First and foremost, Dr. Brigid Mullany, my PhD supervisor, had undeniably the biggest impact on both developing me as a researcher as well as a person, in the past 3 years. I am sincerely grateful for her significant contributions as well as her stellar mentorship for my PhD work. Her excellent insights and knowledge in polishing as well as incredible training in enhancing attention to details and critical thinking has been very pivotal in my transition from a student to a researcher. My work with Dr. Mullany has been full of respect and professionalism, and it has been a great pleasure to have the opportunity to work with her. Dr. Christopher Evans, whom his transcending mentorship provoked a lot of thoughts and ideas as well as his invaluable experience in optical fabrication and testing has been a significant guiding torch for my understanding of the physics of optical polishing and surface characterization. I was very lucky to have the opportunity to work with Dr. Evans on various projects in UNCC to gain experience and education on the science of metrology as well as optics. Dr. Harish Cherukuri, unquestionably had been my main mentor in the finite element modeling of my work, and I had the opportunity to directly work with him and learn a lot about different aspects of the finite element modeling of this work. I also had the opportunity of direct collaboration on multiple articles with Dr. Cherukuri and solving many of the project problem with invaluable insights from him. I am very grateful to Dr. Wesley Williams and Dr. Mohammad Kazemi for their time and kind consideration on being part of my PhD committee. Dr. Russell Keanini, whom I had the opportunity to work on a different project,

has been not just a great mentor but a close and kind friend that provided unforgettable help in my transitioning period in graduate school. I had the great chance to meet with Dr. John Taylor, whom he was visiting UNCC for a year from LLNL. John has a breadth of knowledge in mechanical and optical engineering. He not only was a great mentor to me, but I built a very close friendship with him and has been a strong advocate of me. Dr. Mohammed Hassan, joined our group in the later stages of my project, but with his great contributions, we were able to greatly improve the flaws of my initial FE modeling. Dr. Peter Tkacik, was of great help in my involvement in the vibratory finishing research work. Jayesh Navare, former UNCC graduate, whom gave me the opportunity to provide a mentorship role to him as well as his hard work in vibratory finishing group. Dr. Matthew Davies, Dr. Joseph Owen, Dr. John Troutman, and Daniel Barnhardt as part of the UNC Charlotte's Diamond Turning lab, were integral in the progress of this work by providing diamond machined germanium samples. Mr. Eric Browy, former UNCC graduate student, and Dr. Mohammed Mainuddin, both provided training and insights on running polishing machines and experiments. The incredible faculty, staff, and fabulous infrastructure of the Center for Precision Metrology (CPM) for enabling me to do my work in UNCC. Dr. Jimmey Miller, Mr. Greg Caskey, Mr. Joseph Dalton, Mr. Brian Dutterer, Mr. John Brian, have all provided great help toward the completion of my work.

This Research was supported by the NSF I/UCRC Center for Freeform Optics (IIP-1338877 and IIP-1338898), and partially supported by NSF's IR/D program. I would like to acknowledge the significant help and support of Center for Freeform Optics (CeFO), for providing the financial support for the project. As an industrial member of CeFO, Mr. Mike Bechtold, president, and Mr. Edward Fess, head of R&D, of OptiPro Systems were a pillar

of support and great help throughout the project. With their and Mr. Josh Torres's kind help, I had a full week of testing the end product of this work on OptiPro machines. Mr. William Gemmill from Eminess Technologies, was of great help and support with his excellent knowledge on the chemistry of different polishing slurries. Dr. Flemming Tinker from Aperture Optical Sciences had also been an advocate and source of support and knowledge for polishing freeform optics and dealing with mid-spatial frequency errors.

I would like to express my warmest gratitude to the UNCC Mechanical Engineering community from the very kind faculty members, Dr. Ron Smelser, Dr. Scott Kelly, Dr. Tony Schmitz, and Dr. Garry Hodgins, whom they have been of great mentors and indispensable help to my gain of knowledge at UNCC. The fantastic staff of the ME department of UNCC, Mrs. Jennifer Chastain, Mrs. Tracy Beauregard, Mrs. Marion Cantor, Mrs. Lebra Nance, who their very kind help made my administrative works look much easier than it was.

It goes without saying that my friends and colleagues in and outside the ME department both enabled me to learn new things every day and making the graduate work fun. Todd and Erin Noste, Farzad Azimi, Brittney and Nathan Lambert, Shima Ziaei Zachary Reese, Clark Hovis, Dr. Kang Ni, Yue Peng, Nicholas Sizemore, Dustin Gurganos, Hossein Hemmati, and Milad Shabanian, and many others were the counter weight to my work life and bringing a balance that I very much appreciated.

My final thoughts belong to my loving parents, Mina and Fazel, who were there for me no matter what. I can't thank them enough and their unwavering support was the main foundation supporting me and driving me forward.

TABLE OF CONTENTS

LIST OF TABLES	xiv
LIST OF FIGURES	xv
LIST OF ABBREVIATIONS	xx
CHAPTER 1: INTRODUCTION	1
CHAPTER 2: LITERATURE REVIEW	5
2.1 Polishing optical components	5
2.1.1 Ancient era	5
2.1.2 Modern era	5
2.2 Conventional Optics vs Freeform and Aspherical Optics	6
2.3 Polishing Configurations	8
2.3.1 Full-aperture polishing	9
2.3.2 Sub-aperture polishing	10
2.4 Polishing Components and the Physics of Material Removal	12
2.5 Deterministic Finishing	16
2.6 Surface Characterization of Optical Components	19
2.6.1 Form or figure	20
2.6.2 Roughness or finish	22
2.6.3 Waviness or mid-spatial frequencies (MSF)	24
2.7 Available Solutions for MSF Reduction	28
2.8 Summary	33
CHAPTER 3: FIBER TOOL DESIGN, FABRICATION, AND TESTING	34

3.1 Introduction	34
3.2 Fiber Selection Criteria	34
3.3 Fiber Selection Test Bed	35
3.4 Fiber Based Tool Design and Fabrication	38
3.5 Fiber – Workpiece FE Modeling	40
3.5.1 Nylon 6/6 fiber	41
3.5.2 Glass workpiece	41
3.5.3 FEM steps and boundary conditions	42
3.5.4 Meshing scheme and number of elements	43
3.5.5 Model results (planar workpiece)	44
3.5.6 Model results (non-planar workpiece)	46
3.6 Summary	47
CHAPTER 4: MATERIAL REMOVAL TESTING AND MECHANISMS	49
4.1 Introduction	49
4.2 Polishing Tools	49
4.3 Polishing Experimental Testbed	50
4.4 Workpiece Samples	51
4.5 Polishing Slurries	52
4.6 Supporting Metrology	52
4.6.1 Measuring volume of removed material and process widths	53
4.6.2 Surface roughness	53
4.7 Material Removal from Planar BK7 Samples	54
4.7.1 MRR of fiber based tools using different fibers	55

	x
4.7.2 MRR of the Nylon 6/6 fiber vs process kinematics (load and velocity)	58
4.7.3 MRR/fiber of fiber based tools vs fiber number/tool	60
4.8 Fiber Based Tools Material Removal Mechanism	61
4.8.1 Process width of the Nylon 6/6 fiber vs slurry abrasive particle size	63
4.8.2 Fiber preferential impact on periodic surface features	65
4.9 MR of the Nylon 6/6 Fiber Using FT-1, FT-2, and FT-3 Tool Designs	67
4.10 Surface Finishes Achievable with Fiber Based Tools	71
4.11 Fiber Based Tools Long Term Load Decay and Fiber Wear	72
4.12 Summary	75
CHAPTER 5: FIBER BASED POLISHING PROCESS	77
5.1 Introduction	77
5.2 Experimental Setups	77
5.2.1 3-axis CNC (submerged slurry bath)	77
5.2.2 5-axis CNC (inline slurry delivery)	78
5.3 Workpiece Samples	79
5.4 Supporting Metrology	80
5.5 Fiber Based Tools Translation on Planar Glass	80
5.6 Fiber Based Tools Behavior Near Workpiece Edge	82
5.6.1 Fiber disengagement and reengagement assessment	82
5.6.2 Quantitative evaluation of the twelve fiber Nylon 6/6 tool roll-off effects	83
5.7 Material Removal with Tool Translation in the Slurry Bath	86
5.7.1 Evaluation of total MR and MR profile shape of the tool with translation	88
5.7.2 Evaluation of Tool induced form and MSF errors	90

	xi
5.8 Material Removal in the Inline Slurry Delivery Configuration	93
5.8.1 Spot tests on planar samples	93
5.8.2 Spot tests on non-planar sample	94
5.8.3 Evaluation of total MR and MR profile shape of the tool with translation	95
5.8.4 Evaluation of MR volumes during spiral polishing on planar sample	97
5.8.5 Evaluation of MR volumes during spiral polishing on non-planar sample	101
5.9 Measured Surface Finishes and a Predictive Model	102
5.10 Summary	107
CHAPTER 6: MSF ERROR REDUCTION WITH FIBER BASED TOOLS	109
6.1 Introduction	109
6.2 MSF Reduction of Fiber Based Tools Theory	109
6.3 Fiber-MSF FE Modeling	110
6.3.1 Fiber Young's modulus	112
6.3.2 Fiber cross section geometry	113
6.3.3 Fiber second moment of the cross section	114
6.3.4 MSF feature wavelength	116
6.4 Experimental Setups and Testing Samples	116
6.5 Metrology	118
6.6 MSF Reduction Spot Tests	119
6.6.1 Twelve fiber Nylon 6/6 tool MSF reduction (fiber diameter = 1.6 mm)	119
6.6.2 Fifty-six fiber PET tool MSF reduction (fiber diameter = 0.22 mm)	120
6.7 MSF Reduction Tests Under Translational Conditions	122
6.7.1 MSF reduction from germanium with premade sinusoidal MSF features	122

6.7.2 MSF reduction from germanium with premade cusp features	124
6.8 MSF Reduction During Full Raster Polishing	125
6.9 MSF Reduction Testing on MSF Features with $\lambda = 2 \text{ mm}$	128
6.10 Alternative Fiber Design for More Efficient MSF Reduction	130
6.11 Summary	133
CHAPTER 7: CONCLUDING REMARKS AND FUTURE DIRECTIONS	135
7.1 Key Findings	136
7.1.1 Tooling and fibers	136
7.1.2 Fiber based tools material removal mechanisms	136
7.1.3 Fiber based tools MSF reduction	138
7.1.4 Tool integration in multi axis CNC machines	138
7.1.5 Predictive FE modeling	138
7.2 Future Directions	140
7.2.1 Tool and fiber design	140
7.2.2 Process optimization	141
REFERENCES	144
APPENDIX A: METROLOGY INSTRUMENTS	158
A.1 Taylor Hobson Talysurf 120-L	158
A.2 Zygo Laser Fizeau Interferometer AT1000	159
A.3 Zygo ZeGage	160
APPENDIX B: ZERNIKE POLYNOMIALS	163
B.1 Mathematical Form	163

	xiii
APPENDIX C: DR. CHERUKURI AND DR. HASSAN'S MODEL	166
APPENDIX D: MATLAB CODES GUIDE	168
D.1 Zygo Fizeau Measurement Data Processer (.dat)	168
D.2 Subtractor	169
D.3 Zygo SWLI Measurement Data Processor (.dat)	169
D.4 Profilometer Measurement Data Processor (.MOD)	170
D.5 Convolution code	171
APPENDIX E: PUBLICATIONS, PATENT, AND PRESENTATIONS	172
E.1 Publications from Dissertation Work	172
E.2 Presentations on Dissertation Work	172
E.3 Patent	172
E.4 Other Publications in UNCC	173

LIST OF TABLES

Table 2-1 Deterministic finishing processes	17
Table 3-1 Fiber evaluation summary results for fiber length of 37.5 mm	37
Table 4-1 Tools used for the MRR vs fiber type experiments	56
Table 4-2 Testing conditions for evaluation of MRR vs fiber type	56
Table 4-3 Testing conditions for evaluation of MRR of the twelve fiber Nylon 6/6 tool vs process kinematics	58
Table 4-4 Fiber based tools used for testing MRR/fiber vs fiber number/tool	60
Table 4-5 Polishing slurries used for quantifying the process width vs particles size of the abrasives	63
Table 4-6 Testing conditions for polishing BK7 glass using twelve fiber Nylon 6/6 tool for evaluation of the process widths vs slurry particle size	64
Table 4-7 Testing conditions for the Nylon 6/6 fiber with three different tool designs	68
Table 5-1 Tools tested under translational conditions on float glass	81
Table 5-2 Testing conditions for evaluation of edge roll-off effects of the twelve fiber Nylon 6/6 tool on planar float glass	85
Table 6-1 Fiber properties used for the two-step fiber-MSF FEM	112
Table 6-2 Full raster MSF reduction testing with the twelve fiber Nylon 6/6 tool	126
Table 6-3 Fiber deflection VS dumbbell diameter	133

LIST OF FIGURES

Figure 1-1 Fiber tool concept; (a) globally compliant (b) locally stiff	3
Figure 2-1 Planar and spherical optics vs aspherical and freeform optics	6
Figure 2-2 (a) Application of freeform optics to the illumination of a gas station [13] (b) application of a freeform mirror in a car side mirror [14]	8
Figure 2-3 Polishing process configurations; (a) full-aperture polishing (b) sub-aperture polishing	10
Figure 2-4 (a) Tool and freeform workpiece curvature mismatch (b) uneven pressure distribution of tool near workpiece edge	11
Figure 2-5 (a) Polishing process overview (b) close up of the 3-body interaction	12
Figure 2-6 Possible material removal mechanisms during polishing [27]	13
Figure 2-7 Deterministic finishing process map	18
Figure 2-8 (a) Bonnet polishing tool [61] (c) MRF system [62]	18
Figure 2-9 (a) Form, (b) waviness and (c) roughness errors for a “planar” workpiece	20
Figure 2-10 (a) The influence of figure on a planar wavefront, (b) close up of the surface geometry and the extent of figure error	21
Figure 2-11 (a) “perfect” imaging of a point source (b) “real” diffracted spot image	25
Figure 2-12 The effect of figure, finish, and MSF errors on PSF [95]	26
Figure 2-13 (a) PSF of an optic with no MSF features (b) PSF of an optic with MSF features with a period of 2 mm and RMS of 35 nm	26
Figure 2-14 Polishing MSF errors; (a) from planar (b) from spherical workpiece	28
Figure 2-15 Optimax VIBE finishing process [112]	29
Figure 2-16 Conventional polishing tool paths	30
Figure 2-17 Non-conventional polishing tool paths; (a) pseudo random tool path [114] (b) Hilbert path and modified Hilbert path [117]	31
Figure 2-18 The FADP tool [118]; (a, b) planar and spherical tool configuration (c, d) pre and post the removal of MSF errors	31

Figure 2-19 Float polishing [121] (a) schematic, (b) machine in action	32
Figure 3-1 Fiber selection test bed (a) fiber disengaged, (b) fiber engaged	35
Figure 3-2 Fiber selection test bed examining the Nylon 6/6 fiber	36
Figure 3-3 Fiber based tool initial designs; (a) FT-1 design (b) FT-2 design	39
Figure 3-4 Fiber based tool FT-1 design attached to the Bridgeport milling machine; (a) disengaged, and (b) engaged with workpiece	40
Figure 3-5 Nylon 6/6 fiber stress/strain curve [123]	41
Figure 3-6 Fiber-workpiece interaction FEM steps	42
Figure 3-7 Fiber and workpiece overall meshing and close-up of the finer elements	44
Figure 3-8 Nylon 6/6 fiber-workpiece interaction FEM (a) contact pressure distribution (CPRESS), (b) pressure profile extracted from CPRESS along the dashed line	45
Figure 3-9 FEM of the tilted Nylon 6/6 fiber at 40° (a) contact pressure distribution (CPRESS), (b) pressure profile extracted from CPRESS along the dashed line	46
Figure 3-10 FEM of the Nylon 6/6 fiber-concave workpiece interaction; (a) contact pressure distribution (CPRESS), (b) pressure profile extracted from CPRESS along the dashed line	47
Figure 4-1 Fiber based tool designs (a) FT-1, (b) FT-1 with inline slurry feed (c) FT-2 (d) FT-3	50
Figure 4-2 Polishing testbed; (a) schematic of a tool engaged with workpiece in the slurry bath (b) actual tool in contact with a planar surface	51
Figure 4-3 Material removal from BK7 glass using thirteen fiber Nylon 6/6 tool; (a) Fizeau interferogram (b) radially averaged profile of the Fizeau interferogram	54
Figure 4-4 Normalized MRR/fiber of the fiber based tools listed in Table 4-1	57
Figure 4-5 MRR vs Load \times Velocity of the twelve fiber Nylon 6/6 tool	59
Figure 4-6 MRR/fiber for tools with different fiber number/tool listed in Table 4-4	61
Figure 4-7 (a) fiber – workpiece engagement (b) fiber – workpiece contact close up in the absence of abrasive particles (c) fiber – workpiece – particle interaction and the impact of particle size on process width i.e. Effective Contact	62
Figure 4-8 Process width vs particle size for 12-fiber Nylon 6/6 tool	64

Figure 4-9 Fiber interaction with BK7 sample contacting concentric sinusoidal features; (a) BK7 sample interferogram, (b) fiber interaction with the sinewave, (c) fiber interaction with the sinewave and two different particle sizes close-up	65
Figure 4-10 Peaks vs valleys surface roughness of the sinusoidal features, pre and post the polishing of the BK7 sample	66
Figure 4-11 SWLI measurements of the BK7 sample containing the sinusoidal features; (a) sample peak (b) sample valley of the sinewave	67
Figure 4-12 (a) MR spot for the FT-1 tool, (b) MR spot for the FT-2 tool	68
Figure 4-13 View from bottom of the engaged tools; (a) FT- tool (b) FT-3 tool	69
Figure 4-14 MR spot and comparison of tool foot print size; (a) FT-1 tool, (b) FT-3 tool	70
Figure 4-15 BK7 surface finish (a) before polishing, after polishing with (b) FT-1-3 (Tfiber) (c) FT-1-2 (Nylon 6/6) (d) FT-1-6 (composite) (e) FT-1-1 (Copolymer)	71
Figure 4-16 Load decay of the twelve fiber Nylon 6/6 tool over continuous polishing experiment	73
Figure 4-17 Nylon 6/6 fiber SWLI measurement; (a) unused fiber (b) worn fiber (after 5.5 hours) (c) profile across the dashed line on the worn fiber	74
Figure 5-1 3-axis CNC setup; (a) Haas TM-1 machine tool, (b) test setup close-up (c) twelve fiber Nylon 6/6 tool engaged with planar workpiece	78
Figure 5-2 5-axis CNC setup (a) OptiPro Triumph machine (b) twelve fiber Nylon 6/6 tool engaged with concave workpiece	79
Figure 5-3 Twelve fiber Nylon 6/6 tool – workpiece edge interaction; (a, b) successful fiber reengagement (c) unsuccessful fiber reengagement	82
Figure 5-4 Nylon 6/6 tool MR profile near edge (a) with no fiber overhang (b) “ideal” scenario with tool overhang.	83
Figure 5-5 Nylon 6/6 fiber FEM near workpiece edge (a) 0 mm fiber overhang, (b) 3 mm fiber overhang, (c) 5 mm fiber overhang	84
Figure 5-6 Twelve fiber Nylon 6/6 tool near edge removal profiles for tool overhangs of (a) 0 mm, (b) 3 mm, and (c) 5 mm	86
Figure 5-7 Polishing slurry bath setup (a) reciprocal tool path (b) raster tool path	88

Figure 5-8 MR data of the twelve fiber Nylon 6/6 tool during translation and linear extracted profiles (dashed line) from the MR data; (a) prediction from convolution (b) experimental outcome	89
Figure 5-9 Full raster polishing BK7 with the twelve fiber Nylon 6/6 tool; (a) subtraction map containing the imparted form error (b) PSD of the before and after polishing data	91
Figure 5-10 Zernike decomposition of the tool induced form error (a) RV part (b) RI part.	93
Figure 5-11 The twelve fiber Nylon 6/6 tool on the concave surface (a) FEM pressure profile (b) experimental MR spot profile	95
Figure 5-12 MR data and linear extracted profile of the Nylon 6/6 tool during translation on BK7 glass; (a) prediction from convolution (b) experimental outcome	97
Figure 5-13 Spiral raster polishing configuration and MR profile change with tool position (a) tool at center (b) tool at the edge	98
Figure 5-14 Top view of the spiral polishing configuration and the tool kinematics	99
Figure 5-15 Spiral polishing of planar BK7 glass interferogram and extracted profiles; (a) predicted by convolution, (b) measured experimental outcome	100
Figure 5-16 Spiral polishing of concave BK7 glass interferogram and extracted profiles; (a) from convolution (b) experimental outcome	101
Figure 5-17 Stitched SWLI measurement of BK7 glass during reciprocal path polishing	103
Figure 5-18 Fiber-abrasive-workpiece interaction snapshot; (a) front view of tool engaged with workpiece (b) close-up view of fiber particle engagement (c) top-view coordinates of the tool	104
Figure 5-19 (a) actual surface measurement (b) fiber trace simulation	106
Figure 5-20 (a) Interferogram of BK7 sample polished with Nylon 6/6 tool (b) 20× SWLI measurement of the zone of study (c) simulated surface of the zone of study	107
Figure 6-1 (a) Fiber based tool interaction with a freeform containing MSF features (b) close-up of scenario of a fiber with significant local deflection (undesired) (c) close-up of a scenario of a fiber with negligible deflection (desired)	110
Figure 6-2 Fiber-MSF FEM; Step 1 and Step 2	111
Figure 6-3 $\varnothing 1.6$ mm fiber deflection to MSF's vs fiber Young's modulus	113

Figure 6-4 Fiber deflection to MSF's vs fiber cross section geometry	114
Figure 6-5 FE contact pressure distribution (CPRESS) for different fiber geometries	114
Figure 6-6 Max fiber deflection VS second moment of the cross section	115
Figure 6-7 MSF reduction testing with the Nylon 6/6 tool with no tool translation; (a) before polishing surface profile (b) after polishing surface profile (c) PSD of the before and after polishing profiles	120
Figure 6-8 MSF reduction testing with the PET tool with no tool translation; (a) before polishing surface profile (b) after polishing surface profile (c) PSD of the before and after polishing profiles	121
Figure 6-9 MSF reduction testing on germanium; measured profiles (a) perpendicular and (b) parallel to the polishing tool path. PSD of the measured profiles (c) perpendicular and (d) parallel to the polishing tool path	123
Figure 6-10 Fizeau interferogram of MSF sample with cusps; (a) pre polishing (b) post polishing	125
Figure 6-11 (a) Linear slice data δz from the Fizeau interferograms (b) radially averaged PSD of the Fizeau interferograms	125
Figure 6-12 MSF reduction from germanium during full raster polishing (left) linear 1-D profiles from the from Fizeau measurements (right) radially averaged PSD of the Fizeau measurements	127
Figure 6-13 MSF reduction from BK7 glass; (a) linear profile from Fizeau measurement (b) radially averaged PSD of the measurement	129
Figure 6-14 Fiber combo concept	131
Figure 6-15 (a) Nylon 6/6 fiber (b) modified dumbbell Nylon 6/6 fiber	131
Figure 6-16 FEM pressure profiles (a) Nylon 6/6 fiber (b) Nylon 6/6 fiber with the dumbbell section	132
Figure 7-1 Fiber based polishing process map	143

LIST OF ABBREVIATIONS

BK7	Borosilicate glass
CA	Clear aperture
CNC	Computer numerical controlled
FEA	Finite element analysis
FEM	Finite element model
FOV	Field of view
LLNL	Lawrence Livermore National Lab
MR	Material removal
MRF	Magnetorheological finishing
MRR	Material removal rate
MSF	Mid spatial frequency
PSD	Power spectral density
PV	Peak to valley
RI	Rotationally invariant
RMS	Root mean square
ROC	Radius of curvature
RPM	Revolution per minute
RV	Rotationally varying
SSD	Sub surface damage
SWLI	scanning white light interferometer
TIF	Tool influence function

CHAPTER 1: INTRODUCTION

This work is about the design and evaluation of fiber based polishing tools capable of removing material from optical materials and, most importantly, reducing the magnitude of mid spatial frequency (MSF) features on both classic (planar and spherical) and freeform optical components.

The use of hard materials, such as glass and silicon carbide (SiC), in the optics manufacturing, is very common place. While rough and fine grinding is used to generate the geometric form of the optic, polishing is an indispensable final step in the process chain. The polishing process is responsible for improving the final figure and finish of the fabricated optical component to within the tolerances of its specifications.

The classical optics, mainly were optics with constant radii of curvature, i.e. planar or spherical. With the advent of computerized numerical control (CNC) machines, easy fabrication of optics with variable radii of curvature, i.e. freeforms and aspheres, became feasible. These optics, offer great advantages over their classical counterparts. They expand the optical system design space and enable the designers to realize much more compact systems. On the fabrication side, many technologies for manufacturing these optics have been introduced over the years. The key technology behind the fabrication of freeform optics is the sub-aperture polishing process. In this process a tool smaller than the workpiece ($\sim 1/10^{\text{th}}$ of the workpiece), is deterministically translated over the optic. The tool is given a specific dwell time for each point on the programmed path. This dwell time depends on the amount of localized material removal (MR) needed for achievement of a

part with geometrical errors less than the given tolerances. Conventional polishing pads and pitch tools struggle to conform to variable radius of curvatures (ROC) on a surface. Consequently, this will result, in either non-processed zones, or zones that are processed in the presence of uneven pressure distributions. The unevenness of the applied loads of the tool, can give rise to unpredicted MR of the workpiece and the inducement of errors thereafter. Unfortunately, most of the deterministic technologies employed to fabricate freeforms induce MSF errors on their end product. MSF errors are geometrical errors on the surface that are repeated with a given period (λ) somewhere between 3 mm and 0.08 mm, and an amplitude (PV) of approximately 100 nm. They are effectively the remnant the tool path raster marks resulting from the non-uniform tool MR profiles. These errors decrease the performance of the optical components significantly and limit the range of the operating electro-magnetic wavelength to and above the infrared region of the spectrum (wavelengths $> 1 \mu\text{m}$).

The optics manufacturing community have actively sought for solutions to reduce the MSF errors on freeforms and aspheres. Yet, no definitive solution is available in the literature. Those published are mostly extensions of a current technology or an incremental improvement on a formerly implemented method. The absence of solutions for removing MSF errors from freeform and aspherical optics, was the main motivation to explore a completely different and never tried before approach, of using fiber based polishing tools. The supporting logic for trying fiber-based polishing tools, is that it is expected that the global compliance of the fibers enables the tools to conform to a variety of workpiece forms, i.e. aspheres and freeforms, while the fibers remain locally stiff to the MSF errors,

see Figure 1-1. This tooling configuration should promote preferential MR from the high points of the MSF features, and ultimately reduce the magnitude of the errors.

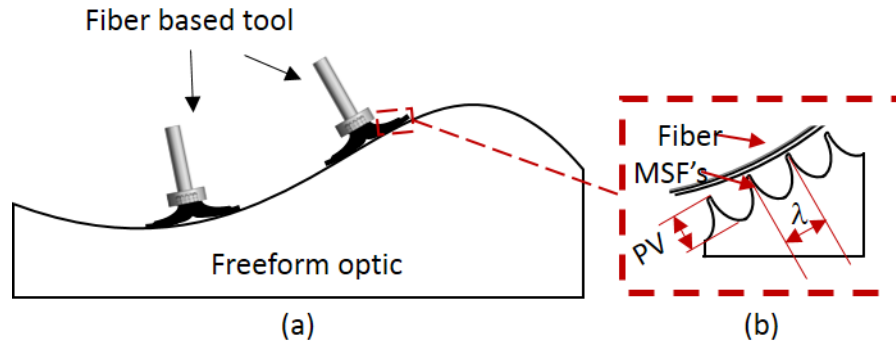


Figure 1-1 Fiber tool concept; (a) globally compliant (b) locally stiff

To best of the author's knowledge, this work is the first implementation of fiber based tools in a precision polishing application. This dissertation outlines the material removal mechanics of these tools whereby key process parameters and their impact on the polishing outcomes are identified. A finite element (FE) based foundation to assist in future tool design is introduced. Most importantly, it is demonstrated that these tools have the potential to reduce preexisting MSF errors.

Chapter 2 provides a broad background about finishing processes in optics manufacturing. The focus of the discussion will be on freeform and aspherical component fabrication. Examples of their wide application in the industrial world will also be listed. Information will be provided regarding optics specifications and available mathematical tools for the characterization of these components. This discussion will have a special emphasis on the MSF's and their impact on the optical performance.

In chapter 3, the initial steps in design, fabrication, and characterization of fiber based tools are described. Two different approaches, experimental and FE simulations, are

employed to reach this goal. Fiber types qualified by both the experimental test bed and the FE model are used in the fabricated fiber based polishing tools.

Chapter 4, contains details on the polishing tests conducted on planar BK7 glass samples. The test results in this section demonstrates the ability of these tools to remove material from glass under different testing conditions. The main process parameters impacting the polishing outcomes (MR rates and surface finish) are identified. An understanding of the fiber – abrasive – workpiece interaction is introduced.

Chapter 5 scopes a more practical perspective; integration of the tools into a commercial 5 axis polishing machine and the resulting challenges. These issues include, long term polishing response of the tool, as well as its performance near the edge of the workpiece. The stability of the tool's material removal footprint over long polishing runs is investigated. Lastly, initial testing results on non-planar samples will be presented. These tests took place onsite OptiPro Systems located in Rochester, NY.

In Chapter 6, the ability of fiber based tools to reduce MSF features is demonstrated. This chapter includes results with respect to the reduction of MSF features from planar surfaces under different testing conditions. An additional two-step FEM is introduced, to assist the identification of fibers suitable of reducing MSF features. The same model is used to explore the design of alternative novel fiber geometries. Examples of alternative fiber geometries with potentially higher efficiency in reduction of MSF features will be illustrated.

In the final chapter, chapter 7, the work is summarized and directions for further development of fiber based tools are discussed.

CHAPTER 2: LITERATURE REVIEW

2.1 Polishing optical components

2.1.1 Ancient era

It is believed that the first optical components made by mankind were polished mirrors about 8000 years ago in Çatal Höyük [1]. Çatal Höyük was located somewhere in the central southern modern Turkey [2]. The first polished lenses are dated back to 2575 BC (before Christ), in ancient Egypt. Their purpose mainly were to serve as ornaments on the Egyptian statues [1]. Primitive polishing mostly involved the use of stones rubbed against the target surface. The polishing agents were usually water or some kind of oil based fluid.

2.1.2 Modern era

In the contemporary optics industry, hard and brittle materials are abound. Grinding is usually the main process to shape the part as close to its final figure. However, the grinding process is very aggressive, and the part produced as such, will have a matt finish. Polishing, is used as a proceeding step, where quality, and specular surfaces can be produced. The mainstream polishing tools, in the modern times, is a layer of a polymeric pad or pitch material adhered to a rigid substrate, sometimes via an intermediate supporting material, e.g. foam, rubber, etc. This intermediate layer is used to control the flexibility of the polishing tool. The polishing agents used are typically a slurry containing fine abrasive particles (usually $< 1 \mu\text{m}$).

2.2 Conventional Optics vs Freeform and Aspherical Optics

Optical components are largely divided into two groups. The first group are the more conventional optics with constant radius of curvature (ROC) over their entire clear aperture (CA), i.e. planar and spherical optics (Figure 2-1 left). The CA of an optical component refers to the functional region of the optic.

The more modern optical components are optics with variable ROC across their aperture. Aspherical optics are a group of such optics that possess at least one axis of rotational symmetry. Freeform optics, contrary to aspherical optics, have typically no axis of symmetry and they, too, have varying ROC over their aperture (Figure 2-1 right).

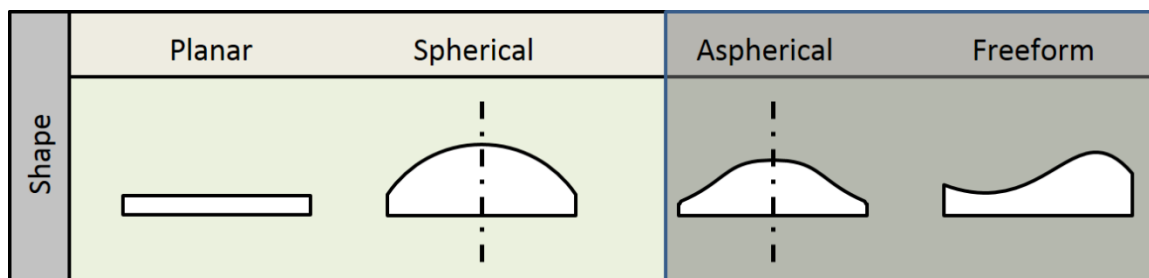


Figure 2-1 Planar and spherical optics vs aspherical and freeform optics

Planar and spherical optics have been manufactured from approximately the beginning of the 18th century in large numbers and even to-date are widely used as the main ingredient in optical systems. One main flaw of the spherical optics is the inherent third order spherical aberrations induced by such optics. These errors are typically compensated by the use of multiple components within the system.

The first use of an aspheric lens in an optical system can probably be attributed to Francis Smethwick (late 17th century) [3], in which he uses “not-spherical” glasses in his telescope and burning glasses. The term “Aspheric” seems to be coined around 1922 [4].

Although aspherical optics and conics were commonly used, prior to the 70's, easy production of such optics was nearly nonexistent. The reason for that is while fabrication of tools with constant ROC's was relatively easy, the varying ROC of the aspheres caused a lot of problems during the polishing for the aforementioned rigid tools. After the 70's emergent manufacturing, computational, and metrology capabilities promoted the use of aspheres in a wide range of industrial applications. Automotive headlighting, high power diode lasers, imaging optics, UV and EUV lithography projection lenses [5, 6] are just a few examples of systems that use aspherical optics. The main advantage of using an aspherical surface is to decrease/control the spherical aberrations, of an optical system with less components needed [7].

The application of freeform optics is more recent than aspherical optics. Jian et al. [8] have classified these surfaces into three distinct groups; (1) freeform surfaces with "steps, edges and facets", e.g. a Fresnel lens, (2) freeform surfaces containing "tessellated patterns", e.g. road signs, and (3) smooth freeform surface which lacks any steps, edges, or tessellated patterns. The term "freeform" used henceforth, refers to smooth surfaces that exploit the freeform shape. The first use of a freeform surface in an optical application can probably be attributed to Luis Alvarez. In the 1960's Alvarez came up with a design of optical lenses where their surfaces can be described in terms of third order polynomials. The use of two identical lenses with the prescribed surface can provide the system with a variable spherical power [9]. With the advances in the CNC machining and positioning, the implementation of freeform optics in optical systems design increased significantly [10]. The first commercial adoption of a freeform optical surface is attributed to the Polaroid SX-70 camera [10-12]. Freeform optics find application across the entire optics

industry. From imaging optics, e.g. in wide FOV mirrors and overhead displays, to illumination applications, e.g. high brightness LED's [11]. Figure 2-2(a) shows the application of freeform optics in the illumination optics of a gas station. The freeform optics used in this gas station have enabled a much more focused light. Figure 2-2(b) depicts how a freeform mirror can greatly enhance the FOV of a car side mirror.

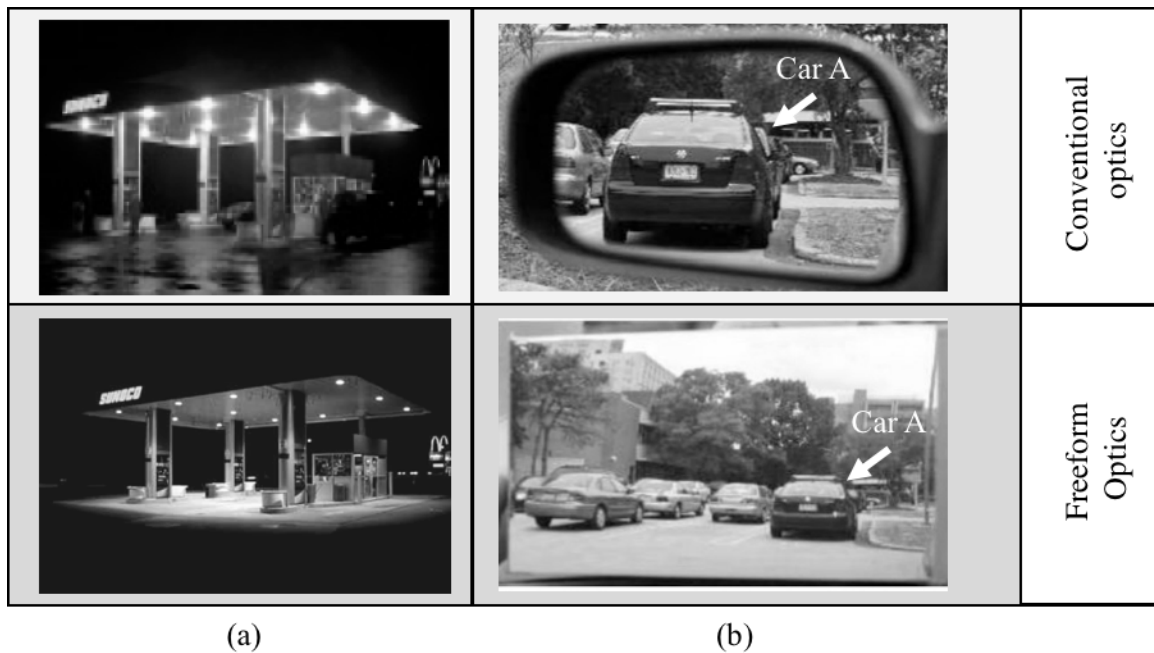


Figure 2-2 (a) Application of freeform optics to the illumination of a gas station [13] (b) application of a freeform mirror in a car side mirror [14]

2.3 Polishing Configurations

The polishing process is comprised of a polishing tool, workpiece, and polishing slurry carrying abrasive particles. The polishing is occurred as a result of the interaction of the three aforementioned components, through abrading material off the workpiece surface. In the modern industrial world, a layer of a polymeric pad [15] or pitch-based [16] material is adhered to a rigid substrate, comprising a polishing tool. The tools are used

commonly in two different configurations, known as full and sub aperture polishing configurations.

2.3.1 Full-aperture polishing

The full-aperture polishing configuration (Figure 2-3(a)) is where the polishing tool is larger than the workpiece, and ideally the ROC of the end product will be the same as the ROC of the polishing tool. As it can be seen the entire workpiece remains in contact with the polishing tool over the course of the process. This configuration is mostly limited to fabrication of parts with constant ROC i.e. planar and spherical optics. Yet there are quite a number of notable full-aperture approaches developed by different researchers that have shown promise in manufacture of slow aspherical optics, i.e. aspheres with small departures from sphericity (smaller than 80%). The first published method can be attributed to David Brown, where he polishes the Herchel Telescope mirror with a special full size lap [17]. He uses a structured lap which offers passive bending and as a corollary this configuration assists the tool in removing undesired distortions from the aspherical mirror of the telescope. Later Jacob Lubliner and Jerry Nelson and their coworkers [18, 19] introduced the stressed mirror polishing method for the fabrication of off-axis paraboloid mirror segments of the 10 m telescope of University of California [20]. In this technique, the aspherical mirror segments are stressed as such that they are made to take the form of a sphere. Conventional spherical polishing is then used iteratively to produce the end product. Releasing the part post the process will restore the aspherical shape of the optic. Beckstette et al., [21] developed the use of a flexible rectangular large lap where the load on different zones of the tool is adjusted via actuators to accommodate the aspherical variable ROC. The tool consists of a thin layer responsible for holding the polishing pitch

i.e. “membrane polishing”, and a set of actuators applying adjustable pressures on this thin layer. Finally, the use of a “stressed lap” in the University of Arizona was adopted by a group of researchers [17, 22, 23]. This polishing configuration consists of a rigid polishing lap which continuously bent by controlled forces to conform to the aspherical shape of the optic.

Even though many researches have investigated the influence of the process parameters on the polishing outcomes, to make the end product of such a polishing configuration predictable and capable of producing high quality and accurate geometries, accomplishing such surfaces with this type of polishing requires highly skilled opticians.

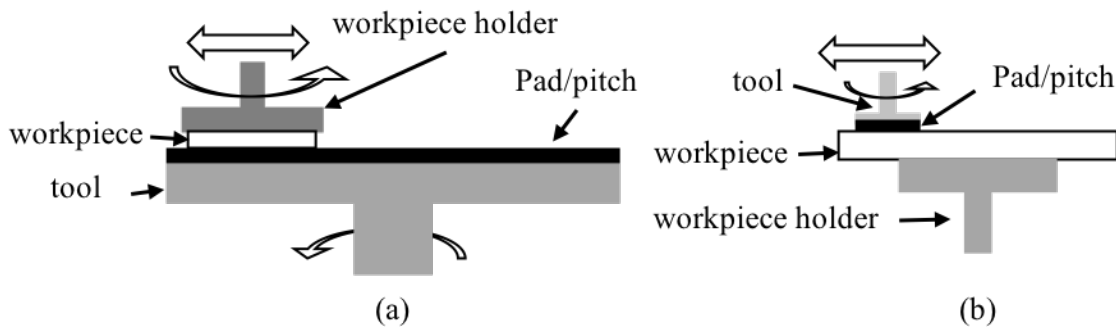


Figure 2-3 Polishing process configurations; (a) full-aperture polishing (b) sub-aperture polishing

2.3.2 Sub-aperture polishing

In this setup, the polishing tool is downsized to dimensions smaller than the workpiece (Figure 2-3(b)). The tool is only in contact with a portion of the workpiece and is translated on a given path removing material as it goes. The advantage of this configuration is that the smaller tools have the ability to manufacture variable ROC on the

surface workpiece. This is achieved by combining the tools dwell time at any point on the surface with knowledge of the tool's MR (see section 2.5 for additional details)

Three main issues arise due to the nature of the sub-aperture processes; (1) potential curvature mismatch between the tooling and the workpiece on a localized scale, (2) tooling roll-off effects near the edge of the workpiece, and most importantly (3) inducement of mid-spatial frequency errors due to the remnant tool path marks.

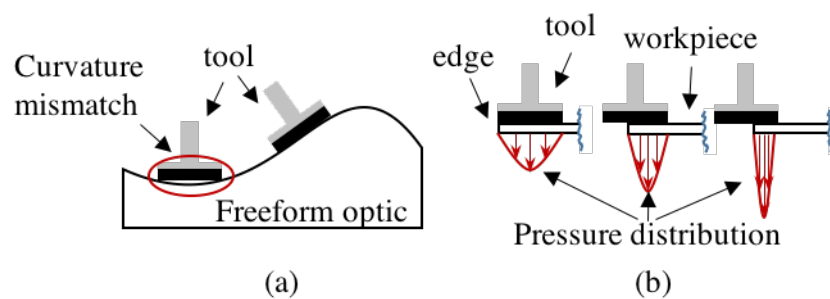


Figure 2-4 (a) Tool and freeform workpiece curvature mismatch (b) uneven pressure distribution of tool near workpiece edge

The curvature mismatch is only a difficulty when dealing with optics that exhibit very high local variations of the ROC. Figure 2-4(a) demonstrates this issue.

In conventional polishing, the so called “edge roll-off”, refers to the much larger material removal from the workpiece edge, due to uneven pressure distributions, see Figure 2-4(b). This is caused by the tool moving off the edge, thereby shrinking the contact area significantly, and as a consequence the rise of very high contact pressures [24, 25].

The third disadvantage associated with this polishing configuration, i.e. inducement of MSF errors, will be discussed later in section 2.6.3, but is related to remnant tool path marks inherent in the process. This polishing setup is the most modern version of polishing systems and will be discussed in more detail in section 2.5.

2.4 Polishing Components and the Physics of Material Removal

Polishing is an abrasive process where at its basic core, the workpiece, the tool, and loose abrasive particles are the main components of the process. The interaction of the three components leads to the removal of material from the workpiece surface. The polishing process, sometimes referred to 3-body abrasion process, and a close up of the described components is depicted in Figure 2-5(a), (b).

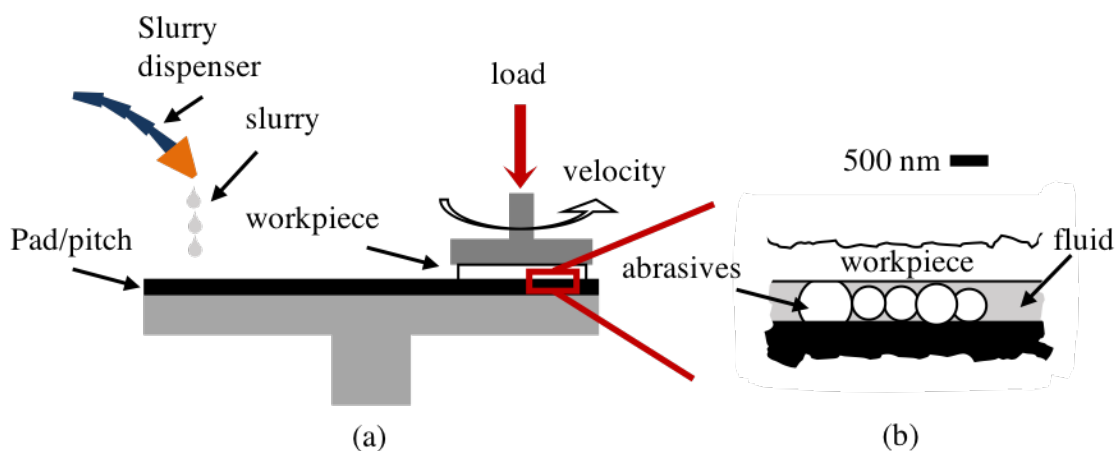


Figure 2-5 (a) Polishing process overview (b) close up of the 3-body interaction

One of the first predictive models for polishing was proposed by Preston [26] in 1927. This model simply states that the material removal rate (MRR) is a function of the applied pressure on the abrasive to the surface of the workpiece and the relative velocity of the abrasive particle with respect to the workpiece. While this model overlooks a large group of parameters affecting the material removal (MR), Preston concludes that all these factors can be grouped into one constant, K_p (i.e. Preston's Coefficient) with the assumption that the constant will not change, if no other parameter, e.g. particle type, slurry pH, temperature, etc., changes. Preston's equation is used ubiquitously in the polishing research work to date and is as follows:

$$MRR = K_p PV \quad [\mu m^3/s] \quad (2-1)$$

The MR mechanism of polishing is a very complex chemo-mechanical process. Understanding the MR mechanism of polishing has been the subject of a vast number of research articles in the past. Evans et al [27] have provided an excellent and detailed review of the different possible removal mechanisms during polishing. Figure 2-6 depicts a summary of the removal mechanisms detailed in [27].

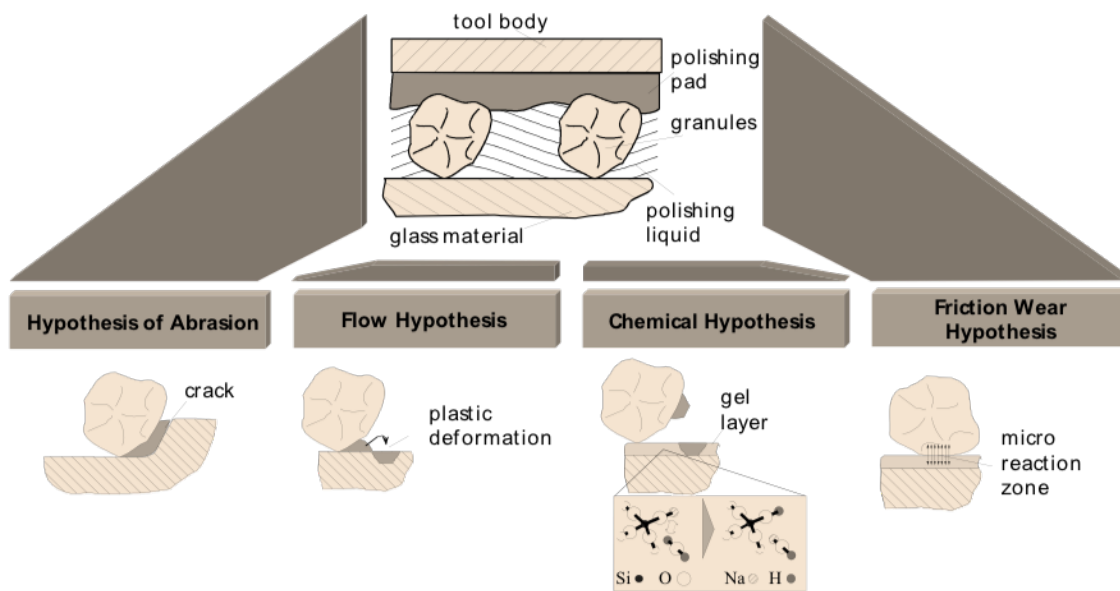


Figure 2-6 Possible material removal mechanisms during polishing [27]

The initial MR mechanism theories mainly attributed the polishing MR to abrasion action of the abrasive particles on the surface. It was speculated that the applied pressure on the abrasive particles causes the appearance of a groove on the surface which is thought to be a result of mechanical ploughing and/or cutting. Sir Isaac Newton [28] was one of the first proponents of this model. Samuels [29] provides evidence of this removal mechanism by showing SEM imaging of polished metals and the residue swarfs of material that greatly resemble grinding chips.

Later, in the early 20th century the “flow hypothesis” became very popular. Sir George Beilby [30] is probably one of the first scientists who proposed this model. According to this hypothesis, the local heat generated as a result of the friction between the abrasives and the surface, softens the surface material, leading to the plastic deformation of the affected zone. The deformed material is moved to the openings in-between the asperities of the surface, resulting in a smoother and specular surface, as expected in polishing.

The chemical aspect of the removal mechanism describes the formation of an affected layer, the “gel” layer, on the surface of the workpiece as a consequence of the chemical reaction between the slurry fluid and the workpiece surface. Harada and Izumitani [31], have shown how the different chemical combinations of polishing slurries on glass changes the micro-vickers hardness of the glass surface. The adhesion of the formed gel layer to the abrasive particles and/or the mechanical ploughing action of the abrasives on this softer layer causes the removal of material.

Finally, the concept of “chemical tooth”, was introduced to explain the removal mechanisms that weren’t otherwise explainable with the mechanisms described in the preceding paragraphs. In this description of the MR mechanism, the chemical bonding between the abrasive particle and the surface of the workpiece in the microscopic level is the main cause for the removal of material off the surface of the workpiece. The chemical reaction of the abrasives is speculated to be enforced near zones with defects on the surface of the glass. This mechanism, best explained by Cook and Brown [32, 33], captures the chemo-mechanical nature of polishing comprehensively. In this description provided by Cook [32] the chemo mechanical nature of MR has five key stages; (1) the water diffusion

under the glass surface, (2) the glass surface dissolving in water under the polishing pressures (3) the chemical bonding of the dissolved glass material to the abrasive particle, (4) the dissolved material can back-deposit on the surface under special condition which this affect the MRR, and (5) the dissolution of the surface as a result of interaction between the particles.

Ed Paul [34] has proposed a generic predicting model that encapsulates the chemo mechanical nature of the polishing based on Cook and Browns description. The application of this model to polishing tungsten [35] has shown a good agreement between the experimental and that predicted by the model. The polishing was done under a variety of chemical and mechanical parameters. More recently, Suratwala and his group [36-38] in Lawrence Livermore national lab (LLNL), have extensively provided invaluable insights in the application of Cook and Brown model in polishing glass. Their investigation has revealed the impact of slurry chemistry, abrasive size, pad stiffness, pad texture, on the glass polishing rates.

In summary of this section, Cook and Brown material removal mechanism is the most widely accepted description of the polishing process and many other researchers have provided evidence that supports their theory. While the MR mechanism theories presented in this section were brief, the goal was to indicate the complexity of the apparently simple polishing process. The focus of this work was not to advance any additional MR mechanism theories, but rather applying general conventions to the process developed in this dissertation.

2.5 Deterministic Finishing

Deterministic finishing, refers to a process whereby the final geometric form of the optic can be predicted within low associated uncertainties. The sub-aperture polishing tooling as well as great advances in computer technology and fast, digitized quantitative measurement of optics, has made deterministic finishing possible. Over approximately the past fifty years a variety of technologies were developed that could be used as a MR tooling, in a deterministic fashion. Most of the technologies rely on the abrasive processes in removing material. the most notable are listed in Table 2.1

All deterministic finishing processes require a stable removal footprint. The tool removal footprint per unit time while stationary, is known as the tool influence function (TIF). The TIF changes with variety of process parameters, e.g. workpiece material, polishing slurry, tool type, process kinematics, etc. [39]. Better measurement and characterization of the TIF yields better predictability of the process outcome and thus a higher process determinism [40]. In each process a tool path is generated, i.e. the tool is rastered over the entire surface. The tool can dwell at each point of the tool path as much as needed, longer dwell times result in higher MR at that point. A matrix containing the dwell time of the tool per point, i.e. the dwell time matrix, is calculated by mathematical deconvolution between the total amount of MR desired from the part and the TIF. The desired MR from the workpiece is determined by subtracting the ideal surface map from the measured (actual) surface map. The described process chain is iterated until the optic meets its specifications, see Figure 2-7.

Table 2-1 Deterministic finishing processes

Mechanism	Year	Process name	Tool Type	Limitation
Abrasion	1972	Computer assisted optical surfacing (CAOS) [41]	Pad tool	Rigid tool
Abrasion	1977	Computer controlled optical surface (CCOS) [42, 43]	Pad tool	Rigid tool
Abrasion	1980	Float polishing [44]	Float polishing	Low MRR
Abrasion	1991	Canon super smooth polisher (CSSP) [45]	Pitch tool	Rigid tool
Abrasion	1995	Magnetorheological finishing (MRF) [46-48]	MR fluid	Complex tooling
Abrasion	1998	Fluid jet polishing (FJP) [49, 50]	Abrasive jet	Sensitive TIF
Abrasion	2002	Precisions [51, 52]	Bonnet tool	Rigid tool
Abrasion	2006	Magnetorheological Jet [®] (MR jet) [53, 54]	MR fluid jet	Sensitive TIF
Ablation	1989	Ion beam figuring (IBF) [55]	Ion beam	Low MRR
Atomic level removal	1987	Elastic emissions machining (EEM) [56, 57]	Rotating sphere	Low MRR
Chemical Etching	1992	Chemical vaporization machining (CVM) [58]	Plasma beam	Low MRR

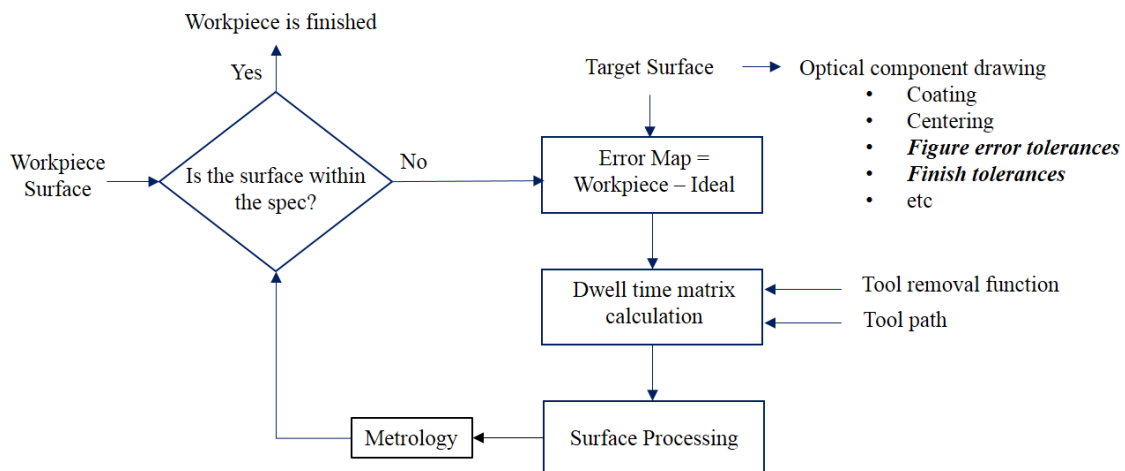


Figure 2-7 Deterministic finishing process map

The technologies in Table 2.1 mostly focused on alternative finishing tooling that could be incorporated in a sub-aperture system and would offer specific advantages. Walker et al. [59-61] developed the use of the “bonnet” polishing tool in the “Precision’s” process, see Figure 2-8(a). The machining center used for this tool, the Zeeko machine, provides 7 axes of motion, enabling the orientation of the tool in different angles. The Zeeko polishing system’s high yield and the ability to produce low surface roughness values, has made this system one of the most widely used machines in the optics industry.

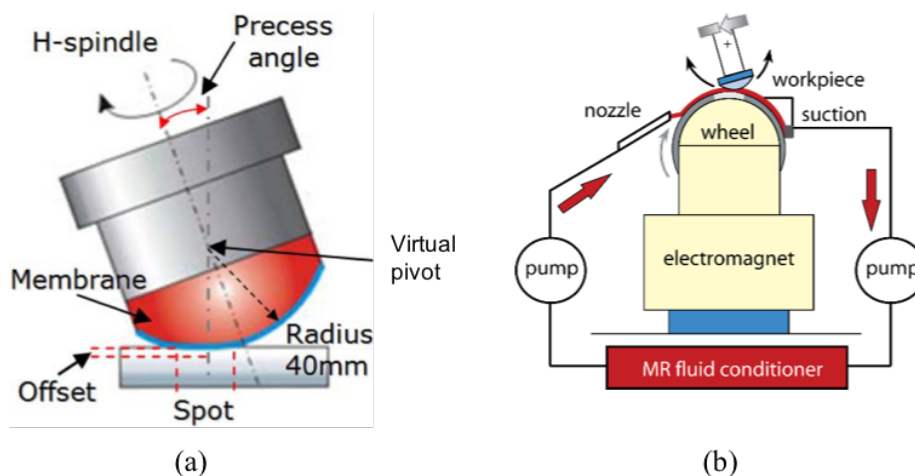


Figure 2-8 (a) Bonnet polishing tool [62] (c) MRF system [63]

One of the other most commonly used and efficient deterministic systems today was developed in the 90's, the QED magnetorheological finishing (MRF) system [64]. Kordonsky et al. [46] demonstrated that a stiffened ribbon of abrasive rheological fluid under the influence of a magnetic field and brought into contact with an optic surface, causes the removal of material from the part. This idea was transferred into a sub-aperture polishing apparatus where the fluid ribbon is carried on top of a rotating wheel [47, 65]. The TIF of the process, is basically the material removal profile of the MRF where the fluid contacts the optic and removes material, see Figure 2-8(b). Achieving figure error tolerances less than 30 nm and surface finishes of the order of 1 nm RMS, with the MRF system is very feasible. The material removal mechanism of the MRF process is mostly attributed to the fluid shearing the surface through the abrasive particles [66, 67].

In each of the sub-aperture processes, the integral components are, integration of the measurement data into the process, a stable tool TIF, as well as controlled motion of the tool, including the translation feed and spindle speeds. These processes, enable the optical fabricators to easily produce freeform and aspherical optics. That being said, a remaining unsolved challenge with respect to optics fabricated by deterministic finishing is the MSF errors imparted by the processes, see section 2.6.3 for details on MSF errors.

2.6 Surface Characterization of Optical Components

Researchers active in metrology and characterization of engineering surfaces, typically seek to measure and evaluate surface geometrical properties, as well as, their mechanical properties. This dissertation, however, doesn't consider the processed surfaces in terms of their mechanical behavior. The concepts laid forth for quantification of surfaces will be described from the optician's perspective, i.e. with respect to dimensional

metrology. One common approach for characterization of the dimensional errors of surfaces, is the separation of the surface components into three different regimes. In general these three regimes are termed as “form”, “waviness” and “roughness” [68, 69]. Though defining sharp distinguishing lines between the aforementioned errors is usually challenging, as the distinguishing lines are dependent on the application of the surface. In case of an optical component the wavelength of the incident light will be a determining factor. Figure 2-9 illustrates these three components for a given “planar” workpiece.

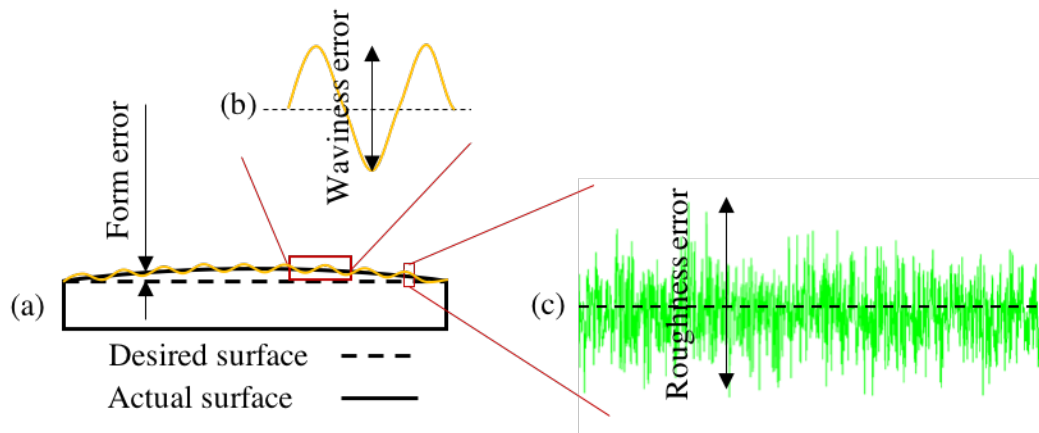


Figure 2-9 (a) Form, (b) waviness and (c) roughness errors for a “planar” workpiece

2.6.1 Form or figure

Form or figure refers to geometrical features of the surface that can be described with periodic functions with periods typically larger than 3 mm.

Figure error is usually caused by the large mechanical deformations induced on the workpiece during the mechanical processing of the part. The mechanical deformations can be caused by the residual stresses present in the part, either from previous processing, and/or the fixturing of the workpiece during the process. The other sources of figure error can be the thermal variations during the process.

Figure error causes the input wavefront of a lens to distort in an undesirable way, see Figure 2-10(a). A close up of the surface geometry and its ideal shape is depicted in Figure 2-10(b). The transmitted wavefront remains relatively coherent, therefore, it is expected for the optic to be able to form an image with present distortions. This type of distortion/aberration is different than that of inherent to special optical geometries, where the correction of such aberrations can be done with subsequent optical elements. Detailed discussions on how optical designers use different approaches for the correction of common inherent aberrations are available in many sources [70-72]. Striving for fabrication of lenses with low figure errors, as the underlying system structure could always facilitate the design process, as attention is only needed for fixing the inherent optical aberrations.

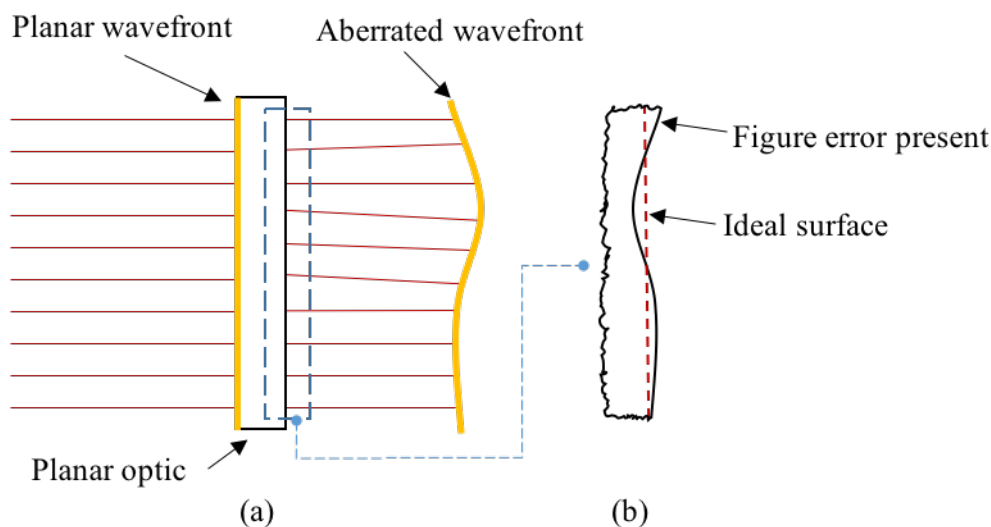


Figure 2-10 (a) The influence of figure on a planar wavefront, (b) close up of the surface geometry and the extent of figure error

In optics, it is common to describe figure errors via a set of orthogonal base polynomials. The RMS of the base polynomials and/or the peak to valley (PV) of each

individual term is used to specify the form errors for a given optic. There are a variety of these polynomials developed by mathematicians over the past century. Since circular parts in optics are prevalent, using a set of orthogonal polynomials in the polar coordinates can facilitate the characterization of a large group of optics. One of the most widely used orthogonal basis, was first derived by Frits Zernike [73]. A detailed account of the Zernike polynomials and their relevant shapes can be found in reference [74]. Zernike polynomials ought to work very well in characterization of conventional optics, and theoretically it is possible to use them for describing freeform and aspherical optics. However, as pointed out by Forbes and Kaya [75-77], the use of Zernike polynomials per se is not numerically efficient. Forbes showed that the use of a proper basis for the orthogonal polynomials can significantly improve characterizing aspherical optics in his paper published in 2007 [75].

The International Organization for Standardization (ISO) has provided documentation for specification of form in optical drawings in the ISO 10110 parts 5, 12, and 19 [78-80]. The part 12 and 19 are recommended for specifying aspherical and freeform optics respectively.

2.6.2 Roughness or finish

Surface roughness or finish, is a term used to describe surface features that are repeated with a much smaller period than that of form. The upper limit of roughness bandwidth is considered ~ 0.08 mm for visible light applications.

The roughness of a surface post of a process is highly dependent on the mechanical and chemical aggressiveness and the MRR of the process. Mechanically Aggressive and high MRR processes such as grinding produce matt finishes. Whereas, slow processes like

polishing can produce specular and shiny surfaces. Polishing under favorable chemical conditions and the absence of etching typically leads to surfaces with low roughness values.

The surface roughness of optical components causes the incident light to scatter in random directions. That is mainly due to the comparable lateral dimension of surface finish to the wavelength of light. The random direction of the scattered light implies that for roughness values above a certain limit no image can be formed by the optical component, which is contrary to the impact of figure error. For a specular surface (which are desired for most optical applications), the amount of scattered incident light is directly correlated to the square of the RMS of the surface roughness [81-84]. The well-known Rayleigh-Rice theory introduces the expression for the correlation between the distribution of scattered light and surface roughness. The total integrated scatter (*TIS*), which provides a measure of the number of scattered photons in the optical component, is directly correlated to the RMS of the surface roughness with the following relation given by Harvey et al [85]:

$$TIS \approx (4\pi\sigma/\lambda)^2 \quad (2-2)$$

Where σ is the RMS of the surface roughness and λ is the wavelength of the incident light.

Based on the argument above, for quantification of surface roughness on optical surfaces, the RMS of the high frequency surface deviations is used. To quantify the high frequency surface variations, a high magnification interference microscope can be used. For separation of the local forms of the measured data, high pass filtering is applied. These filters are, nowadays, available in digital format and is applicable to the digitized measured data. The application of digital filtering to the measured data is detailed in many highly regarded works [68, 86]. As suggested by the aforementioned references the use of the

discrete Fourier transform (DFT), and suppression of the unwanted spatial frequencies present within the data can be conveniently implemented, to separate the roughness data.

The part 8 of the ISO 10110 standard is dedicated to the specification of surface texture on optical components, which is inclusive of the surface roughness as well [87]. The standard recommends the use of the RMS of the roughness for optics specification. The definition for the RMS of the roughness data is provided in ISO 25178-2 [88]. ISO has also, disseminated documentation which elaborates on the different type of filters and their operation on the surface data [89-92]. The afore mentioned standards recommend a cutoff of 0.08 mm for the calculation of surface roughness.

2.6.3 Waviness or mid-spatial frequencies (MSF)

Waviness, or MSF refer to the surface features that have a spatial period of approximately 0.08 mm up to 3 mm. As can be inferred by the number, the MSF wavelength is in-between the scale of features associated with form and roughness errors.

The main source of the inducement of MSF errors is the tool marks post a sub-aperture process. Since the tool path in the sub aperture processes are a raster path or a spiral path, the periodic MSF features are induced with a period correlated to the path stepover. Hull et al [93] have provided a list of the possible sources of MSF errors. Some of the most notable ones due to the fabrication process are: (1) the imprint of the structure ribs of backing of the optic if a light weighted structure is used (2) poor tool and workpiece curvature mismatch and uneven pressure distribution of the tool over the aperture of the workpiece, (3) imprint of the tooling back support structure on the surface. The growing interest in use of freeform and aspherical precision optics, and the more use of sub-aperture processes as a corollary, has signified dealing with MSF features. Parks [94] has shown

how not considering the MSF errors can result in failure of the performance of the optic containing them.

The existence of MSF features on an optic causes the appearance of flare in the image produced by such optics. This phenomena is attributed to the “small-angle scatter” [95, 96] effect of the MSF features. Small-angle scatter effects, spread the area of the point spread function (PSF). Based on the geometrical optics theory, a converging lens is expected to image a perfect point source to a “perfect” point. See Figure 2-11(a). Yet due to the limited aperture size in any lens (or optical system) the effects of diffraction prevent the system of achieving such a perfect point, see Figure 2-11(b). The intensity distribution of the imaged point source is the PSF of the optical system.

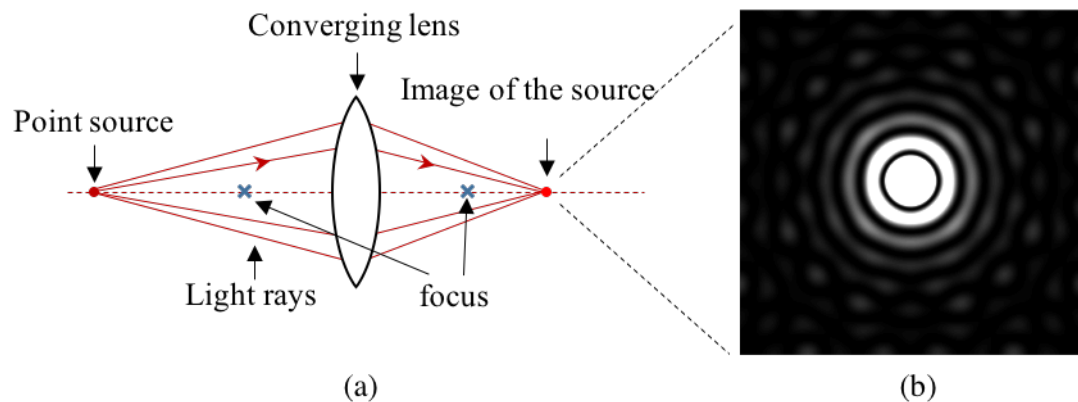


Figure 2-11 (a) “perfect” imaging of a point source (b) “real” diffracted spot image

The effect of the different surface errors, figure, finish and MSF, on the PSF was investigated by Harvey et al [96]. Figure 2-12 shows linear profiles across the PSF of surfaces with figure, finish, and MSF errors. It is clear that the MSF errors, contrary to figure and finish broadens the PSF. Figure and finish on the other hand reduce the peak magnitude of the PSF.

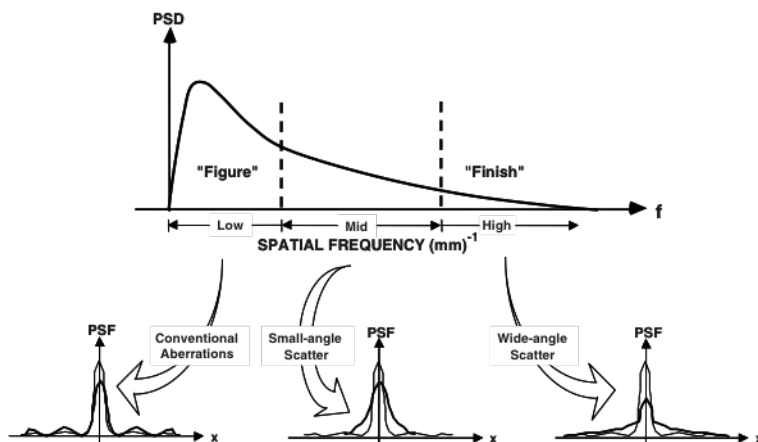


Figure 2-12 The effect of figure, finish, and MSF errors on PSF [96]

Figure 2-13(a), (b) show the spot imaging of two optics without and with MSF features respectively. As evident in the figure, the optic with MSF features (period of 2 mm and RMS of 35 nm), has a broader image of the point source. As a consequence of this broadening of the PSF, flare and reduction in the resolution of the optical system will occur.

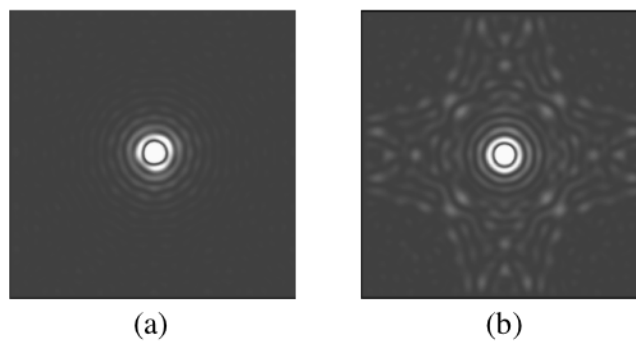


Figure 2-13 (a) PSF of an optic with no MSF features (b) PSF of an optic with MSF features with a period of 2 mm and RMS of 35 nm

For quantification of the MSF errors, the power spectrum density (PSD) of the surface deviations of the optic is one of the most widely used techniques in the optics community. Generally speaking, the PSD of the surface is obtained by applying the Fourier

transform to the surface height data. The MSF features, as pointed out earlier, are periodic surface features in nature. Therefore, the power spectrum should demonstrate a strong signal at the frequency of the MSF's. The power of this signal can be translated to the magnitude of the MSF errors. This can be conveniently explained by the use of Parseval's [97] theorem expressed below:

$$\int_{-\infty}^{+\infty} |z(x)|^2 dx = \int_{-\infty}^{+\infty} |Z(f_x)|^2 df_x \quad [\mu m^3] \quad (2-3)$$

Where $z(x)$ is the height distribution on a linear 2D profile, and $Z(f_x)$ is the Fourier transform of $z(x)$. The Parseval's theorem implies that the reduction in periodic surface errors, will translate into the reduction of the power of the aforementioned error in frequency space.

The use of the PSD function for evaluation of surface roughness was first investigated by Rasigni et al [98]. In their paper they show that the spectral analysis can be used to compute the roughness and waviness of the surface with the PSD. Church et al [99] had used the PSD in comparing the measurement data of a single part using two different instruments. Nevertheless, it was Church and Tackas [100] that firstly demonstrated the use of the PSD of the surface measurement data can be very beneficial in prediction of the light scattering characteristics of the surface. Later the researchers in LLNL [101-105] published documents on how the PSD could enable imposing tolerances on the optics manufactured for the national ignition facility (NIF) optics. Some efforts for the use of the aerial PSD has been taken more recently [106, 107]. However, little usefulness of this method has been showcased thus far.

One of the other metrics common in determining the image quality of an optic influenced by the MSF features is the use of modulation transfer function (MTF). The MTF can be quantified by evaluating the square of the absolute value of the Fourier transform

of the PSF. Intuitively speaking, the MTF is the power spectrum of the PSF and it reveals the resolving power of the optic for a given feature size. The MSF errors cause the MTF values to be smaller at higher spatial frequency features. For more details of the effect of MSF errors on the MTF look into references [96, 108, 109].

The ISO 10110 standard [110] has instructions on specifying the PSD tolerances on optical drawings as a method in controlling MSF specifications on optical components.

2.7 Available Solutions for MSF Reduction

MSF errors are bearing significant amount of limitations on the optical components containing them. The removal of the MSF errors, post the processes causing them, is also very costly and challenging. Unfortunately, there are not many options available for the reduction of MSF errors on freeform and aspherical optics. For planar and spherical optics, a full-aperture tool with a hard polishing pad is usually used, see Figure 2-14. Parks and Evans [111] have conducted experiments using a conventional polishing tool, with backed foam of pellaon to show preferential material removal from the high regions of the diamond turning marks from diamond-turned electroless nickel and aluminum.

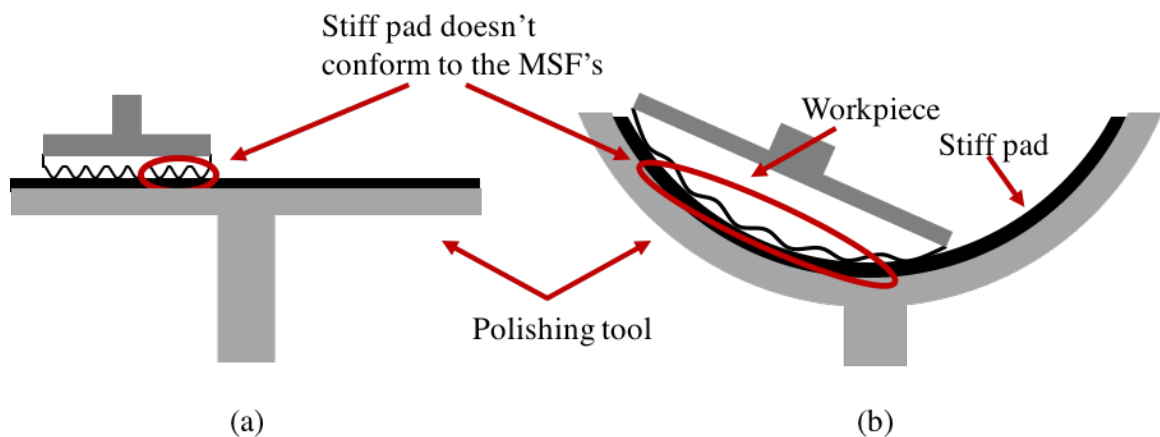


Figure 2-14 Polishing MSF errors; (a) from planar (b) from spherical workpiece

The rigid full-aperture tooling cannot be used for polishing MSF's off freeform and aspherical optics generally. The full-aperture tooling is mostly available for polishing MSF's off parts with constant ROC, i.e. planar and spherical optics. Limited full-aperture MSF reduction technologies for aspheres are available. The VIBE polishing process developed by Optimax [112, 113] is a full-aperture polishing tool for removal of MSF's from aspheres, see Figure 2-15. In this method, a rigid polishing lap with a flexible pad is used. The lap has dimensions as close as the aspherical workpiece. High frequency vibrations are applied to the lap during the polishing which assist in removing the MSF errors. The lack of any rotational symmetry of freeforms rules out any possible full aperture solutions for the removal of MSF's of such optics.

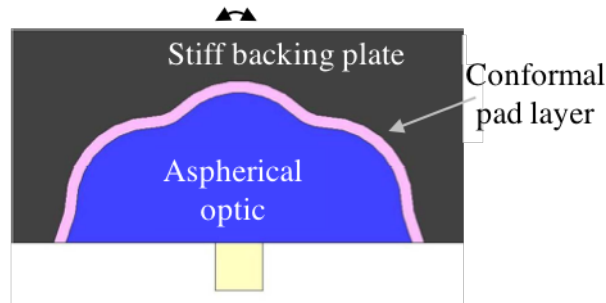


Figure 2-15 Optimax VIBE finishing process [113]

The other group of approaches for controlling the extent of the MSF errors is modification of the polishing tool path. The typical tool path for polishing freeforms are shown in Figure 2-16. Some control over the wavelength of the induced MSF errors can be applied by modifying the tool stepover in each case [114].

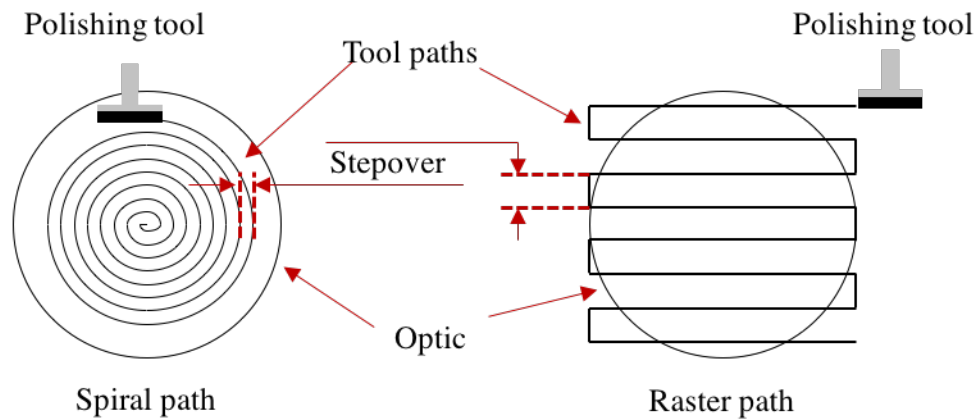


Figure 2-16 Conventional polishing tool paths

The use of “pseudo random” polishing tool paths by Dunn et al [115] has shown to decrease the amount of MSF errors. Figure 2-17(a) shows this pseudo random tool path. Wang et al. [116] have adopted a similar approach by creating polishing tool paths in “unicursal random maze” configuration, Figure 2-17(b). Toolpaths with non-conventional shapes, and not random in nature, are also investigated by a few researchers. The use of Hilbert tool paths, see Figure 2-17(c), in works by Dong et al [117] and Wang et al [118] has shown success in achieving MSF errors with less severity than that achievable by conventional tool paths. Essentially the idea is to intersect the polishing tool paths randomly ensuring that no periodic features with a constant wavelength is produced. The existence of uneven pressure distributions of the polishing tools, nonetheless, is unavoidable. While the tool paths can greatly aid in smoothing of the MSF errors on parts with mild slope variations, the case is far more complicated for steeper optics.

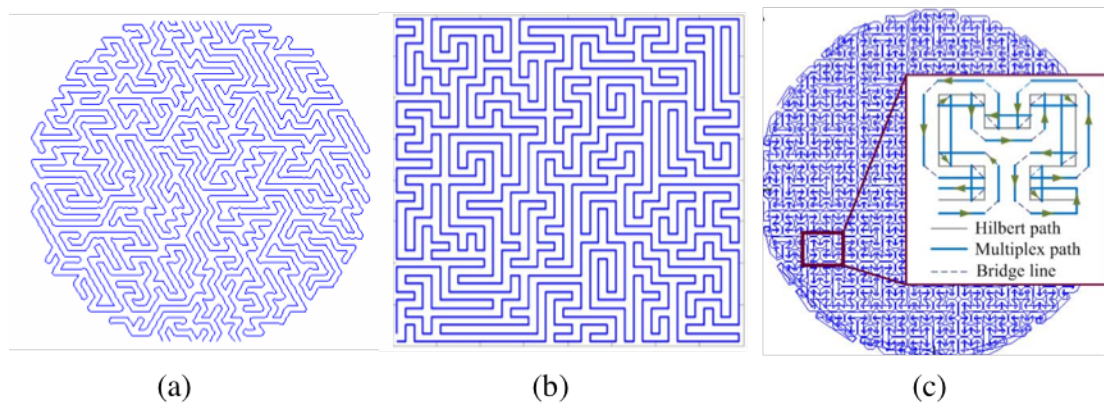


Figure 2-17 Non-conventional polishing tool paths; (a) pseudo random tool path [115] (b) Hilbert path and modified Hilbert path [118]

The final group of methods for dealing with MSF errors on optics are alternative sub-aperture tooling, that provide local stiffness to the MSF errors by some means incorporated in the tool architecture. It also should enable the tool to accommodate for the various ROC that are traversed over during the polishing action. Achieving the combination of the two is of great challenge. Dong et al [119] have developed a polishing tooling that resembles a discretized polishing pad tool, called “fixed abrasive diamond pellet (FADP)” tool, see Figure 2-18 (a,b).

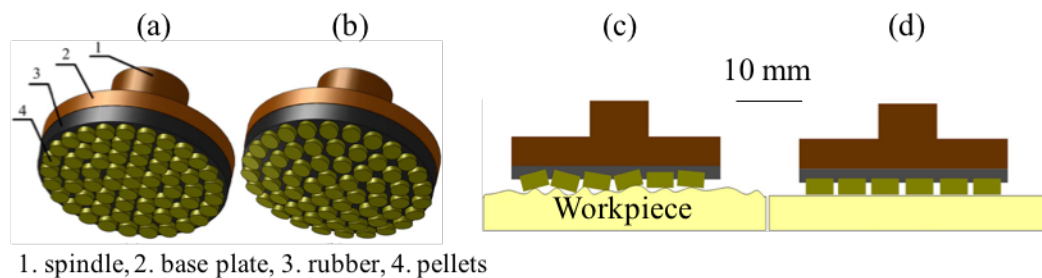


Figure 2-18 The FADP tool [119]; (a, b) planar and spherical tool configuration (c, d) pre and post the removal of MSF errors

The segmented pellets in the FADP tool gives the relative compliance to the tool, yet the stiff nature of each pellet (~ 3 mm in diameter), enhances the tool rigidity on a local scale, and thus enabling the removal of MSF errors. The shortcoming with this method is clearly that optics containing small ROC's cannot be polished and processed.

Another method that researcher in LLNL [120] have shown to have potential in removing MSF errors off aspherical samples, is the use of float polishing. The float polishing apparatus was first introduced by Namba [121]. This polishing system is based on the principles of hydrodynamics. A thin layer of slurry fluid between the workpiece and the rotating precision machined lap, causes the particles to remove material off the surface of the optic, see Figure 2-19. This approach is very effective for low departure aspherical optics. The hydrodynamics with steeper samples and/or freeform shapes will become exponentially complex in such apparatus. Needless to say, the higher capital cost associated with this system is another limitation that should be mentioned.

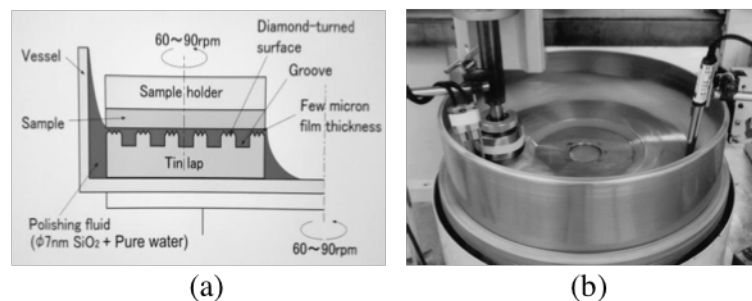


Figure 2-19 Float polishing [122] (a) schematic, (b) machine in action

In summary of this section, it is undeniable that a major vacancy of a technology for dealing with MSF errors on freeform and aspherical optics exist. The methods described here have a very limited scope and, in some cases, are specific to one specific geometry. This gave the motivation to adopt a more generic tool that would enable processing optics

with wider range of geometries. It is believed that the use of fibers can address the issue and successful implementation of a tool made of fibers can greatly enhance the capabilities of the optics manufacturing community in fabrication of freeform optics.

2.8 Summary

In summary, polishing plays a pivotal role in modern day optics manufacturing industry. Yet, the mainstream polishing systems for finishing freeform and aspheres suffer from inducing MSF errors. These errors have limited the applicability of the optics to longer wavelength region of the electromagnetic spectrum. Today, scientists such as Parks, Evans, Nelson, etc., mostly agree establishing local stiffness to the higher regions of the MSF errors, is key to effectively reduce these errors. Several group of technologies, have shown success and potential in reducing the MSF errors and were described in this chapter. However, these methods mainly encompass a limited range of part shapes. With the great advances in computer science, optical systems design has moved at a very high pace. Successfully achieving MSF reduction of freeforms will aid in transitioning the freeform design into the visible light regimen, where it can have enormous impact. This requires the manufacturing industry provide methods of reducing preexisting MSF features. The work detailed in the following chapters seeks to address this issue.

CHAPTER 3: FIBER TOOL DESIGN, FABRICATION, AND TESTING

3.1 Introduction

This chapter details three key topics with respect to fiber based tools design, fabrication, and characterization; (1) the key fiber metrics and fiber selection criteria are introduced (2) fiber metrics are measured and quantified using an experimental test bed, (3) initial tool designs and tool fabrication step are detailed, and (4) a finite element model (FEM) of the fiber workpiece fundamental interaction is created.

3.2 Fiber Selection Criteria

As discussed in Chapter 2, Preston's equation is the most widely used quantitative model for predicting material removal rates (MRR) in polishing. Pressure and velocity are both mechanical aspects of the polishing process. The K_p coefficient represents all the other elements (either mechanical or chemical) affecting the material removal (MR). In the present study, the majority of the work is focused on the mechanical contributions of the different elements involved in the fiber based polishing process.

To the best knowledge of the author, the use of fiber based tools in polishing precision optics had not been published in literature prior to this work and publications thereof. This imposed a great challenge in opting a direction for studying these tools. Hence, the baseline of the work was founded upon Preston's equation. Based on this premise, the main fiber selection criteria were the following; (1) The fiber should be

capable of applying a pressure that is expected to result in MR, (2) the fiber should established a reasonably long contact length on the workpiece to ensure that the fiber is capable of spanning multiple MSF's, (3) the fiber should be able to retain its contact with the workpiece when in motion and polishing the workpiece, (4) The fiber should be sufficiently large and robust for ease of fiber handling and tool fabrication and, (5) the final tool design should be such to enable a systematic study on the tool workpiece interaction. Thus, for keeping the action of a single fiber relatively independent from other fibers any fiber cross over in the tool was prevented.

3.3 Fiber Selection Test Bed

A simple experimental test bed for evaluation of an individual fiber interacting with a planar surface was utilized. This test bed is shown schematically in Figure 3-1.

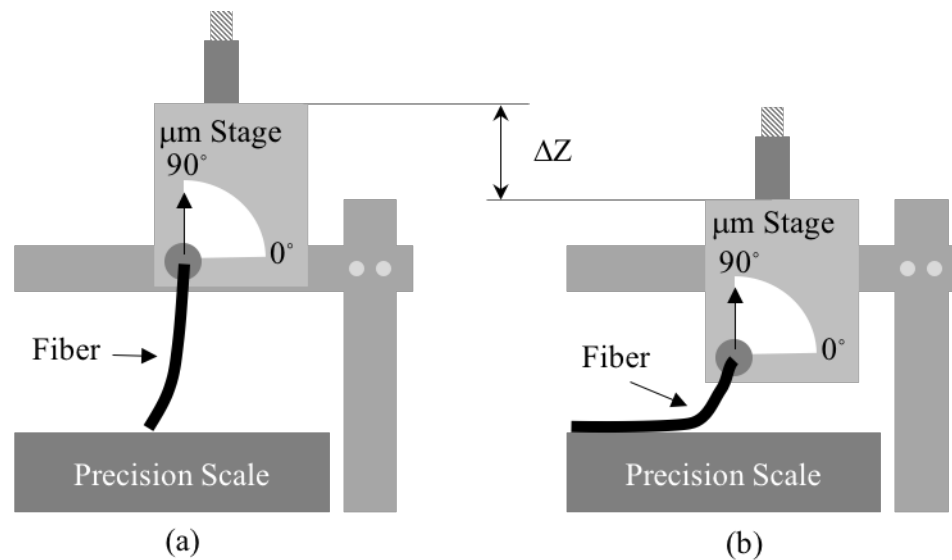


Figure 3-1 Fiber selection test bed (a) fiber disengaged, (b) fiber engaged

The test bed consisted of a micrometer stage with a displacement range of 25.4 mm and a resolution of 25.4 μm in the z direction. The fiber attached to the stage is illustrated

in Figure 3-1(a). The stage was lowered to bring the fiber into contact with a high precision scale, OHAUS® Adventurer PRO® (resolution of 0.1 mg). The approximated load corresponding to different fiber positions was measured via this scale, Figure 3-1(b). The height which the loads were measured in this setup would correspond to the plunging depth of the tool (ΔZ) for the polishing experiment. The length of the contact made between the fiber and the scale was measured approximately using backlighting and a ruler placed behind the fiber. Figure 3-2 depicts the image of the setup studying the Nylon 6/6 fiber.

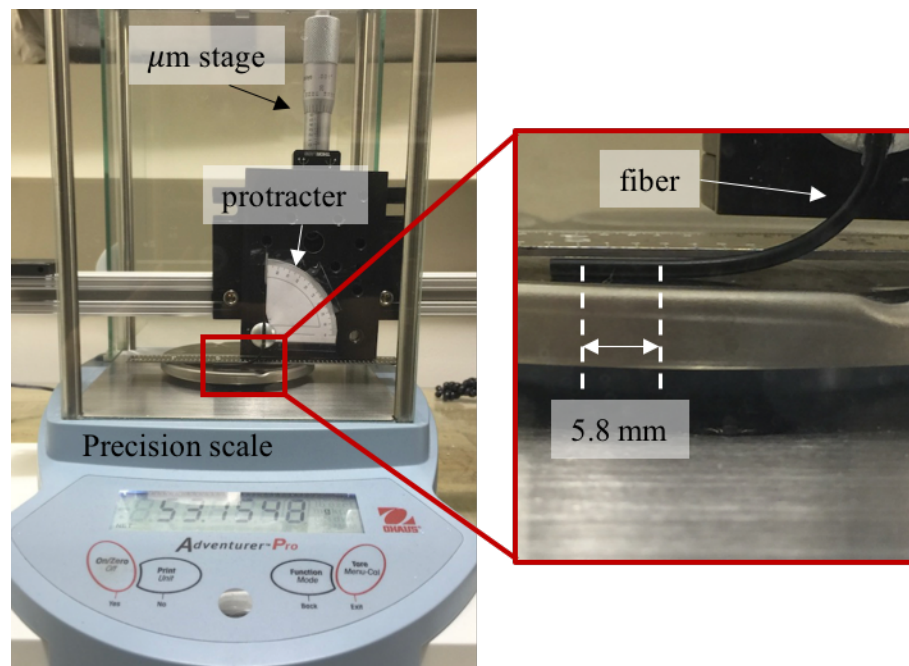












Figure 3-2 Fiber selection test bed examining the Nylon 6/6 fiber

A range of fibers with different cross section geometries (circular, triangular, rectangular, etc.), different fiber materials (Polypropylene, Acetal Co-Polymer, Nylon 6/6, etc.), and different critical dimensions (0.2 mm to 3mm) were sourced. The fibers were sourced from different suppliers. Some of them were procured from chain hardware stores such as Lowes® and HomeDepot®.

Table 3-1 summarizes the evaluation of a range of fibers using the test bed. The fiber dimensions were measured with an optical microscope. The Young's moduli of the fibers were not provided by the vendors.

Table 3-1 Fiber evaluation summary results for fiber length of 37.5 mm

Material	Geometry and dimensions (mm)	Modulus (GPa)	Contact length (mm)	Contact load (N)	Estimated pressure (kPa)
Polypropylene (Tfiber) [123]	 1.2 side	1.5	11.4	0.39	31
Nylon 6/6 (N66) [124]	 Ø1.6	2.5	5.8	0.53	600
Polyurethane (PS) [123]	 2 × 0.6	0.5	15	0.3	5
Carbon fiber (CF) [125]	 1 × 0.1	140	30	0.35	12
Co-Polymer [123]	 Ø1.4	1	4.5	0.75	1016
Silicone (SF) [126]	 Ø1.3	0.001	25	0.03	1.4
Co-Polymer [123]	 Ø0.5	1	6.75	0.01	29.4
Polyethylene terephthalate (PET) [123]	 Ø0.22	3	7.25	0.005	10
Carbon fiber (CF) [125]	 3.0 × 3.0	140	Fiber failed	Fiber failed	Fiber failed
Unknown Ceramic [127]	 0.5 × 0.25	N/A	Fiber failed	Fiber failed	Fiber failed

The modulus of each fiber in the table was approximated from values available in the literature. The pressures were calculated through dividing the total contact load by the measured contact length and approximate contact widths. The contact widths for the triangular and rectangular geometries were taken as the width of the fiber itself. These values for the circular geometries were approximated via the FEM, detailed later in this

chapter, are in the order of 10 μm (PET fiber), 50 μm (Copolymer $\varnothing 0.5$ mm), and 150 μm (fiber diameter > 1 mm). In each case the fiber was evaluated under conditions for which would provide the longest contact length achievable.

The first eight fibers in Table 3-1 successfully satisfied the conditions for qualifying to be used in a polishing tool. All of the eight fibers had a sufficiently long contact length as well as reasonable contact pressures. Polishing tests with these fibers was conducted, and the results of such testing can be found in Chapter 4. The bending stresses for the last two fibers in the table, exceeded that of their failure stress, thus causing the fibers to fail under the testing. These two fibers were disqualified for use in a polishing tool.

While conventional polishing pressures are of the order of 20 KPa to 100 KPa [128, 129], some of the pressure values given in Table 3-1 are much higher. To decrease the fiber contact pressure, two conditions should be met; (1) decreasing the applied load, and (2) increasing the fiber contact length. Tilting the fiber relative to the tool axis accomplished both of the two aforementioned points. To enable the experimental test bed for evaluating fibers at a tilted position, a protractor for measuring the angles was accommodated on the testing setup, see Figure 3-1 and Figure 3-2. As a result of tilting the fibers to an angle where the pointer in Figure 3-1 was at 40° , 50% reduction to the estimated pressures listed in Table 3-1 was achieved.

3.4 Fiber Based Tool Design and Fabrication

One of the main challenges of the work in its infancy was the vacancy of any prior work about the application of fiber based tools in precision polishing. This made the design space of such tools very enormous. Any arrangement of fibers basically, can be a different design. Regardless, the design opted for the majority of the work here was based on the

premises detailed in section 3.2, i.e. ease of fabrication and the ability of a systematic study of the fiber workpiece interaction.

Figure 3-3 illustrates two initial designs used in the work. The first design, referred to as FT-1, Figure 3-3(a), was the tool configuration most used for the work in this dissertation. Basically, this configuration is very similar to a simple paint brush in which the fibers are parallel to the shaft of the tool. In the second design, referred to as FT-2, see Figure 3-3(b), the fibers are tilted at 40° with respect to the tool axis. This design is similar to the scenario where the fiber is tilted in the fiber study setup. The goal of this design, as mentioned thereof, was to decrease the total polishing pressure exerted by the tool.

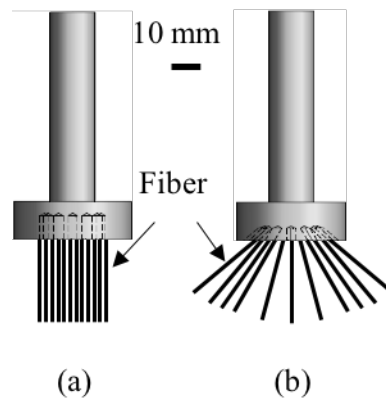


Figure 3-3 Fiber based tool initial designs; (a) FT-1 design (b) FT-2 design

The tool head was fabricated by turning a piece of aluminum initially. For a typical tool, twelve holes, as fiber holders, were then drilled into the tool head. The diameter of the drilled holes depends on the fiber used in the tool. The fibers are glued with Loctite[®] Super Glue in the holes. This facilitates later detachment of the fibers from the tool by submerging the tool into an acetone solution.

Figure 3-4(a) shows a fabricated tool using twelve Nylon 6/6 fibers with fiber length of 37.5 mm. The tool was lowered down towards the workpiece to establish contact between the tool and workpiece. Typical ΔZ values were based on results from the initial testing of the fibers on the fiber selection study setup. Upon contact with the workpiece, the fibers fanned out radially and created an annulus region in physical contact with the surface, see Figure 3-4(b). This tool was used for the majority of the polishing experiments throughout this dissertation.

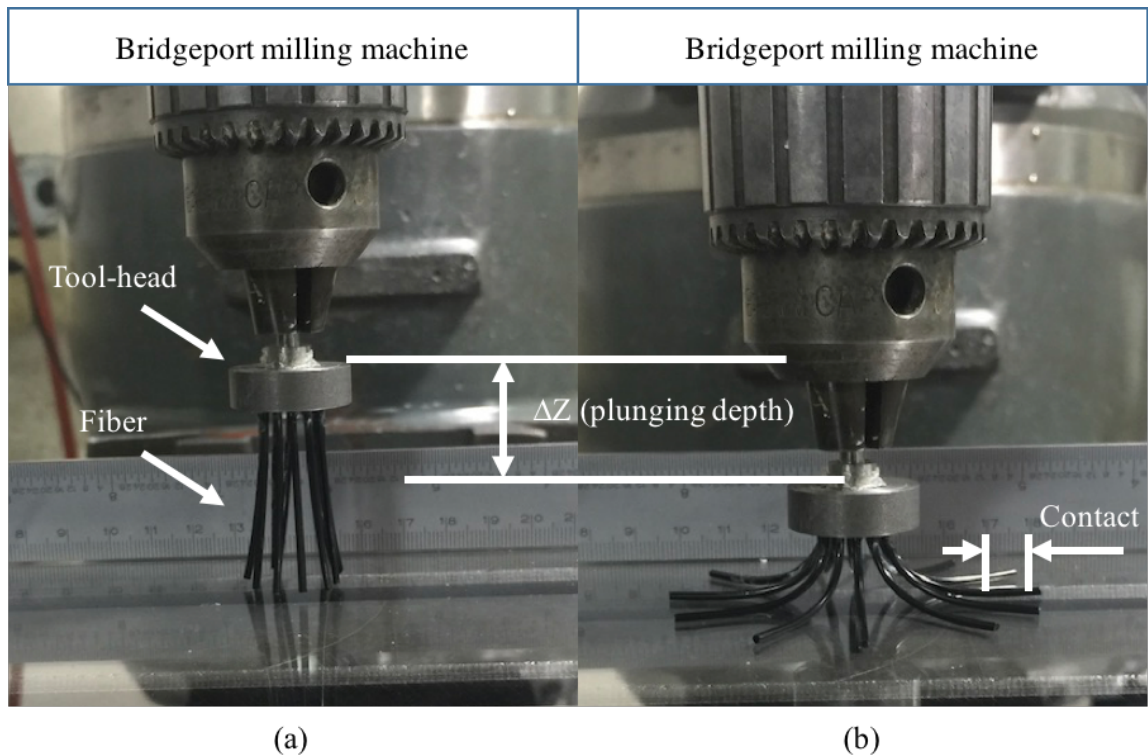


Figure 3-4 Fiber based tool FT-1 design attached to the Bridgeport milling machine; (a) disengaged, and (b) engaged with workpiece

3.5 Fiber – Workpiece FE Modeling

One of the main shortcomings of the fiber study test bed, was that, it doesn't provide any insights on how the applied contact pressure by the fiber is distributed over the fiber-

workpiece contact length. For comprehending the fundamental fiber-workpiece interaction, a FE model (FEM) was created. The model is a static model (no tool rotation), created in ABAQUS®/Standard [130].

3.5.1 Nylon 6/6 fiber

While the FEM's for different fiber material/geometry combinations were developed over the course of this work, details associated with modeling of a particular fiber is presented here. This fiber, the Nylon 6/6 fiber (sourced from Hahl-Pedex®: Hahl PA 6/6) (Table 3-1), was mainly chosen due to its extensive use in this work.

The Nylon 6/6 fiber with a length of 37.5 mm and \varnothing 1.6 mm was used. Elastoplastic behavior was attributed to the material of the fiber. The nonlinear behavior was accommodated through tabulated data obtained through the stress – strain curve shown in Figure 3-5. No additional creep behavior was included in the model.

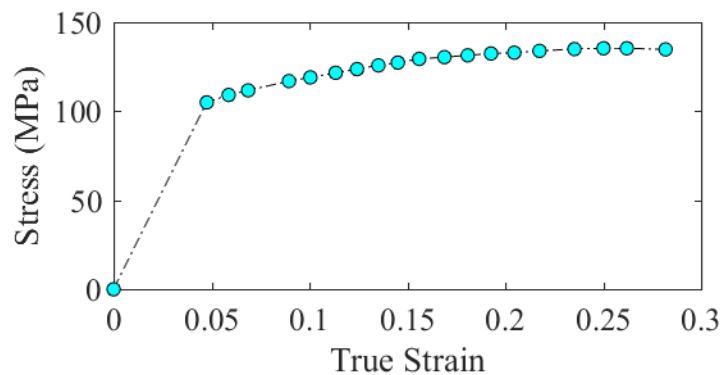


Figure 3-5 Nylon 6/6 fiber stress/strain curve [124]

3.5.2 Glass workpiece

The workpiece, made of glass, was only modeled using elastic elements. The modulus of elasticity was set as 70 GPa. The dimensions of the glass were taken as 37.5 mm \times 5 mm \times 1 mm.

3.5.3 FEM steps and boundary conditions

To simulate the fiber-workpiece interaction a multi-step model was created. In the first step the fiber was bent in the plane of engagement (Figure 3-6(b)) by enforcing an angular displacement to the tip of the fiber. This deformation was necessary in the polishing experiment as well, for ensuring proper fiber-workpiece contact. In step 2 (Figure 3-6(c)) the workpiece was displaced towards the deformed fiber, until contact was initiated.

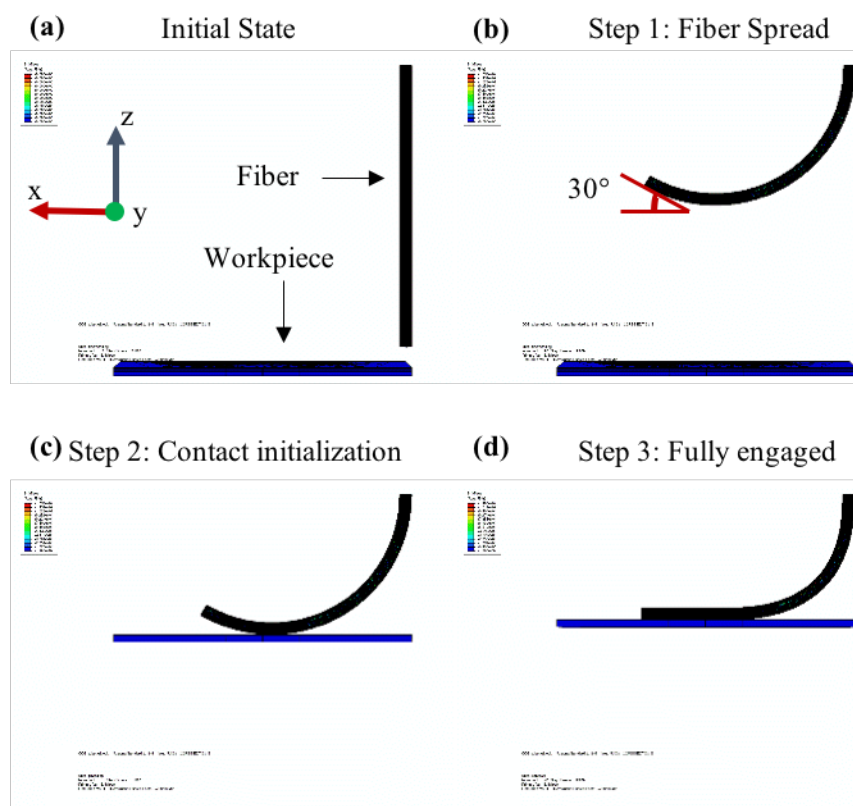


Figure 3-6 Fiber-workpiece interaction FEM steps

Finally, in step 3 (Figure 3-6(d)), the angular displacement at the tip of the fiber was removed, while the workpiece was moved towards the fiber by a small amount (2 mm), causing the fiber to attain static equilibrium state, and establishing a full contact with the workpiece. The coefficient of friction between the surface and the fiber was taken as 0.1.

The normal contact behavior between the fiber and workpiece, was picked as “hard” contact. This implies that with the pressure contact approaching zero, the fiber will no longer be in contact with the workpiece [130].

Since the geometry of the FEM is symmetric, the model was halved in the plane of the fiber bending. The fiber is fixed at the top, where in the actual tool, reflects where the fiber is fixed to the tool head. The symmetry conditions were applied on the halved fiber and workpiece faces. The end of the fiber and the workpiece will observe boundary conditions in accordance with the model steps, described earlier. In step 1 and step 2, the fiber end was bent 120° , around the y-axis. This displacement was removed in step 3. For the motion of the workpiece, the displacement boundary condition was attributed to the bottom face of the glass plate. These displacements were 0 mm, 20.5 mm, and 22.5 mm, in step 1, step 2, and step 3, in the vertical direction respectively. The final displacement value was selected to reflect the ΔZ used in the polishing tests.

3.5.4 Meshing scheme and number of elements

For discretization of the entire model, C3D10M (modified quadratic tetrahedral) elements were used. The fiber was meshed uniformly with element size of $100\ \mu\text{m}$. The glass workpiece on the other hand was equipped with biased meshing scheme. The element sizes were as small as $50\ \mu\text{m}$ in the contact zone, whereas the mesh size far away from the contact zone went up to 5 mm. The total count adds up to 327,224 elements and 493,155 nodes. Figure 3-7 shows the overall meshing, as well as, the close up of the fine elements used.

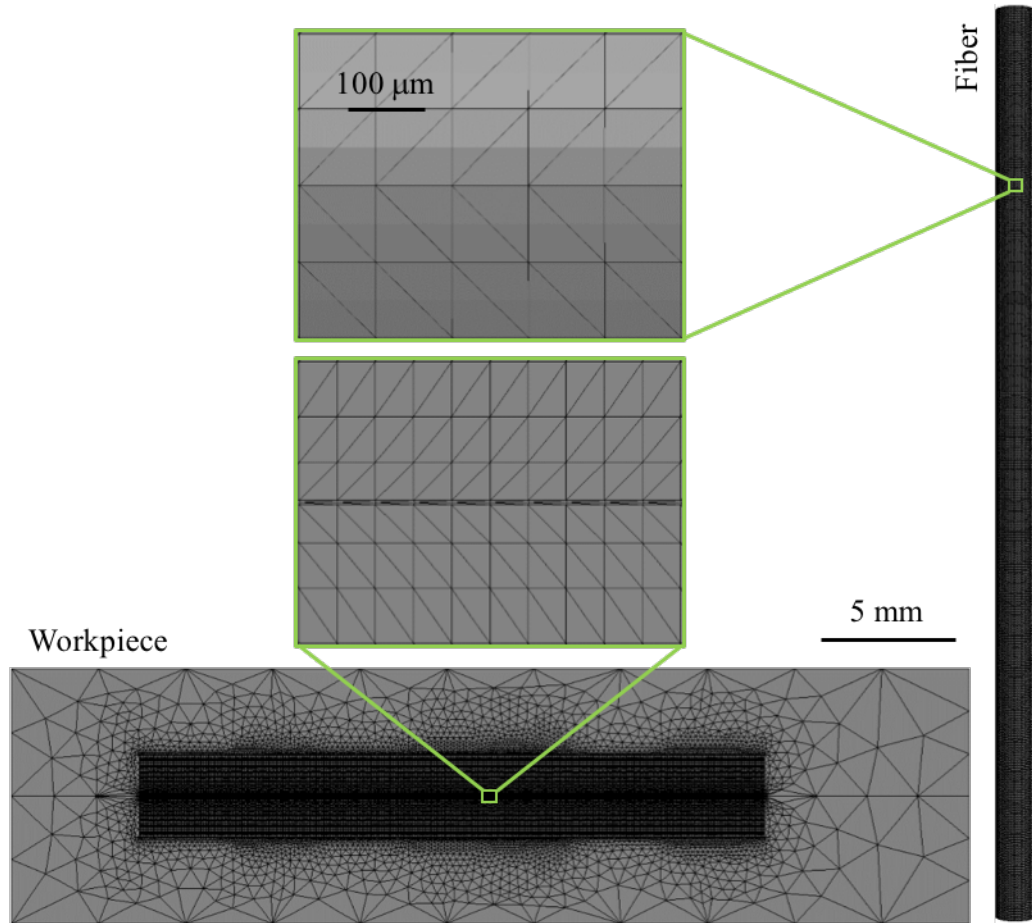


Figure 3-7 Fiber and workpiece overall meshing and close-up of the finer elements

3.5.5 Model results (planar workpiece)

As mentioned earlier, one of the main underlying parameters of the polishing process is the pressure distribution exerted by the polishing tool on the workpiece. Examination of the pressure distribution was a key goal of the FEM work. The experimental test bed explained in section 3.3 didn't provide any insights on this distribution. However, the FEM can complement the experimental test bed providing fiber contact pressure distribution. This contact pressure distribution in ABAQUS is called CPRESS. Figure 3-8 shows the pressure distribution obtained from this model. A line profile of pressure (pressure on a line) was extracted from the centerline of the contact

zone, (Figure 3-8(b)), and a V-shaped profile was observed. This line was where the highest pressure values are exerted. The ability of fiber based tools in removing material will be discussed in detail in the next chapter, where it will be shown that the MR profile exhibits the same V-shape. The striking similarity between the removal profile and pressure profile, was indicative of two key points. First of all, this hinted that the MR of the tools most likely, obeyed Preston's law of MR. In other words, the MR was directly correlated to pressure. Furthermore, it showed the potential of the FEM in predicting polishing outcomes of these tools. The FEA can be employed as powerful aid, in future fiber tool designs, as a consequence of the validity of the model.

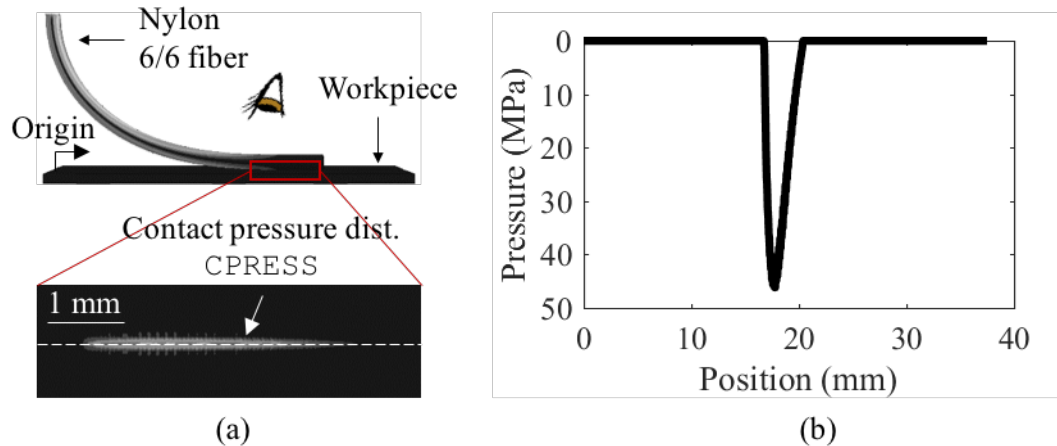


Figure 3-8 Nylon 6/6 fiber-workpiece interaction FEM (a) contact pressure distribution (CPRESS), (b) pressure profile extracted from CPRESS along the dashed line

Figure 3-9(a) shows the pressure distribution of the same Nylon 6/6 fiber, tilted at 40° , on a planar surface. The pressure profile from the centerline of the pressure distributions is illustrated in Figure 3-9(b). The pressure profile suggested that tilting the fiber had indeed reduced the maximum contact pressure. The MR testing results of this tool is presented in Chapter 4 as well.

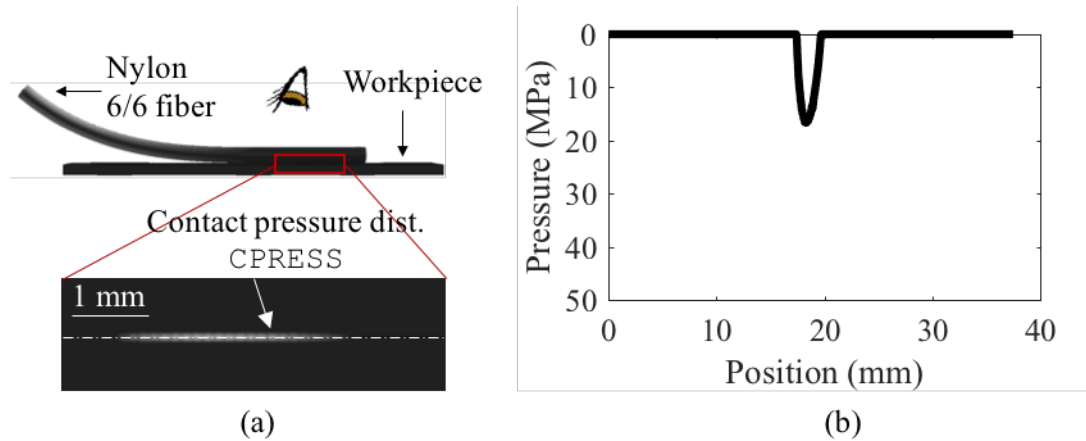


Figure 3-9 FEM of the tilted Nylon 6/6 fiber at 40° (a) contact pressure distribution (CPRESS), (b) pressure profile extracted from CPRESS along the dashed line

As it will be discussed in Chapter 6, the FEM lays the foundation for selection of fibers that promote higher MSF removal capability.

3.5.6 Model results (non-planar workpiece)

A similar FEM procedure to the one described above was used to model the fiber – workpiece interaction on a curved surface. The fiber was modeled with the same specifications detailed in the previous subsection. The workpiece was $\varnothing 75$ mm concave surface with ROC of 75 mm. To minimize simulation time, only an arc of the spherical workpiece was created in the FEM. The same idea of halving the fiber along its line of symmetry was employed. The C3D10M elements were used for the discretization of both fiber and the workpiece. a total 256,834 number of nodes and 166,952 number of elements were created. Figure 3-10(a) shows the engaged fiber with this workpiece as well as the contact pressure distribution of the fiber on the workpiece. Depicted in Figure 3-10(b), the pressure profile obtained from the FEM suggests that the width of the pressure profile is

narrower than that of the planar surface. Yet the profile has the same V-shaped geometry.

Testing on this sample will be done in Chapter 5.

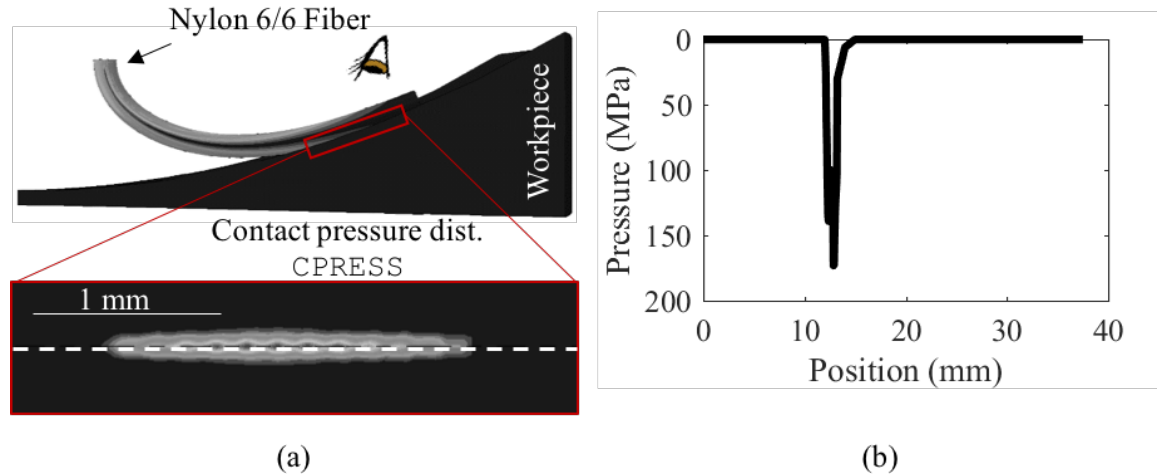


Figure 3-10 FEM of the Nylon 6/6 fiber-concave workpiece interaction; (a) contact pressure distribution (CPRESS), (b) pressure profile extracted from CPRESS along the dashed line

3.6 Summary

In summary of this chapter, initial steps in design, fabrication and characterization of fiber based tools were taken. The key highlights of this chapter were the following:

- Criteria for selection of fibers suitable for a fiber based tool were introduced.
- Based on the fiber selection criteria a group of fibers were procured and selected. The fibers had different materials (polymers, carbon fiber, ceramic), and dimensions (0.22 mm to 3 mm).
- A simple experimental setup for measuring the fiber characteristics was devised and employed. This setup enabled the measurement of fiber loads and approximate contact lengths.

- Two simple fiber based tool design and their fabrication steps was detailed.
- An FEM for better understanding the fiber workpiece interaction was created. This FEM was used for evaluation of the fiber contact pressure distribution on both planar and non-planar surfaces.

CHAPTER 4: MATERIAL REMOVAL TESTING AND MECHANISMS

4.1 Introduction

This chapter will discuss the initial polishing test outcomes with respect to three key topics; (1) the impact of fiber choice (geometry and material) on the material removal rates (MRR), (2) the effect of process kinematics on the MRR's, (3) the influence of abrasive particle size on the MR of the tools, (4) the material removal (MR) mechanism of fiber based tools, and (5) fiber based tools long term behavior and fiber wear.

4.2 Polishing Tools

The majority of the experiments were carried out using the FT-1 polishing tool configuration. However, testing with different tool configurations (FT-2 and FT-3) was done as well. The three tool designs are depicted in Figure 4-1. Figure 4-1(a) shows the FT-1 design, whereas Figure 4-1(b) is essentially the same tool with the addition of an inline slurry feed at the center. This tool is used for a group of experiments in the next chapter. Figure 4-1(c) depicts the FT-2 design. The FT-1 and FT-2 were discussed in the previous chapter. The FT-3 design, see Figure 4-1(d), is very similar to the FT-2 design, in a sense that the fibers are tilted relative to the tool axis. The direction of the tilt, however, is opposite to that of FT-2 tool. This design was inspired by the fact that it can provide a tool with a smaller footprint relative to the FT-1 and FT-2 configurations.

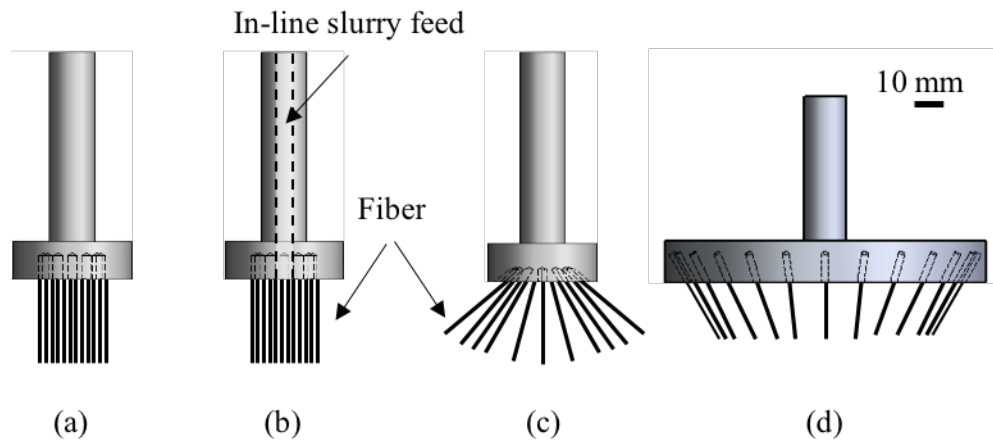


Figure 4-1 Fiber based tool designs (a) FT-1, (b) FT-1 with inline slurry feed (c) FT-2 (d) FT-3

The tools used had a variety of fibers sourced in Chapter 3. In all tests, there was no tool translation, just rotation about its center, i.e. spot test.

4.3 Polishing Experimental Testbed

For the purpose of evaluating the MR of the tools, a new experimental setup was devised. The setup consisted of the workpiece that was submerged in a bath of slurry. Details of slurries used are given for each test in the relevant sections. The tool was attached to a Bridgeport milling machine. The tool was brought into contact with the workpiece by adjusting the height of the machine tool-head, the z axis. The exerted loads by the tool on the workpiece was measured by placing an OHAUS Navigator XT[®] weighing scale with a resolution of 0.5 g, underneath the slurry bath. The scale had a load sampling rate of 10 Hz. Figure 4-2(a) shows the schematic of this test setup. As depicted in the figure the tool was rotated around its axis. The relative motion between the abrasive particles and the surface workpiece, caused by the tool rotation, promoted material removal from an annular

zone, where the fiber was in contact with the workpiece. A picture of the actual tool in contact with a piece of float glass is shown in Figure 4-2(b).

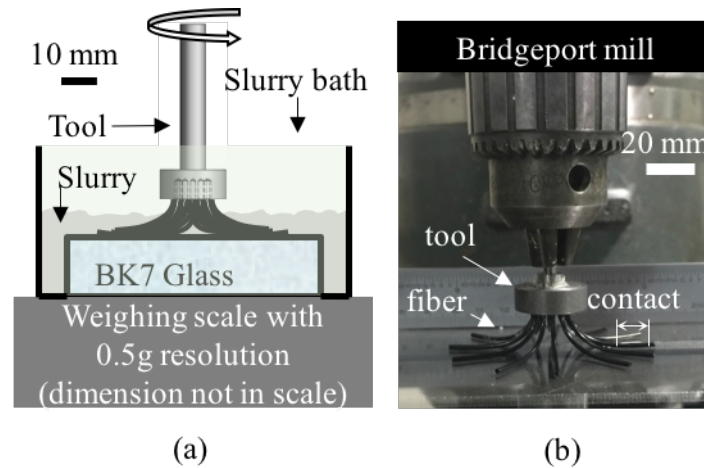


Figure 4-2 Polishing testbed; (a) schematic of a tool engaged with workpiece in the slurry bath (b) actual tool in contact with a planar surface

Prior to starting the polishing tests, the parts were centered with respect to the machine's spindle using a dial indicator with a resolution of $2.54 \mu\text{m}$. The relative tilt of the workpiece to the spindle was brought to below 0.02° , by placing aluminum foil underneath the slurry bath. The tilt of the part was measured using the same dial indicator as used for centering.

4.4 Workpiece Samples

Two types of BK7 glass samples were used. The first type were planar samples, (planarity better than $\lambda/4$, where $\lambda = 633 \text{ nm}$), with a diameter of 75 mm. These samples were used to evaluate a tool's MR profile and rate, and identify the key parameters affecting the removal rates, see sections 4.7.1 through 4.7.3, and section 4.8.1.

The second type of samples were the same $\varnothing 75$ mm planar samples which had concentric sinusoidal features machined onto their surfaces. These features were machined on a QED[®] Q-22 XE MRF machine. The fabricated sinewave had a wavelength of 2 mm and a peak-to-valley (PV) of 100 nm. This sinewave offered a different level of interaction between the polishing components, i.e. fiber, abrasive, and glass workpiece, whereby enabling the understanding of the fundamental interaction between the polishing components. In section 4.8.2, it is shown that polishing the BK7 sample containing the sinusoidal features resulted in different fiber-workpiece-abrasive particle interactions as a corollary of the height difference between the peaks and valleys of the features.

4.5 Polishing Slurries

The majority of the polishing tests were conducted with a commercial polishing slurry, Hastilite PO[®] slurry, manufactured by Universal Photonics[®]. Hastilite PO[®] is a ceria based slurry and 90% of the ceria particles have a diameter smaller than 1 μm , while the remaining are as large as 4 μm [131]. The slurry provides a favorable chemical environment for polishing glass and producing specular surfaces on glass with this slurry can be achieved. The slurry was diluted with water with 10:1 volumetric ratio (10 parts water 1 part slurry). In addition to the Hastilite PO[®] slurry, some other ceria and silica based slurries were used. The details of those slurries are given in the relevant sections.

4.6 Supporting Metrology¹

All BK7 samples were measured interferometrically. The instrumentation used is to enable the evaluation of two different scale of features. The larger scale features on the

¹For more details look at Appendix A

part, for the quantification of process outputs such as volume of removed material and process widths. The smaller scales are used to measure the surface roughness of the samples before and after polishing.

4.6.1 Measuring volume of removed material and process widths

For quantification of the first group of metrics, the samples are measured with a Zygo Verifire AT1000 laser Fizeau interferometer with a 101.6 mm aperture size, and a detector size of 1000×1000 pixels. This was achieved through subtracting the “pre-polishing” from the “post-polishing” interferogram. Since all the parts used in this section consist of planar geometries, the only processing to the measurement data is the removal of a best fit plane from the raw measurements.

4.6.2 Surface roughness

For the quantification of surface texture of the polished parts, two scanning white light interferometers (SWLI) were used. A Zygo ZeGage SWLI using a 20× Mirau objective, with a field of view (FOV) of $417 \mu\text{m} \times 417 \mu\text{m}$, and a 1024×1024 pixels detector size was used for the measurement of the surface roughness of the polished samples.

For measuring the peaks and valleys of the sine wave on the BK7 glass sample with concentric sinusoidal features, the Zygo NewView 5000 is used. The instrument has a 10× Mirau objective with a FOV of $830 \mu\text{m} \times 830 \mu\text{m}$, and a 640×480 pixels detector size. This instrument is equipped with an automated stage facilitating the automatic measurement of multiple sequential peaks and valleys. The data obtained through both of the SWLI instruments were subject to removal of a best fit 4th order polynomial.

4.7 Material Removal from Planar BK7 Samples

To give an introduction on the process metrics, the results from a typical MR test is depicted in Figure 4-3. The polishing test, was carried out on BK7 glass, for 10 minutes with the tool rotating at 100 RPM spindle speed. The polishing tool, comprised of thirteen Nylon 6/6 fibers with a length of 37.5 mm (tool FT-1-2 in Table 4-1). The polishing slurry was the Hastilite PO[®] slurry.

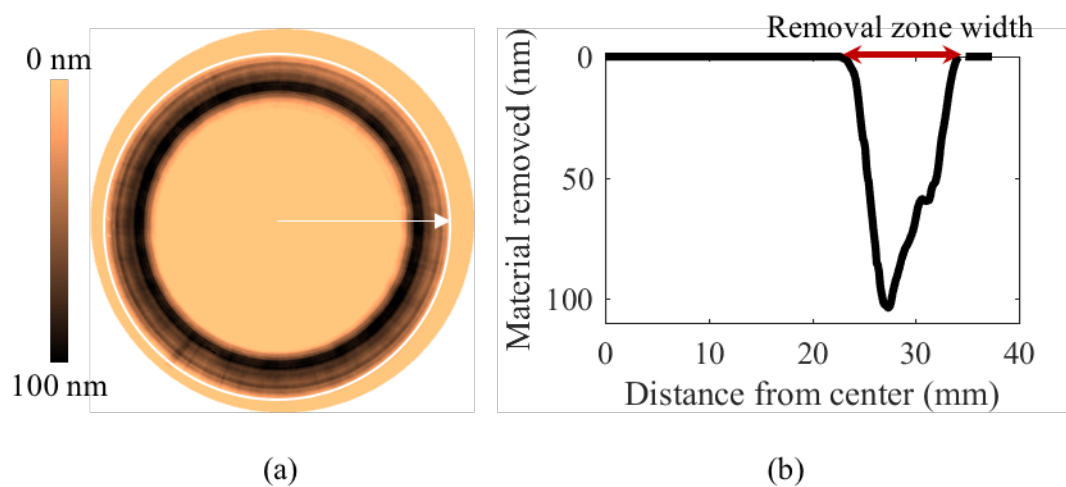


Figure 4-3 Material removal from BK7 glass using thirteen fiber Nylon 6/6 tool; (a) Fizeau interferogram (b) radially averaged profile of the Fizeau interferogram

Figure 4-3(a) shows the Fizeau interferogram of the polishing test. As expected, material was removed from an annular region. Figure 4-3(b) illustrates the radially averaged profile of the Fizeau interferogram, where process widths and depth of removal can be seen. The process width, the material removal rate (MRR), and MRR/Fiber are the main process metrics used in the following sections. MRR is the total volume of removed material per unit of time, whereas MRR/Fiber is MRR divided by the number of fibers in the polishing tool. For evaluation of total MR volume, the area under the radially averaged

profile, was calculated. This area was then rotated 360° about the center of the polished annulus and the resulting volume was the total volume of removed material. The width of the removal zone in the averaged profile was deemed as the process width.

The removal profile in Figure 4-3(b) shows the existence of a V-shaped MR profile. Comparing this result to the FEM pressure distributions (see Chapter 3, section 3.5.5), also V-shaped, confirms the validity of the FEM as well as suggesting that the MR is driven by the applied pressure of the tools.

In the following subsections results with respect to the material removal of fiber based tools from planar BK7 glass will be reported. At each subsection, the aim was to investigate the impact of a specific fundamental parameter on the MR characteristic of fiber based tools. The parameters include fiber type, fiber count, process kinematics (load and velocity), and abrasive particle size.

4.7.1 MRR of fiber based tools using different fibers

For investigating the impact of fiber type on the MRR of the fiber based tools, the FT-1 design was used. The fibers introduced in the previous chapter, see Table 3-1, are tested for this study. Table 4-1 lists the tools made for the purposes of this section. All the tools were in the same FT-1 configuration (see Figure 4-1 for the tool design).

Table 4-2, contains the group of experiments conducted with the tooling introduced in Table 4-1. The table also contains information on the slurry used, process kinematics, and the total polishing time. The workpiece used for all of the tests were the planar BK7 glass samples.

Table 4-1 Tools used for the MRR vs fiber type experiments

Tool name	Fiber			
	Material	Geometry	Length (mm)	Number/tool
FT-1-1	Copolymer	Ø1.4 mm	37	15
FT-1-2	Nylon 6/6	Ø1.6 mm	37	13
FT-1-3	Polypropylene	Δ, 1.2 mm/side	37	12
FT-1-4	Copolymer	Ø0.5 mm	37	58
FT-1-5	Composite	1 mm × 0.1 mm	37	12
FT-1-6	Silicon	Ø1.3 mm	37	12
FT-1-7	Polyurethane	2 mm × 0.6 mm	37	12

Table 4-2 Testing conditions for evaluation of MRR vs fiber type

Tool name	Slurry	Tool RPM	Load (N)	Polishing time (min)
FT-1-1	Hastilite PO	100	10.2	10
FT-1-2	Hastilite PO	100	4.4	10
FT-1-3	Hastilite PO	100	3.92	10
FT-1-4	Hastilite PO	100	0.71	10
FT-1-5	Hastilite PO	100	4.34	10
FT-1-6	Hastilite PO	100	0.38	10
FT-1-7	Hastilite PO	100	1	30

Figure 4-4 shows MRR/fiber of the tooling used for the experiments listed in Table 4-2. The results are normalized with respect to the MRR/fiber of the FT-1-3 since it had

the highest MRR/fiber amongst all the fibers. This use of MRR/fiber is justifiable since testing revealed that the MRR changes linearly with the number of fibers per tool, see section 4.7.3.

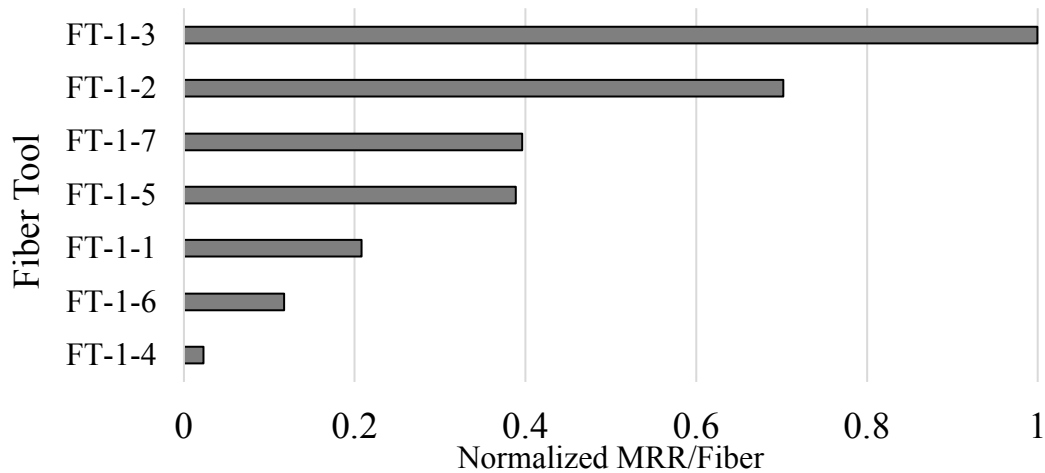


Figure 4-4 Normalized MRR/fiber of the fiber based tools listed in Table 4-1

As it can be seen in Figure 4-4, each fiber type had a very different MRR/fiber. The main attributes that can cause these differences were speculated to be the fiber geometry and fiber material. Both of these properties can affect the process width as well as the total load exerted by the fiber. Finding a direct correlation that would explain these differences, would be of great difficulty. This is due to a number of unknown properties associated with each fiber, such as fiber wettability, fiber creep behavior, fiber hardness, etc. Finding the correlation that would quantify and predict the MRR of a fiber based on material properties and fiber geometry is the subject of future work.

The information obtained from these tests isolates the fibers that provide relatively higher MRR's. The T-fiber and Nylon 6/6 fiber, for this reason, were chosen for the majority of the work in this dissertation.

4.7.2 MRR of the Nylon 6/6 fiber vs process kinematics (load and velocity)

To verify the connection between the MRR of a fiber based tool (Nylon 6/6) with the process kinematics, i.e. pressure and velocity, a range of tests with different spindle speeds and loading conditions were conducted. The tool has twelve Nylon 6/6 fibers, with each fiber being 37.5 mm long. The slurry used for the testing is Hastilite PO slurry. The aim of these tests was to, first, investigate whether these tools comply with Preston's law of MR, and if yes, what is the Preston coefficient for this particular tool. The testing conditions are provided in Table 4-3.

Table 4-3 Testing conditions for evaluation of MRR of the twelve fiber Nylon 6/6 tool vs process kinematics

Test#	Slurry	Tool RPM	Load (N)	Polishing time (min)
1	Hastilite PO	100	4.7	10
2	Hastilite PO	100	4.6	10
3	Hastilite PO	100	4.4	10
4	Hastilite PO	100	7.8	10
5	Hastilite PO	200	4.7	10

To ascertain the repeatability of the polishing outcomes of the Nylon 6/6 tool, Test 1, 2, and 3 were conducted at relatively the same conditions, see Table 4-3. As shown in Figure 4-5, the tool, appears to comply reasonably with Preston's law of MR. Yet it should be noted that the number of testing was very limited (five tests), due to the limited resources available. Extensive testing would be needed for further verification and a more accurate evaluation of the Preston's coefficient. The Preston coefficient obtained for this set of

experiments with the tool was estimated to be $0.17 \mu\text{m}^2/\text{N}$. This value is on the lower end for typical polishing pad and pitch tools, reported in several references between 0.1 to $2 \mu\text{m}^2/\text{N}$ [32, 33, 132]. This is most likely due to the different removal mechanism of fibers. The active area within a Nylon 6/6 fiber is limited to a narrow line of contact, whereas in a polishing pad the active area is the entire area of the pad.

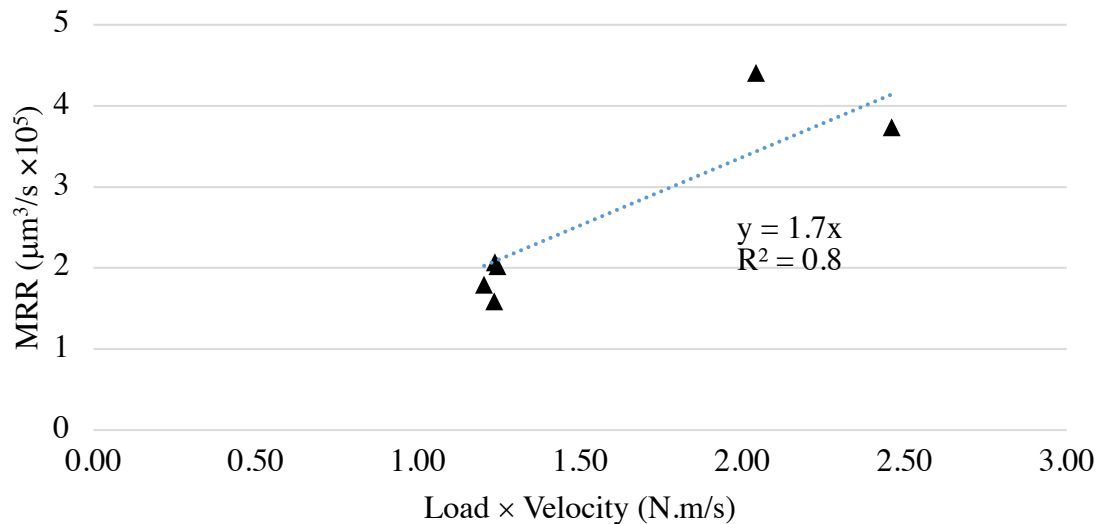


Figure 4-5 MRR vs Load × Velocity of the twelve fiber Nylon 6/6 tool

It should also be noted that the MRR of fiber based tools is significantly less than conventional pad tools. Based on previous experimental tests conducted by UNCC student M. Marcos [133], using a UNINAP-1 pad an $\varnothing 10$ mm tool on Fused Silica glass with the Hastilite PO[®] slurry, MRR of the order of $8 \times 10^5 \mu\text{m}^3/\text{s}$ was achieved. The MRR with the Nylon 6/6 tool revolves around $2 \times 10^5 \mu\text{m}^3/\text{s}$ from BK7 glass. This suggests a 75% less removal than a pad with a comparable footprint (but much larger contact area).

The fiber based tools polishing process, like any other polishing process, heavily relies on the polishing loads and relative velocities. Investigation on the Nylon 6/6 tool

revealed that this particular fiber, reasonably complied with the widely accepted Preston's law of MR. The similar shape of the V-shaped pressure profile from the FEM and the MR profile, also, supports this notion. For sure to comprehensively prove the Prestonian behavior of these tools, a large number of testing would be required. The results obtained here, nonetheless, can be used for prediction of total MR as the load or velocity change

4.7.3 MRR/fiber of fiber based tools vs fiber number/tool

Two different fibers were tested. For each fiber two tools with different fiber numbers were fabricated, i.e. a total number of four tools were tested. The tools are listed in Table 4-4. The testing for each tool was conducted for 10 minutes and a spindle speed of 100 RPM. The slurry used was the Hastilite PO slurry, and the samples were the planar BK7 glass.

Table 4-4 Fiber based tools used for testing MRR/fiber vs fiber number/tool

Tool name	Fiber			
	Material	Geometry	Length (mm)	Number/tool
FT-1-1	Copolymer	Ø1.4 mm	37.5	15
FT-1-8	Copolymer	Ø1.4 mm	37.5	8
FT-1-2	Nylon 6/6	Ø1.6 mm	37.5	13
FT-1-9	Nylon 6/6	Ø1.6 mm	37.5	6

Figure 4-6 depicts the MRR/fiber of the tools listed in Table 4-4. The MRR/fiber closely matched in both cases suggesting the independent behavior of fibers within one given tool. Discussed in the previous section, fiber based tools have a relatively low MRR than that of conventional polishing tools. Based on the results presented in sections 4.7.2

and 4.7.3 two immediate solutions for enhancement of the MRR of a fiber based tool are available; (1) Increasing the number of fibers per tool, and (2) change in process kinematics.

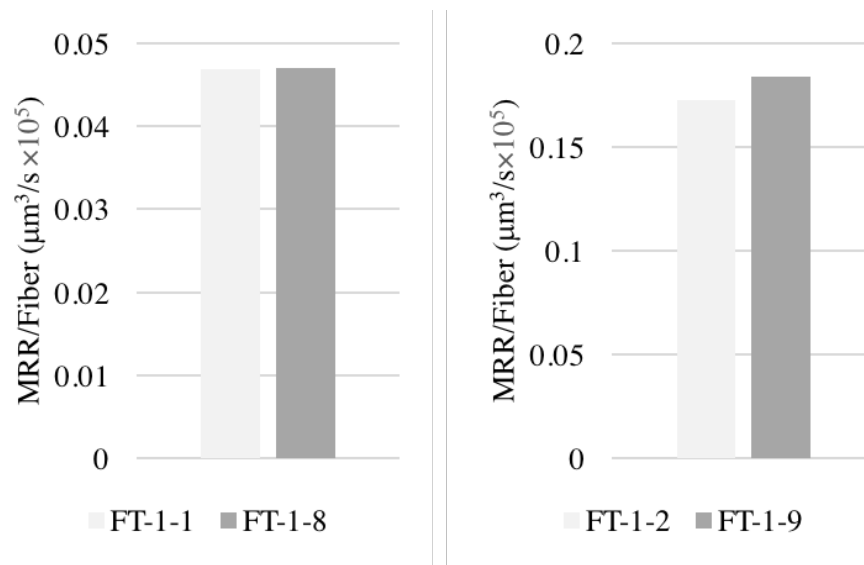


Figure 4-6 MRR/fiber for tools with different fiber number/tool listed in Table 4-4

4.8 Fiber Based Tools Material Removal Mechanism

The contact area of the fibers used in the fiber based tools are much smaller than conventional polishing tools. This implies that the number of abrasives imbedded in the fibers are very small, if any. However, the fibers are capable of entraining abrasive particles at their leading edge. The combined effect of the fiber down-force on the entrained abrasives towards the workpiece surface, and the wiping motion of the fiber is believed to contribute significantly to the removal of material off the workpiece surface. As a consequence of this removal mechanism, the removal zone should not be restricted to a region where the fiber is in physical contact with the workpiece. Indeed, any opening between the fiber and the workpiece smaller than the abrasive particles should be capable of entraining the particles. To better illustrate this description, Figure 4-7(a) shows a Nylon

6/6 fiber in contact with a planar workpiece. Figure 4-7(b) is the close up of the fiber in physical contact with the workpiece. Based on the MR mechanism of fiber based tools, the removal zone is not limited to the region termed as “actual contact” in the figure. Any region where the gap between the fiber and the workpiece is smaller than the abrasive particle size should contribute to the removal zone. Figure 4-7(c), shows these regions termed as “effective contact 1” and “effective contact 2” for two different particle sizes. It is expected that a slurry with smaller abrasives to have a smaller process width, than that of a slurry with larger particles, i.e. “effective contact 1” < “effective contact 2”.

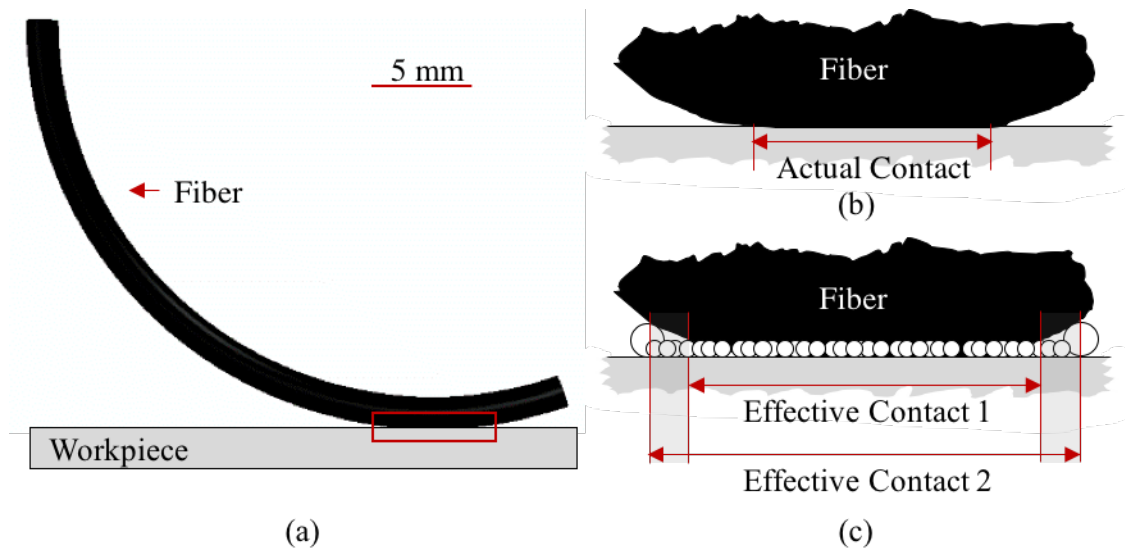


Figure 4-7 (a) fiber – workpiece engagement (b) fiber – workpiece contact close up in the absence of abrasive particles (c) fiber – workpiece – particle interaction and the impact of particle size on process width i.e. Effective Contact

The material removal mechanism of fiber based tools, is backed by both FEM and experimental evidence. In the FEM, a parameter called *COPEN* exists, that essentially quantifies the gap between the fiber and workpiece near the contact zone, i.e. where *CPRESS* \neq 0. The actual contact, in FEM, was evaluated by measuring the length of the

pressure profile, 3.75 mm for the Nylon 6/6 fiber. The length of the COPEN was subject to the same measurement for areas that report a gap smaller than the Hastilite PO[®] particle size ($\approx 1 \mu\text{m}$). This length was about 10.7 mm. This length is much closer to the process width, i.e. “effective contact” length, which was about 13.4 mm, thus confirming the association of zones with openings smaller than the particle size with the process width’s. For the details of the FEM look into Chapter 3.

4.8.1 Process width of the Nylon 6/6 fiber vs slurry abrasive particle size

To experimentally verify the MR mechanism theory the twelve-fiber Nylon 6/6 tool was used for polishing planar BK7 glass samples. The testing was conducted using polishing slurries with different abrasive particle sizes. Information about these polishing slurries are provided in Table 4-5. The slurries had different chemical influences on glass. Nevertheless, no MR would be expected, in the absence of any mechanical means, i.e. the fiber – particle interaction. The chemical aspect of the slurry will affect the depth of the MR profile. However, this aspect was not fully explored here.

Table 4-5 Polishing slurries used for quantifying the process width vs particles size of the abrasives

Ref	Slurry name	Dilution Vt%	Particle type	Particle size
A	Hastilite [®] PO	10:1 H ₂ O	Ceria	1 μm
B	UltraSol [®] Optiq	10:1 H ₂ O	Ceria	0.40 μm
C	NanoTek [®] CE 4086	10:1 Ionized H ₂ O	Ceria	0.04 μm
D	UltraSol [®] S39	N/A	Silica	0.11 μm
E	UltraSol [®] 250K	N/A	Silica	0.02 μm

The testing conditions associated with each slurry in Table 4-5 are provided in Table 4-6.

Table 4-6 Testing conditions for polishing BK7 glass using twelve fiber Nylon 6/6 tool for evaluation of the process widths vs slurry particle size

Slurry	Particle Size (nm)	Tool RPM	Load (N)	Polishing time (min)
A	1000	100	4.7	10
B	400	100	4.6	10
C	110	100	4.4	60
D	40	100	4.3	60
E	20	100	4.7	60

The results of the testing, depicted in Figure 4-8, clearly indicated that the process width decreases with the decrease in the slurry particle size. This result supports the MR mechanism theory of the fibers postulated at the beginning of this section.

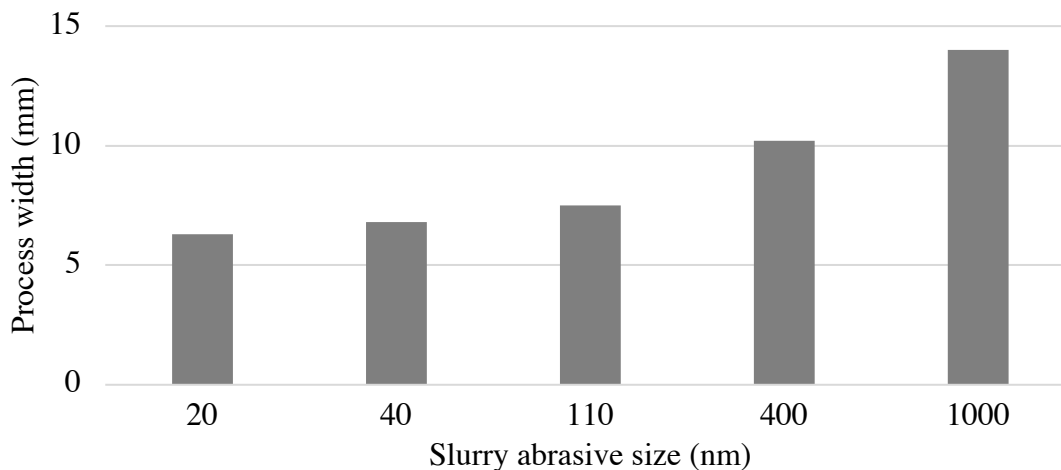


Figure 4-8 Process width vs particle size for 12-fiber Nylon 6/6 tool

4.8.2 Fiber preferential impact on periodic surface features

In a second group of testing, the planar BK7 sample that contained concentric sinewave features was used. Figure 4-9(a) shows the Fizeau interferogram of the sample. The goal of this test was to provide further evidence on the MR mechanism theory, in the sense that the fiber will be interacting with peaks and valleys of the surface sinewave features differently, see Figure 4-9(b). A close up of this interaction depicted in Figure 4-9(c), revealed that the fiber is likely to impact both regions, if a slurry with large abrasives is used, i.e. Hastilite PO (particle size $\approx 1\mu\text{m}$). Using a slurry with smaller abrasive particles, i.e. UltraSol[®] 250K (particle size $\approx 20\text{ nm}$), will most likely result in a much more preferential impact, on the peaks, and the particles will freely roll beneath the fiber in the valleys.

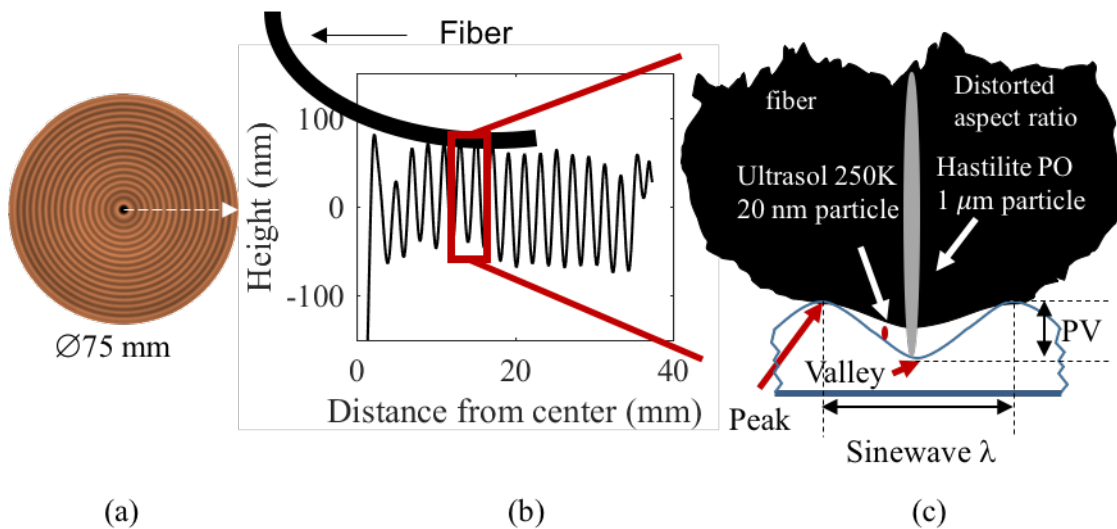


Figure 4-9 Fiber interaction with BK7 sample contacting concentric sinusoidal features;

(a) BK7 sample interferogram, (b) fiber interaction with the sinewave, (c) fiber interaction with the sinewave and two different particle sizes close-up

A twelve-fiber Tfiber (triangular cross section) tool was used for the polishing of the BK7 sample. The spindle speed was at 100 RPM, and for a total polishing time of 60 minutes. The UltraSol® 250K was used as the polishing slurry.

The Zygo NewView 5000, was used to measure 12 peaks and 12 valleys at the locations that were polished during the testing. The difference in the surface texture measured on the peaks and valleys, should provide a numerical metric in comparing the effect of the process, on the regions.

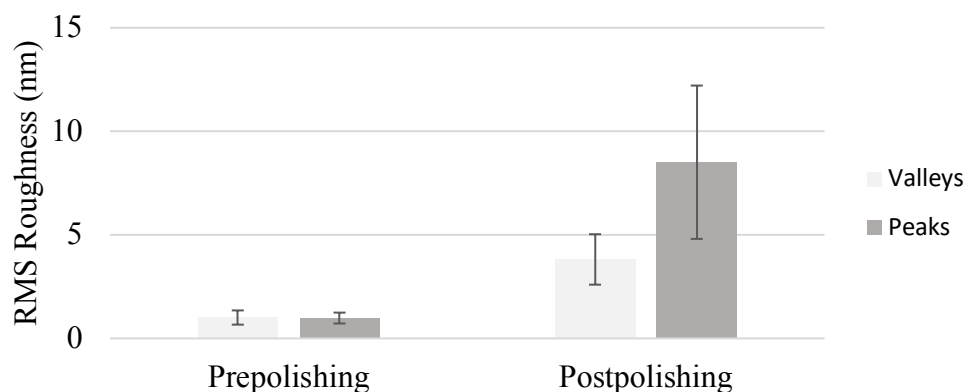


Figure 4-10 Peaks vs valleys surface roughness of the sinusoidal features, pre and post the polishing of the BK7 sample

Depicted in Figure 4-10, it is clear that RMS roughness values had a distinctly higher magnitude on the peaks than the valleys. The roughness values for both regions were in the same order of magnitude before the polishing. The interferogram obtained on the peaks showed the presence of deep scratches, see Figure 4-11(a). This is not the case for the interferograms of the valleys. The valleys, for the most measurements, had been chemically impacted and any deep scratches were absent, see Figure 4-11(b).

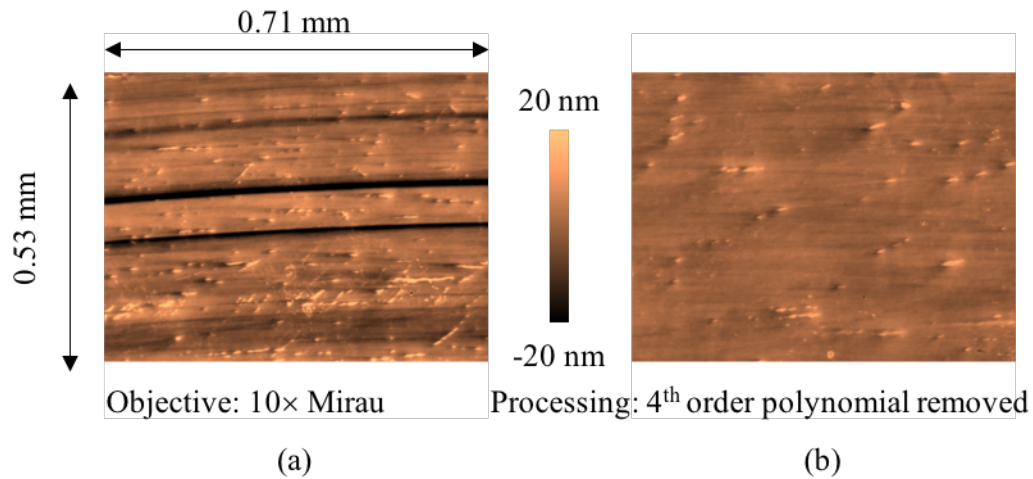


Figure 4-11 SWLI measurements of the BK7 sample containing the sinusoidal features;

(a) sample peak (b) sample valley of the sinewave

To summarize this section, the surface modification was at 3 times higher at zones that were suspected to have a higher interaction with the fiber. These zones, mainly, were at a higher elevation. This key result is pivotal in understanding the physics of MSF reduction as well. Generally speaking, the aim would be to achieve a state where the abrasive particles will roll underneath the fiber, without sustaining any significant force. This, in theory, means that the MRR should be much less at the valleys than that of the peaks where the abrasive particle is directly engaged with the workpiece through the load applied by the fiber. In chapter 6, this key conclusion will be leveraged in identification of fibers that could promote preferential MR from the higher zones of the MSF errors.

4.9 MR of the Nylon 6/6 Fiber Using FT-1, FT-2, and FT-3 Tool Designs

In addition to the FT-1 tool design, the other two configurations, i.e. FT-2 and FT-3, were fabricated as well. These designs are depicted in Figure 4-1. The tools used for the testing are listed below in Table 4-7.

Table 4-7 Testing conditions for the Nylon 6/6 fiber with three different tool designs

Tool name	Fiber			
	Material	Geometry	Length (mm)	Count
FT-1	Nylon 6/6	Ø1.6 mm	37	12
FT-2	Nylon 6/6	Ø1.6 mm	37	12
FT-3	Nylon 6/6	Ø1.6 mm	37	24

All three tests were conducted with a spindle speed of 100 RPM, using Hastilite PO[®] slurry, for 10 minutes. Three planar BK7 samples were polished with the tools.

The FT-2 provides lower polishing pressures. A linear trace off the Fizeau interferogram of the polished samples with the FT-1 and FT-2 tools are depicted in Figure 4-12(a), (b) respectively. The smaller process width of the FT-2 tool was in agreement with the FEM prediction results. The lower removal depth of the FT-2 tool validated the lower polishing pressures that has resulted in lower MR.

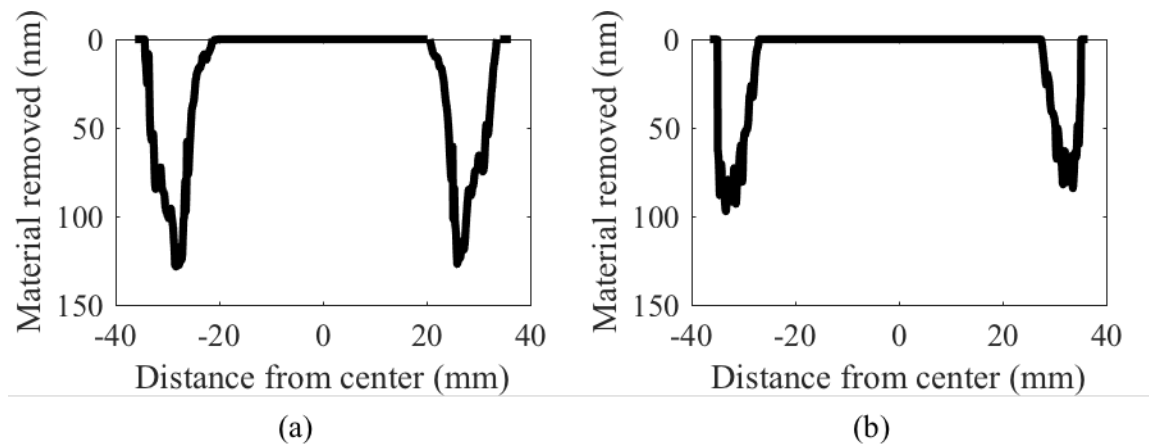


Figure 4-12 (a) MR spot for the FT-1 tool, (b) MR spot for the FT-2 tool

One of the key characteristics of a polishing tool is the footprint size. In this work, a very simple variant of the FT-1 tool, i.e. FT-3, was designed to obtain a smaller footprint. Acquiring a larger footprint size, seems to be much more trivial case in the sense that the position where the fibers are glued can be extended to a larger radius with respect to the tool axis. The FT-3 design, is a very simple alternative, where the direction of the bending of the fibers, is reversed inwards and towards the tool axis.

Figure 4-13(a), (b) shows the approximated tool footprint of the FT-1 and FT-3 tool respectively. As illustrated in the figure, FT-3 tool had the potential of a smaller footprint size for the Nylon 6/6 fiber.

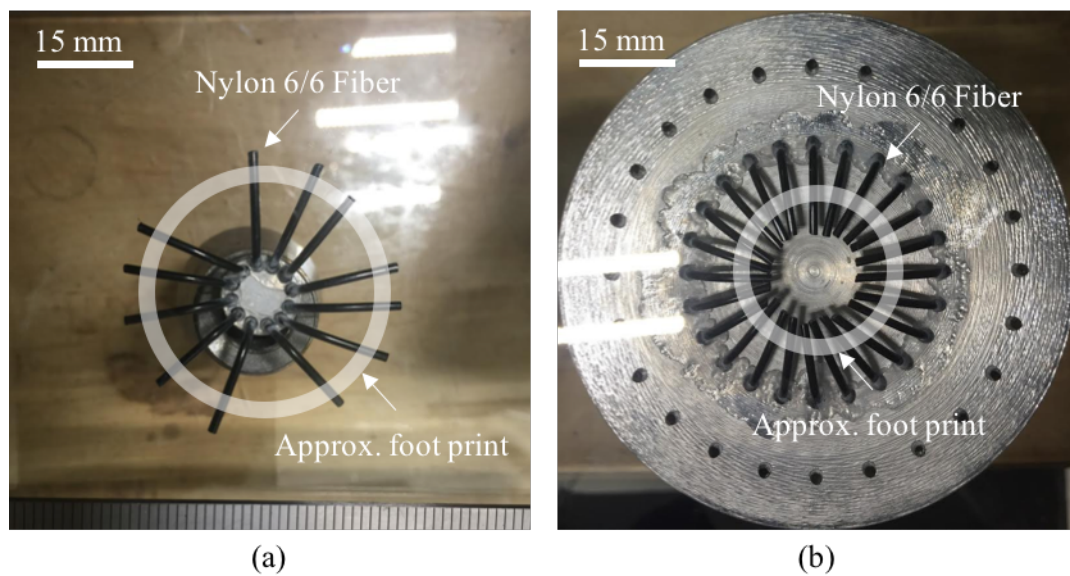


Figure 4-13 View from bottom of the engaged tools; (a) FT- tool (b) FT-3 tool

With this design, the smallest footprint achievable depends on the smallest circle where the fibers tips meet (Figure 4-13(b)). The approximate footprint size can be stated as:

$$tfps = R_m + P_w \quad [mm] \quad (4-1)$$

Where $tfps$ is the tool footprint size, P_w stands for the process width, and R_m is the radius of the aforementioned circle. This Radius can be calculated from Equation (4-4):

$$R_m = \frac{n_f D_f}{2\pi} \quad [mm] \quad (4-2)$$

Where, n_f is the number of fibers within the tool, and D_f is diameter of the fibers.

The MR testing of the tools in Figure 4-13, verified the potential of the FT-3 design in offering a smaller tool footprint. The results of such testing by extracting a linear trace from the interferograms are shown Figure 4-14(a), (b) for FT-1 and FT-3 respectively.

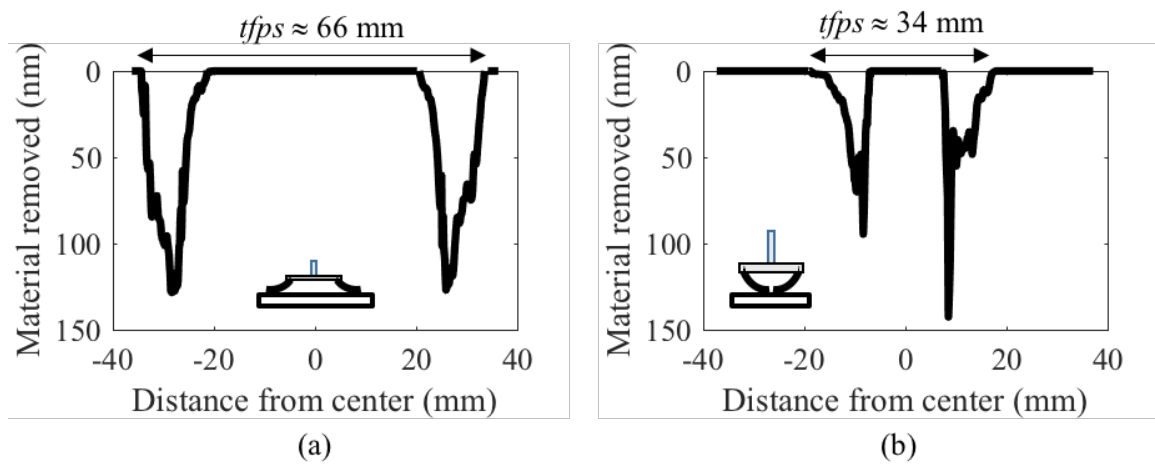


Figure 4-14 MR spot and comparison of tool footprint size; (a) FT-1 tool, (b) FT-3 tool

For the tool used in this test, 24 fibers were used. This gives an R_m value of about 6 mm. With an approximate process width of about 7 mm and a 3 mm of fiber tip dead zone, the tool footprint size is predicted about 32 mm. This is consistent with that obtained through the experimental evaluation. It should be noted that the peculiar artifacts on the removal profile can be mainly attributed to the housekeeping issues, such as the existence of coarse particles in the testing setup. This test was not repeated, as if this result was

mainly used to demonstrate as a proof of concept in achieving a smaller footprint with a simple tweak in the tool design.

4.10 Surface Finishes Achievable with Fiber Based Tools

The next topic is the final surface finish of a workpiece polished with fiber based tools. Surface finish results on the sinusoidal samples were discussed earlier. Two points should be raised with respect to that test; (1) the slurry used for polishing that sample did not contain the optimal chemistry for polishing glass. Hence the final finish of that piece, suffered from random chemical blemishes, degrading the surface finish values to numbers close to 10 nm rms. (2) The test was done with keeping the position of the tool fixed, i.e. spot test, which typically have worse finishes than the scenario with tool translation. To address the first issue, the surfaces polished with the Hastilite PO[®] slurry were measured. For the second point, in the next chapter results with lower roughness values for when the tool is translated on the surface will be presented.

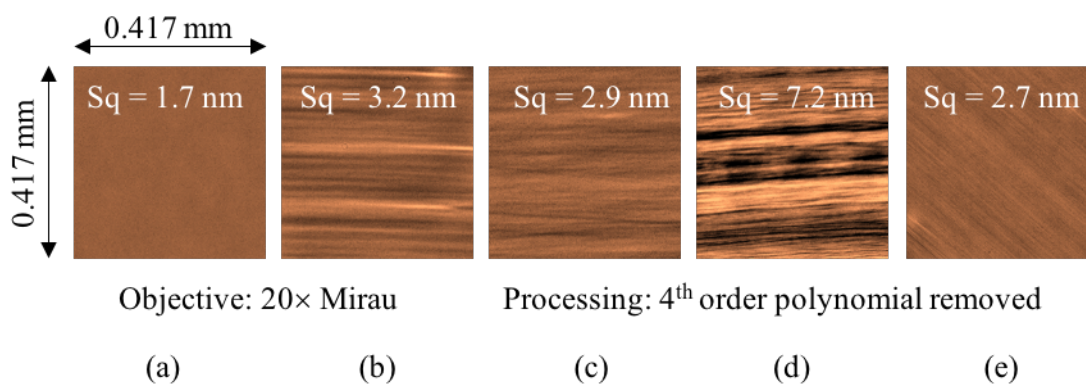


Figure 4-15 BK7 surface finish (a) before polishing, after polishing with (b) FT-1-3 (Tfiber) (c) FT-1-2 (Nylon 6/6) (d) FT-1-6 (composite) (e) FT-1-1 (Copolymer)

Using a 20× Mirau objective on the Zygo ZeGage SWLI, the BK7 glasses polished with the Hastilite PO[®] slurry were all measured. The surface finishes imparted by different fibers varied in the order of 2-3 nm RMS. Sample roughness measurements associated with the different fibers are depicted in Figure 4-15. The samples polished with the polymeric fibers had a better finish than of those polished with the composite fiber. The main reason for that is most likely to the different surface texture of the carbon fiber. The polymeric fibers all possessed smoother surfaces than that of the carbon fiber.

4.11 Fiber Based Tools Long Term Load Decay and Fiber Wear

Polishing optics, is typically a long and iterative process. Having tools that wear slower and sustain a stable tool influence function (TIF) over these long process times, is of great interest. In order to evaluate the long-term behavior of the fiber based tools, two metrics were investigated.

From the experimental results thus far, it is understood that the polishing load was one of the key parameters in material removal of the fiber based tools. The first metric in studying the stability of fiber based tools over long span of polishing times, was the drop in the load of the Nylon 6/6 tool over the course of 4.5 and 9-hour spot tests. The exerted load from the tool was continuously registered to the computer with the OHAUS Navigator XT[®] scale. The frequency of registration is 10 Hz.

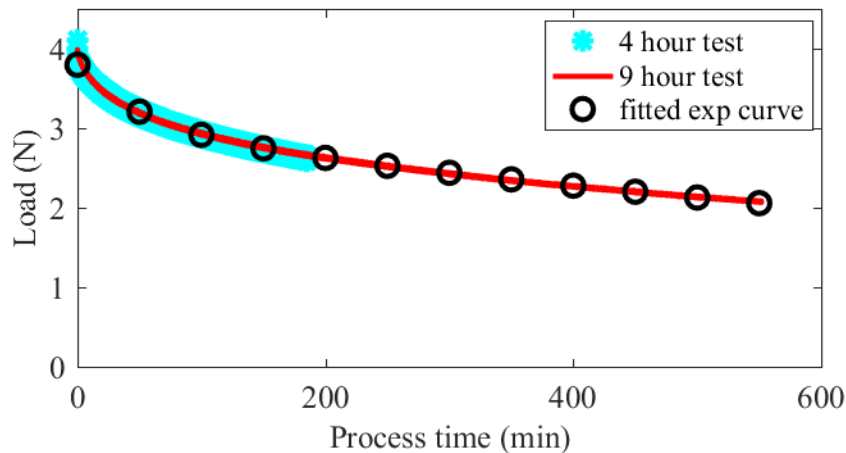


Figure 4-16 Load decay of the twelve fiber Nylon 6/6 tool over continuous polishing experiment

Figure 4-16 shows the behavior of two newly fabricated twelve-fiber Nylon 6/6 tools, over 4.5 hour and 9 hour tests. The tools tested in both case showed an exponential decay in their polishing loads. This exponential drop in load was most likely due to the mechanical creep of the fibers. Extensive research available in [134-136], showed an exponential relationship between stress and strain during constant application of a load to polymeric materials. This load drop had also been observed in discontinuous measurement of the loads. The load drop may be a problematic concern in the context of a stable TIF. This can be mitigated by setting a break-in period for each polishing tool. Taking a careful look at Figure 4-16, the load drop for the initial 20 minutes is approximately 25% which corresponds to around 1 N. this drop in the next 580 minutes is about 1 N (33%). So, assigning a break-in period for the Nylon 6/6 tool of 20 minutes will greatly ameliorate this issue. The other solution can be the addition of a “tool compensation” for the polishing operation. This can be realized by increasing the plunging depth (ΔZ) of the tool as polishing progresses with time. Finally maintaining the tools in a preloaded state can

further help this issue. This will cause the fibers to be in the plateau zone of the exponential graph, and thus exhibiting load drops with much lower rates.

One of the major issues that conventional pad tools suffer during the polishing is the wear of the pad surface. To measure the wear rates of the Nylon 6/6 fiber, the SWLI microscope was used. Interferograms of the surface of the fiber, before, and after 5.5 hours of polishing is shown in Figure 4-17(a), (b) respectively. The fibers had undergone polishing BK7 glass with the Hastilite PO® slurry for mostly spindle speeds of 100 rpm. The wear flats on the surface of the fiber was about 5 μm , where the wear flat refers to the depth of which the material of the fiber had been removed, see Figure 4-17(c). This is a very promising number, in the sense that enables the fibers to be used for very long polishing hours, without significant fiber wear.

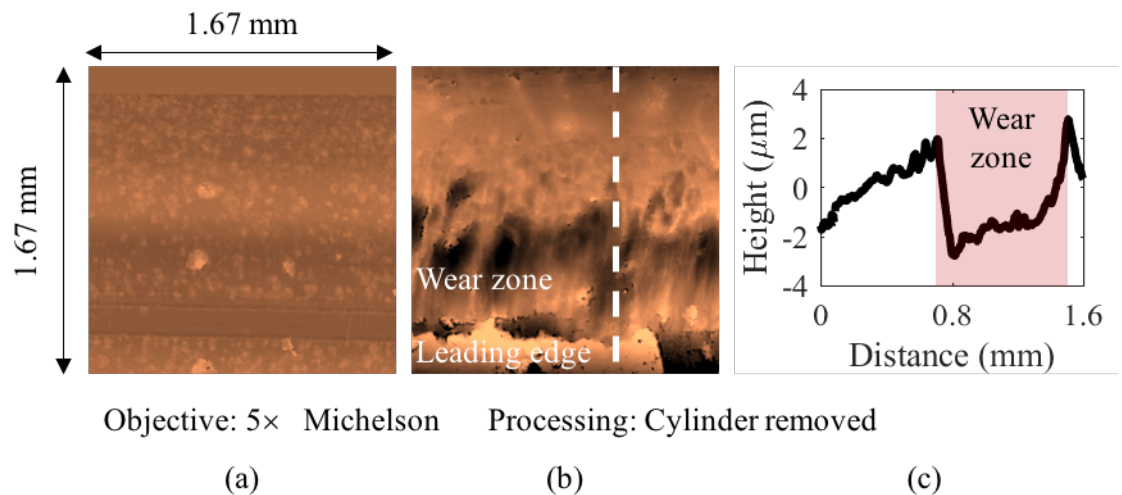


Figure 4-17 Nylon 6/6 fiber SWLI measurement; (a) unused fiber (b) worn fiber (after 5.5 hours) (c) profile across the dashed line on the worn fiber

4.12 Summary

In this chapter, extended testing with fibers, of different material, geometries and critical dimensions, showed the ability of fiber based tools in removing material from BK7 glass. The tests were aimed to seek the main parameters affecting the polishing outcomes. The most important highlights can be enumerated as follows:

- Fiber based tools appear to comply with Preston's law of material removal. The polishing testing with the Nylon 6/6 fiber suggested a reasonably linear relationship between the MRR of the tool and applied load times tool relative velocity. It was also noted that the MRR of fiber based tools were lower than comparable in size pad tools.
- The MRR/fiber of two different fiber based tools, was found to be independent of the number of fibers/tool. This result conveyed that each fiber within a tool behaved independently from the other fibers in the same tool.
- The material removal mechanism of fiber based tools was described. It was shown that the abrasive particles entrapped at the leading edge of the fiber and pushed down by the fiber towards the surface contributed mainly to the MR of these tools. The wiping motion of the fiber sweeping these entrapped particles caused the removal of material from the surface of the workpiece.
- Two alternative tooling designs were tested. It was shown that these designs can provide lower polishing pressures, as well as smaller tool foot print sizes.
- The surface finish of the BK7 glass samples polished with different fiber based tools were in the order of 3 nm RMS for the majority of the fibers.

- The long-term behavior of the polymeric fiber Nylon 6/6 was investigated. It was concluded that the tool has an exponential load decay behavior, and the magnitude of the drop is much larger at the beginning of the process. The fiber wear was also quantified. Fiber wear flats on the order of 5 μm over 5.5 hours which was a promising number, was observed.

CHAPTER 5: FIBER BASED POLISHING PROCESS

5.1 Introduction

This chapter details test results obtained when tool operated under translational conditions in a CNC machining center. For fiber based tools to be considered as a viable commercial tooling the following topics are addressed; (1) the fiber based tool's ability in operating under translational conditions is investigated, (2) fiber based tool's interaction with the workpiece edge and edge roll-off effects are scrutinized, (3) the stability of the MR profile overtime and the ability of producing a predicted form is studied, and (4) the extent of tool induced form and MSF errors is assessed.

5.2 Experimental Setups

5.2.1 3-axis CNC (submerged slurry bath)

The Haas[®] TM-1 machine at UNCC was used for testing the tools under translation. The CNC machine is depicted in Figure 5-1(a). To facilitate tool translation a larger slurry bath was fabricated. This new bath gives a working area of 275 mm × 260 mm, see Figure 5-1(b). The workpiece was fixed to the base of the slurry bath using Loctite[®] Super Glue. The specially sized grooves machined on the aluminum base, allowed the setup to be fixed on the table of the 3-axis CNC machining center. All of the MR experiments, in this setup, were conducted with the twelve-fiber Nylon 6/6 tool, and the Hastilite PO slurry diluted

with water (10:1 %Vt). The tool is depicted in Figure 5-1(c) engaged with a piece of BK7 glass.

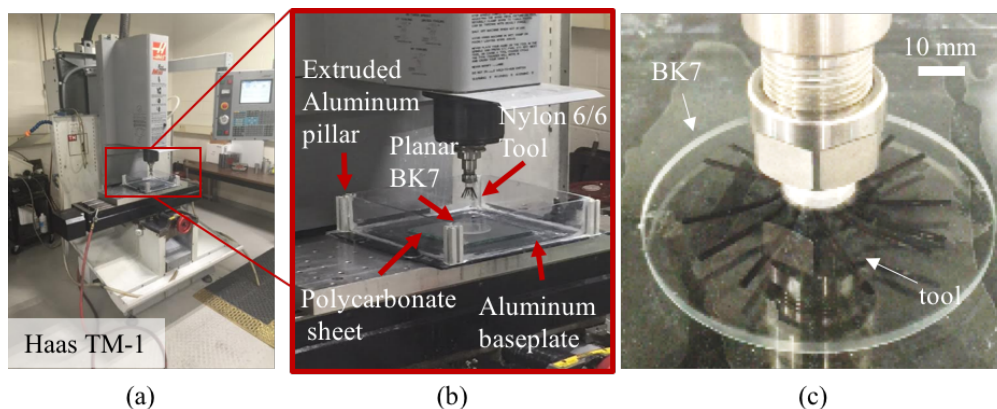


Figure 5-1 3-axis CNC setup; (a) Haas TM-1 machine tool, (b) test setup close-up (c) twelve fiber Nylon 6/6 tool engaged with planar workpiece

5.2.2 5-axis CNC (inline slurry delivery)

For testing the tools on non-planar samples, a 5-axis machining center was needed. This environment was provided by OptiPro[®] Systems. The polishing machine is an OptiPro Triumph, shown in Figure 5-2(a). Figure 5-2(b) shows a close up of the machine spindle and the twelve-fiber Nylon 6/6 tool engaged with a concave BK7 glass. The MR experiments in this setup was conducted with the twelve-fiber Nylon 6/6 tool as well. The polishing slurry used, was the UltraSol[®] Optiq (undiluted). This machine was located at OptiPro systems plant in Ontario, NY. A major difference between the setup used in the 5-axis machine and the 3-axis machine is the slurry delivery method. Contrary to the slurry bath used on the 3-axis system, a flood, recirculating delivery system was used whereby slurry was supplied by adjacent nozzles, and through the tool shaft with a feed rate of 5 l/min. the slurry was flooded through the delivery hose, as well as the center feed which was 6.35 mm vent drilled at the center of the tool. The parts were fixed to the specialized

chuck with a blocking pitch, 528 BLACK, made by Universal Photonics[®]. The part was preheated on a hot plate. Then using a butane torch, the pitch was continually applied on the chuck. The part was then placed on the chuck, and given time to completely adhere to the chuck

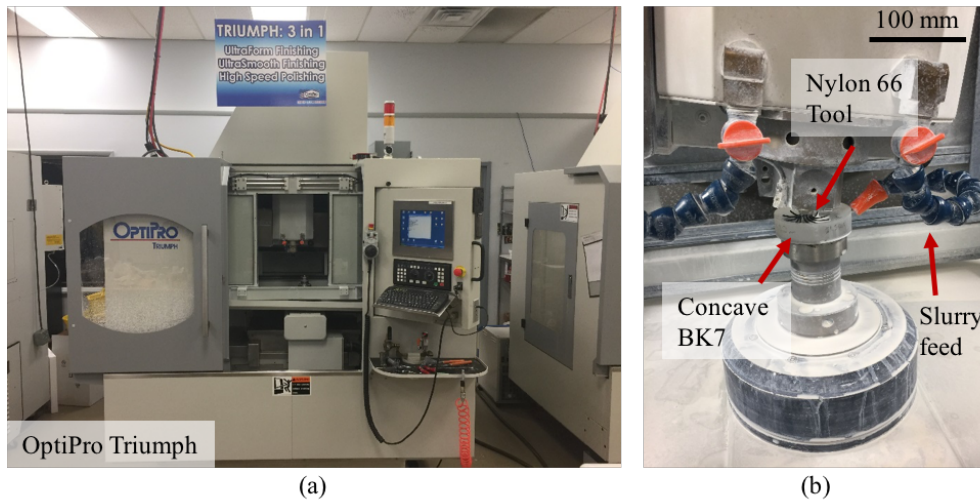


Figure 5-2 5-axis CNC setup (a) OptiPro Triumph machine (b) twelve fiber Nylon 6/6 tool engaged with concave workpiece

5.3 Workpiece Samples

Three different samples were used. Planar 250 mm × 125 mm, and 6 mm thick float glass plates were used to investigate the tool stability and ability to maintain its contact shape with the workpiece under translational conditions. The same samples were used for examining the behavior of the tool near the edge of the workpiece.

The same $\varnothing 75$ mm planar BK7 glass samples used in the last chapter were used to

- 1) compare the MR profiles as predicted by convolution to that experimentally obtained.
- 2) To evaluate the nature and extent of tool induced MSF errors. And 3) to quantify the MR volume of the tool in the system with inline slurry feed.

The third sample used is an $\varnothing 80$ mm concave BK7 glass with a radius of curvature (ROC) of 75 mm. The sample was fabricated by OptiPro[®] Systems. This sample was employed to evaluate the tool's performance on a non-planar surface.

5.4 Supporting Metrology

In addition to the metrology instruments used in Chapter 4, the OptiTrace[®] 5000, a contact profilometer with a 5 μm ruby tip was used. The instrument had a scan range of 150 mm and a vertical range of 12 mm. For the profiles measured with this instrument a best fit plane as well as a low-pass filter with a cut-off of 800 microns was applied. This instrument was used when large volumes of material was removed during the testing and the large slope values in the removal zones prevented the sample to be measured interferometrically.

To measure the concave BK7 glass interferometrically, a reference sphere with an aperture size of 101.6 mm and $f_{\#}$ of 1.5, on the Zygo Verifire AT1000 laser Fizeau interferometer was used. In addition to the removal of a best fit plane of the raw interferogram of the concave optic, the Zernike power term is also removed. The power term has the shape of a paraboloid where its maxima/minima is at the center of the interferogram, and its gradient vector at the maxima/minima is purely in the z direction. More information on the Zernike power term can be found in Appendix B.

5.5 Fiber Based Tools Translation on Planar Glass

The initial testing was to ascertain that selected fiber based tools had the ability to maintain their contact form on planar samples of float glass with a range of spindle speeds and tool feed rates. The tests were carried out on the 3-axis machine, and the slurry bath

was filled with water. This would enable the tool to run in a submerged configuration, and at the meantime visual observation of the interaction of the tool and the workpiece was feasible. Three tools were tested and are listed in Table 5-1 below.

Table 5-1 Tools tested under translational conditions on float glass

Tool number	Fiber			
	Material	Geometry	Length (mm)	Count
1	Nylon 6/6	Ø1.6 mm	25	12
2	PET	Ø0.22 mm	25	56
3	Polyurethane	2 mm × 0.6 mm	25	4

The tools were tested for spindle speeds from 100 RPM up to 1000 RPM, and with translational velocities from 1.5 mm/s up to 30 mm/s. All three tools, were successful in preserving their contact shape with the workpiece while traversing on the float glass. No fiber entanglement or pullout was observed. For spindle speeds larger than 500 rpm, the fluid adjacent to the tool was agitated aggressively and formed rapid vortices in the neighborhood of the tool. This would most likely change the dynamics of the fiber – particle – workpiece interaction. That said, the testing in the slurry bath are all under a spindle speed of 100 rpm since the majority of the spot tests were taken under this spindle speed. The remainder of this chapter will be exclusively dedicated to the results obtained with tool 1, i.e. twelve-fiber Nylon 6/6 tool.

5.6 Fiber Based Tools Behavior Near Workpiece Edge

5.6.1 Fiber disengagement and reengagement assessment

The effect of tool overhang off the edge of the workpiece on fiber disengagement, and of more importance, reengagement with the workpiece, was studied. The tool was translated along the edge of the workpiece with different fiber overhang values. The float glass sample with dimensions of 250 mm × 125 mm, was used. Figure 5-3 (a) and (b) depict cases where the fiber overhang values are 8 mm and 25 mm respectively. The fiber reengaged successfully with the workpiece in both scenarios. In the third case, see Figure 5-3(c), the outermost fiber on the tool is beyond the workpiece edge. Under such circumstance, failure in fiber reengagement with the workpiece, as well as occasional fiber pull out was observed. The initial tests suggested that successful reengagement of the fiber with workpiece usually occurs when the tool center is located as such that the outermost fiber is at least in line with the edge of the workpiece. In the tool depicted in Figure 5-3 the fibers were 6 mm away from the tool center. In case (b), the tool center was 6 mm away from the workpiece edge. In case (c), on the other hand, when the center was at 1 mm away from the edge, not all fibers had reengaged with the workpiece successfully.

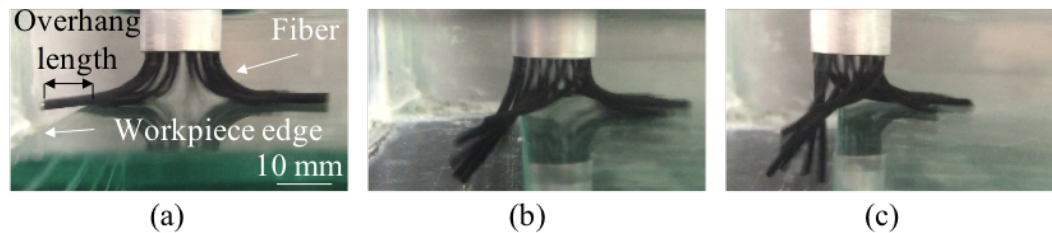


Figure 5-3 Twelve fiber Nylon 6/6 tool – workpiece edge interaction; (a, b) successful fiber reengagement (c) unsuccessful fiber reengagement

The other notable point is that, for some approximate overhang length of the tool (75% of the fiber length), extra features and notches were cut unto the surface of the fiber. While not verified, this was most likely due to the rougher surface of the ground edge and/or the sharp corner of the edge of the glass. These notches were speculated to affect the final finish of the part.

5.6.2 Quantitative evaluation of the twelve fiber Nylon 6/6 tool roll-off effects

Fiber based tools, like any other pressure based polishing tool, are likely to suffer from the edge roll off phenomena. Yet it was speculated that due to the tool architecture, each fiber behaves independently, thereby the roll-off zone near the edge would be much smaller than that of conventional polishing tools. Only the fibers at the workpiece edge would have a modified MR profile, and the tool foot print would be cropped as much as the overhang distance. While fibers fully engaged with the surface would be unaffected. Ideally the MR profile wouldn't be affected at all. Figure 5-4(a) shows the MR profile of the tool with no fiber overhang. Figure 5-4(b) illustrates the ideal case when the tool overhang had no effect on the MR profile, and the profile is cropped as much as the overhang.

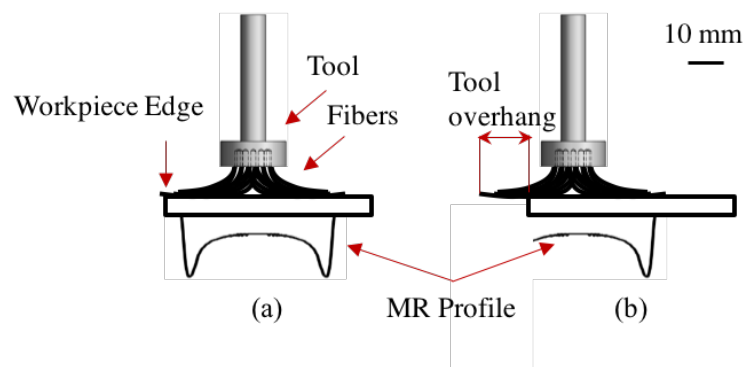


Figure 5-4 Nylon 6/6 tool MR profile near edge (a) with no fiber overhang (b) “ideal” scenario with tool overhang.

The same FEM described in chapter 3 was used to examine the evolution of the pressure distribution as the fiber was moved off the workpiece edge. To achieve these two changes were made to that model: 1) The fiber material was modeled with elastic properties and a Young's modulus of 2.27 GPa. 2) The fiber length was changed to 25 mm to reflect the fiber length used in the testing. Figure 5-5 shows three investigated cases. Each case contains a fiber with different overhang length.

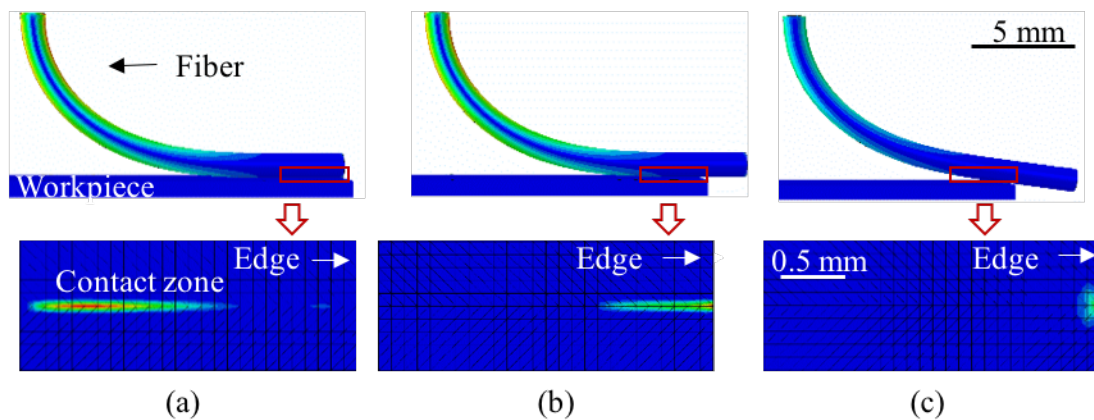


Figure 5-5 Nylon 6/6 fiber FEM near workpiece edge (a) 0 mm fiber overhang, (b) 3 mm fiber overhang, (c) 5 mm fiber overhang

Figure 5-5(a) shows the event where the fiber was adjacent to the edge and the overhang is 0 mm. The resulting pressure distribution exhibited the same V-shaped that was observed and explained in chapter 3. Figure 5-5(b) and Figure 5-5(c) depict cases where the fiber extended beyond the workpiece edge by 3 mm and 5 mm respectively. In the second case, i.e. Figure 5-5(b) the fiber was placed as such that both the non-contacting tip as well as half of the contacting length of the fiber were over the workpiece edge. As a result, the contacting region was halved, and the magnitude of the pressure had increased. In the third case, Figure 5-5(c), the fiber was moved even further and the fiber deformation

for maintaining the fiber tip along a line was no longer sufficient. the pressure distribution had shrunken to a very small area. The FEM suggested very high pressures in a zone 0.2 mm away from the edge. As a corollary of this localized high pressure, an area parallel with the edge and 0.2 mm thick will be non-functional. This mean that the clear aperture (CA) of the workpiece will be 0.4 mm less than the full aperture (FA). The 0.4 mm limiting CA is a very promising number, since 2-3 mm roll-offs are very typical values for conventional polishing tools [24, 25, 137, 138].

To experimentally verify the FE predicted result, tests were conducted on planar float glass plates. Three tests corresponding to the cases shown in Table 5-2, were done. In each test, the tool was translated along 100 mm of the plate edge to ensure the MR profile near the edge was not affected by the reversal motion and footprint of the tool. Details of the testing conditions are provided in Table 5-2.

Table 5-2 Testing conditions for evaluation of edge roll-off effects of the twelve fiber Nylon 6/6 tool on planar float glass

Test#	Tool RPM	Tool Feed	Slurry	Fiber overhang length
1	100	3 mm/s	Hastilite PO	0
2	100	3 mm/s	Hastilite PO	3
3	100	3 mm/s	Hastilite PO	5

The samples were measured before and after the polishing with the Fizeau interferometer and were subtracted from one another. Line profiles extracted from the subtracted Fizeau interferograms can be found in Figure 5-6. In the first two case, the FEM suggested that the tool shouldn't induce any edge roll off. For test 1, i.e. 0-mm tool

overhang (Figure 5-6(a)), the tool MR profile was unaffected. In test 2, i.e. 3-mm tool overhang (Figure 5-6(b)), the V-shape was truncated, as expected from the FEM. Finally, as the tool was shifted further to 5 mm tool overhang, the zone that exhibits high removals was as small as 0.5 mm. This implies that, the region that was considered as the region with edge roll off was as small as 0.5 mm. Also, equally important, the length of this zone was predicted by the FEM = 0.2 mm, adding more value and credibility to the model, not only for tool design guidelines, but also in predicting process outcomes, such as the one discussed here.

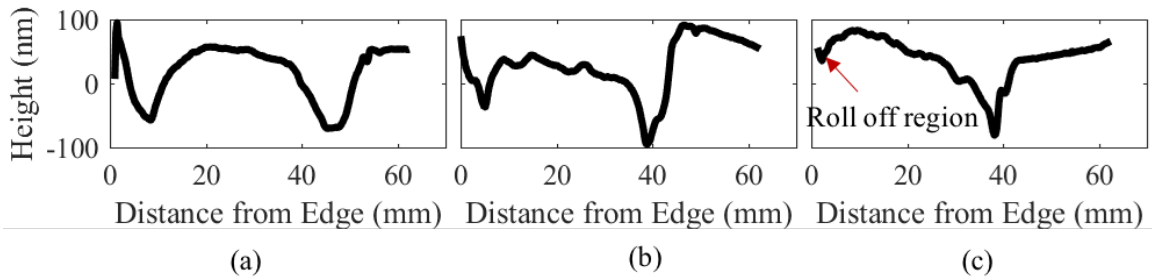


Figure 5-6 Twelve fiber Nylon 6/6 tool near edge removal profiles for tool overhangs of

(a) 0 mm, (b) 3 mm, and (c) 5 mm

5.7 Material Removal with Tool Translation in the Slurry Bath

One of the desired properties for a sub-aperture polishing tool, is a stable tool influence function (TIF), over long polishing periods. To quantitatively predict the MRR of the tool in translation, measurement of the TIF of the tool and basic mathematical convolution can be used. Theoretically the MR from any given point, e.g. u, v , is calculated whereby the convolution of the TIF and the dwell time function, as follows:

$$MR(x, y) = \iint D(u, v)TIF(x - u, y - v) du dv \quad [\mu m] \quad (5-1)$$

Where $D(u, v)$ is the dwell time function, i.e. the amount of time that the tool resides for any given point u, v . TIF is the TIF of the tool, i.e. MR profile of the tool per unit of time.

To acquire the TIF of this tool a MR from a spot was obtained on $\varnothing 75$ mm BK7 glass under 100 rpm spindle speed, 10-minute process time, and Hastilite[®] PO slurry. The sample containing the spot was measured before and after polishing with the Fizeau interferometer. Using fiducials on both the part and the measurement stage, it was diligently attempted to align the part with respect to a common coordinate system. The metrology data was transferred to MATLAB[®], where the before and after polishing interferograms were subtracted from each other to provide the tool's TIF. To minimize misalignment error further, the measurements were subtracted at small angle of rotations around the center of the workpiece at 5° with 0.1° increments. The angle where the subtraction map had the smallest RMS value was opted as the "optimal" angle. The subtraction map was then radially averaged. This averaged profile was next rotated around the center of the profile to obtain the new 3-D map representing the TIF of the tool.

Due to the large tool TIF size to workpiece size (55 mm to 75 mm) ratio, and to counteract any edge effects, a recess with a diameter of 75 mm was machined unto a polycarbonate sheet, as deep as the thickness of the BK7 part which is 4.35 mm. The BK7 part was inserted into this recess and the sheet will serve as a sacrificial surface. Two different tool paths were used here. A linear reciprocal path, see Figure 5-7(a), where the tool was traversed back and forth on a straight line, and a full raster path with a given stepover, see Figure 5-7(b).

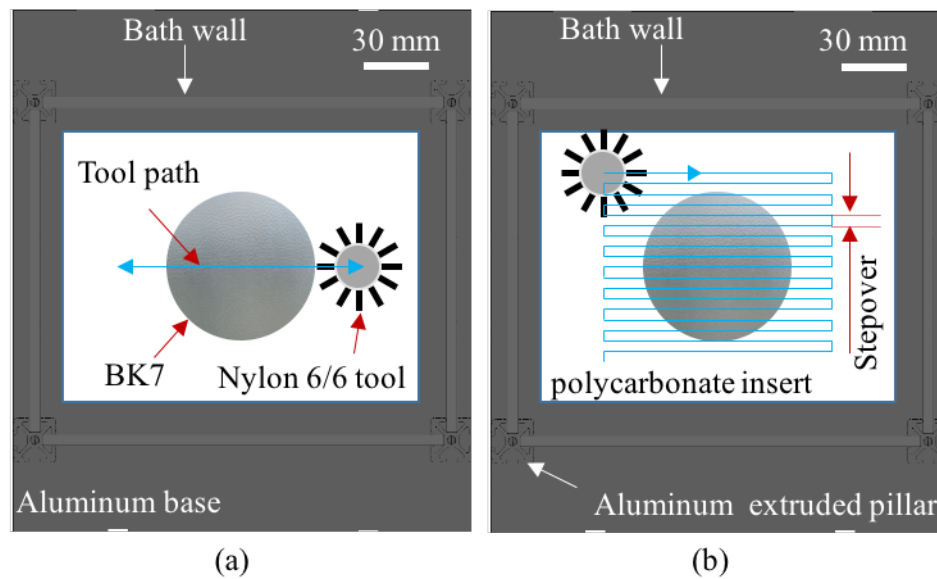


Figure 5-7 Polishing slurry bath setup (a) reciprocal tool path (b) raster tool path

5.7.1 Evaluation of total MR and MR profile shape of the tool with translation

To evaluate the total volume of MR and stability of the MR profile during translation, the reciprocal tool path was used, see Figure 5-7(a). The reasoning behind opting for the reciprocal tool path was that since the tool doesn't polish the entire workpiece, zones either side of the tool path exhibit no MR. Hence, these surfaces can be used as references for evaluation of the absolute MR values.

The test conditions for evaluating the absolute MR were at a spindle speed of 100 rpm and feedrate of 3 mm/s. The tool was reciprocated across the workpiece for 30 passes, giving a processing time of 43 minutes. The Hastilite PO[®] diluted with water, was used.

A uniform dwell time map was created on a straight line. The TIF of the Nylon 6/6 tool is then convolved with the created dwell time map. The surface map generated of such convolution is shown in Figure 5-8(a). Figure 5-8(b) shows the experimentally obtained post polishing surface interferogram. Linear profiles are extracted from both surface maps

and are depicted underneath their respective maps. The results showed that experimental removal profile shape greatly resembled that of predicted by convolution. Higher than expected removal volumes was achieved in the experimental test.

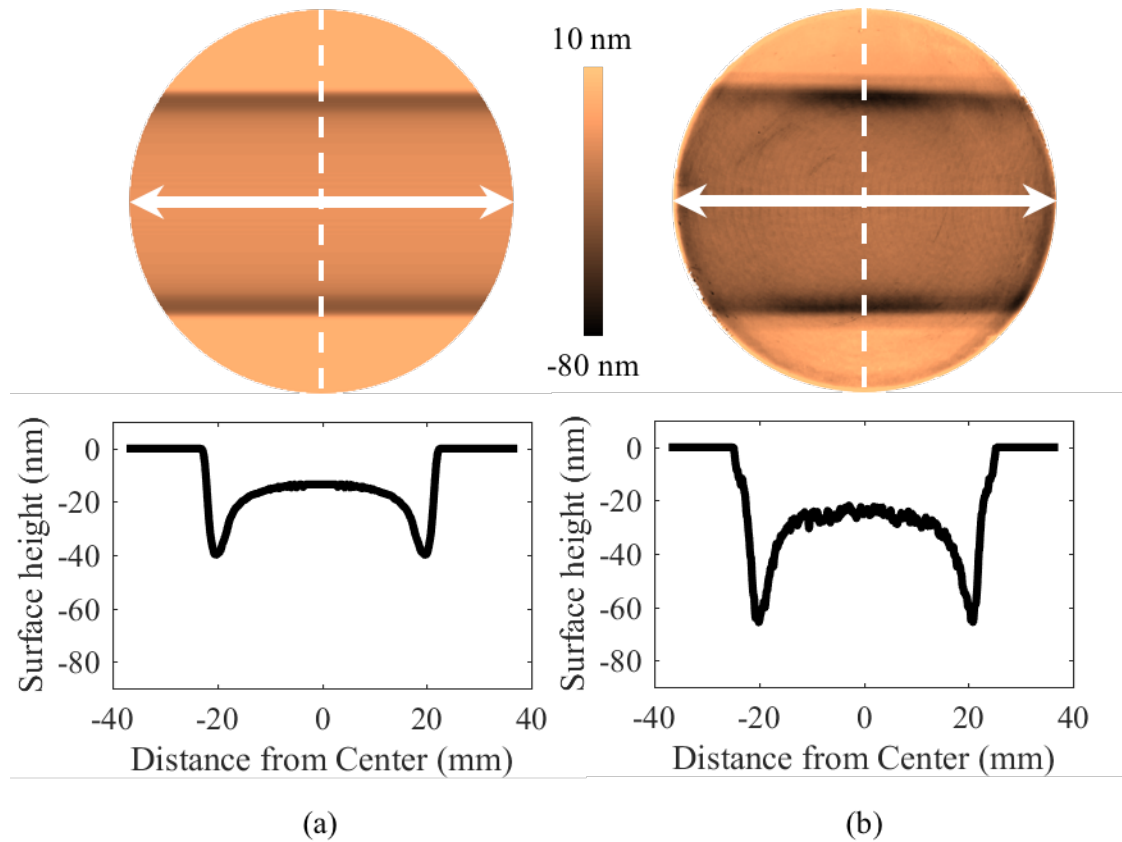


Figure 5-8 MR data of the twelve fiber Nylon 6/6 tool during translation and linear extracted profiles (dashed line) from the MR data; (a) prediction from convolution (b) experimental outcome

The total volume of MR from the test was about 50% more than the prediction. This discrepancy is most likely rooted in the different slurry mixing conditions, as a corollary of the translational motion of the tool. Visual observation of the spot test showed that the abrasive particles exhibited more settling than the scenario where the tool was in translation, in the slurry bath. The addition of tool translation mitigated the particle

settlement. This in turn is believed to cause engagement of larger number of abrasive particles in action, and hence more removal from the surface polished with the tool in translation.

Consistency of the material removal profile shapes, suggested that the increase in the MRR had occurred uniformly. It is speculated that a TIF obtained from a spot test with proper slurry circulation may aid in a better agreement between the convolution and experimental MR profiles.

5.7.2 Evaluation of Tool induced form and MSF errors

The full raster path was used to estimate the form and MSF errors induced by the tool. It should always be taken into consideration that fiber based tools are essentially a sub-aperture tool, and MSF errors are expected to be imparted on parts that are processed with these tools. The test setup for this testing was sketched in Figure 5-7(b).

In order to have an estimate of the imparted MSF of the tool, the Fourier transform can be applied to equation 5-1. The resultant equation will be:

$$MP(\lambda_x, \lambda_y) = \Delta(\lambda_x, \lambda_y)TIF(\lambda_x, \lambda_y) \quad [\mu m] \quad (5-2)$$

Where MP , Δ , and TIF , represent the Fourier transforms of MR , D , and TIF respectively. Equation 5.2 suggests that the material removal spatial frequency content, will be driven by those present terms in the dwell time and the TIF. By that logic, the main sources of expected MSF's are the footprint size and the raster stepover in the testing. For a simple raster path with a given stepover, the stepover length will be a spatial wavelength of interest. The TIF of the Nylon 6/6 tool has an approximate size of 50 mm. Therefore, it will have potential spatial wavelengths of anything below this TIF size.

For experimentally evaluating the extent of the tool induced form and MSF errors, a full raster test with a stepover of 0.5 mm was conducted. The spindle speed was at 100 RPM and the tool feed rate was 3 mm/s. The total polishing time was approximately 200 minutes, and the Hastilite PO[®] slurry was used as the polishing slurry.

The tested $\varnothing 75$ mm BK7 part was measured before and after polishing with the Fizeau interferometer. The same measurement and data processing procedure outlined in section 5.7.1 is used. The subtraction map, i.e. map containing the form error, see Figure 5-9(a), had a total RMS value of 8 nm. The simulation results predicted a total uniform removal depth of 60 nm. However as evident from this result, a degree of non-uniformity, albeit low (RMS 8 nm) existed.

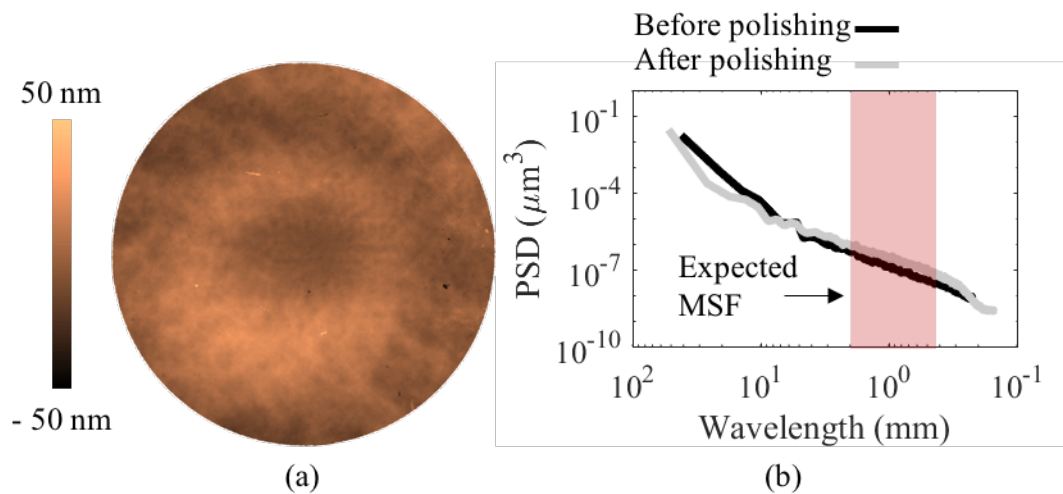


Figure 5-9 Full raster polishing BK7 with the twelve fiber Nylon 6/6 tool; (a) subtraction map containing the imparted form error (b) PSD of the before and after polishing data

The prediction from the MATLAB[®] analysis, was that MSF errors with a wavelength of 0.5 mm and a PV of 2 Å should be imparted by the tool. The MSF errors were characterized by looking at the PSD of the part before and after the polishing.

Discussed in Chapter 2, MSFs are indicated by a noticeable spike in the PSD within the 0.08 mm and 3 mm bandwidth, i.e. in this case 0.5 mm and 2 mm, see Figure 5-9(b). The PSD of the before and after polishing data didn't suggest the inducement of any unexpected MSF errors on the part.

Sources of the form error could be due to uncertainties present in the subtraction map. These uncertainties can arise from the measurement of the part before and after the polishing. Furthermore, more uncertainty can be introduced during the calculation process of the subtraction map. In order to estimate such uncertainties, five separate measurements of a planar BK7 glass on the same Fizeau interferometer were taken. Prior to each measurement the part was cleaned, and Petroleum Jelly was applied to the back surface. Each measurement setup was given an additional 45 minutes for reaching temperature equilibrium with the room. The measurement data were then subtracted from one another, resulting in 10 subtraction residual maps. The total RMS of each subtraction map was calculated, and the 10 RMS values had an average of 5 nm. Comparing this value with the 8 nm RMS evaluated as the imparted form error, the conclusion is that the form error should be much less than 8 nm RMS. This error over the course of 200 minutes of polishing and 60 nm of uniform removal is not significant.

Nevertheless, speculations regarding the other possible sources of form error are presented. Initially the total form error was decomposed into the rotationally varying (RV) and rotationally invariant (RI) parts, using the Zernike base polynomials, Figure 5-10. The RV part had a total RMS of 5.6 nm, whereas the RI term contribution was 4.1 nm RMS. The decompositions were up to the first twenty-eight Zernike terms. More information on the Zernike polynomials can be found in Appendix B.

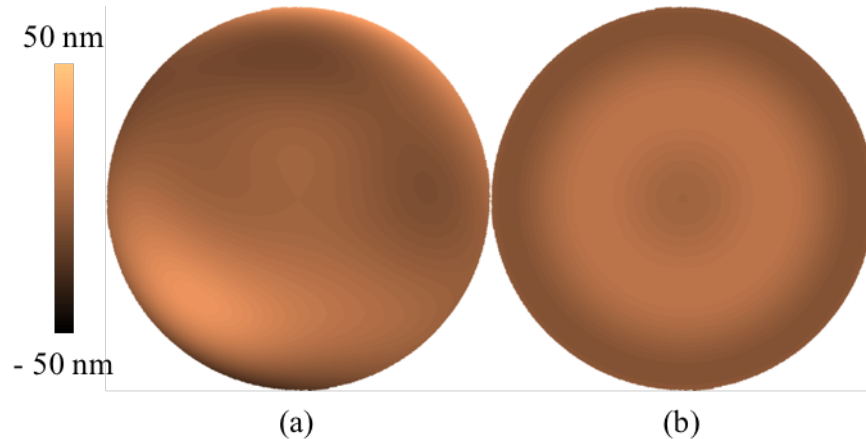


Figure 5-10 Zernike decomposition of the tool induced form error (a) RV part (b) RI part.

The RV term (Figure 5-10(a)) as its shape suggested can be attributed mainly to the unevenness of the part fixture, part rocking in the fixture, and part bending. The machined pocket into the polycarbonate sheet had a non-smooth surface. Initial measurement of the parts in this setup with the dial indicator, showed typically a tilt of about 0.03° , which translates into a 0.038 mm height difference from edge to edge of the part. Both of the aforementioned factors can contribute to the unevenness of the fixture and as a result the errors induced during the polishing.

The RI terms (Figure 5-10(b)) were conjectured to be related to thermal instabilities of the testing setup. After all no temperature controlling apparatus was used for this experiment.

5.8 Material Removal in the Inline Slurry Delivery Configuration

5.8.1 Spot tests on planar samples

The external slurry delivery in the OptiPro[®] Triumph system causes the slurry dynamics to be very different than of that in the submerged bath. Initial tests were focused

on evaluating the twelve fiber Nylon 6/6 tool's MR capabilities with the different slurry supply mechanism. The slurry used, UltraSol[®] Optiq, is a ceria based slurry provided by Eminess[®] Technologies. This slurry has special formulation for lower settling rates [139] relative to the Hastilite PO[®] slurry, and the particle sizes are 400 nm which are smaller than the 1 micron Hastilite PO[®] slurry particles.

In the first test a spot test was conducted on a $\varnothing 75$ mm BK7 glass sample. The spindle speed was 100 RPM, and the sample was polished for 10 minutes. The spot profile generated by the tool using the inline slurry feed conditions had the same V-shape similar to the spot profile obtained in the slurry bath, however, the MRR with the inline system was significantly higher. The tool's MRR in the inline delivery system was nearly ten times of the tool's MRR in the slurry bath. The very different slurry dynamics and the polishing slurry were the main parameters changed relative to the testing in the slurry bath.

The next test was to examine whether the tool's MRR maintains its relative linear relationship with tool velocity. A spot test with 500 rpm spindle speed and 10 minutes was obtained. The MRR of the tool with 500 rpm spindle speed was increased about 600%. The very deep zones of the removal region, hindered the measurement of the part by the interferometer, and thus a mechanical profilometer, OptiTrace 5000, was used for the measurement of the polished sample. Concluding statement is missing

5.8.2 Spot tests on non-planar sample

The testing on the spherical BK7 sample with a spindle speed of 100 rpm and for 10 minutes, was carried out. The FEM pressure profile and the resulting MR spot on the non-planar surface are compared next to each other in Figure 5-11(a), (b) respectively. The FEM, detailed in Chapter 3, predicted a C_{PRESS} length of 1.3 mm and a C_{OPEN} length of

3.9 mm. These values were smaller than the tool process width of 7.1 mm. This under-prediction of the FEM was observed for the planar surface, where the FEM had predicted C_{PRESS} and C_{OPEN} lengths of 3.75 mm and 10.7 mm respectively, whereas the tool had a process width of 13 mm. It is notable, however, that the FEM correctly predicted that the process width of the tool on the concave surface should be smaller than that of the planar surface.

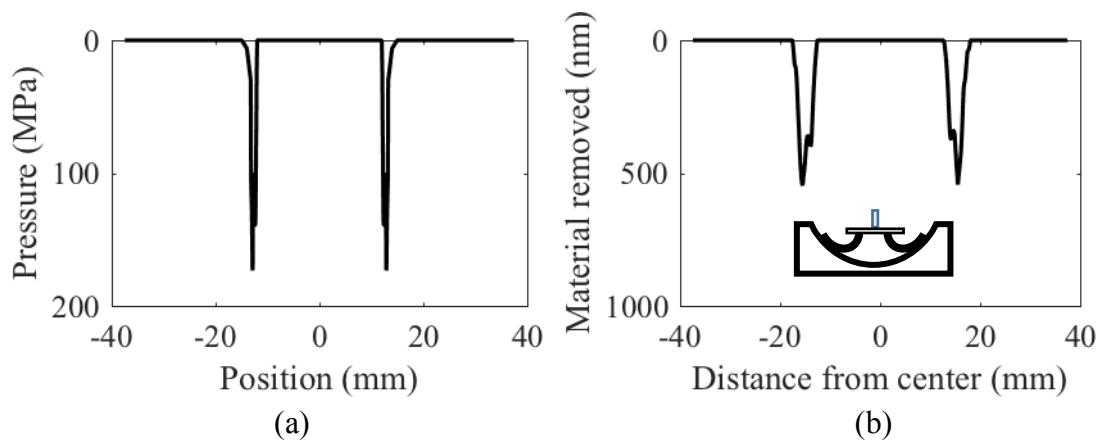


Figure 5-11 The twelve fiber Nylon 6/6 tool on the concave surface (a) FEM pressure profile (b) experimental MR spot profile

The V-shape was present in both the FEM and experimental MR profile. This suggests that the mechanics of MR on a non-planar surface, was similar to that on the planar surface. This spot will be used later for predicting the MRR of the tool with the addition of translation, on the same curved surface.

5.8.3 Evaluation of total MR and MR profile shape of the tool with translation

After verification of the tool's ability in removing material with the new slurry feed, the next test was to ensure that this removal remains consistent with the addition of tool translation. The test setup was introduced in Figure 5-2. As it was displayed in that figure,

no consideration for an extended/sacrificial surface, for negating the edge effects of the part, was accommodated. The tool was only translated to a certain distance, where no fiber damage and/or reengagement issues would arise.

Two different translation tests on planar samples were conducted. In the first test, similar to that conducted on the 3-axis system, the tool was translated back and forth on a linear path. This test was done to investigate whether material is removed with the tool in translation, as well as, to determine how the total volume of MR compares to that predicted by convolution methods as detailed in section 5.7.1.

The tool was translated with a linear rate of 3 mm/s and a spindle speed of 100 RPM. The tool was translated back and forth for 38 passes which amounts to 20 minutes of process time. The same UltraSol[®] Optiq slurry was used.

Figure 5-12(a) shows the surface map predicted by convolution in MATLAB as well as a linear profile extracted from the surface map. Figure 5-12(b) depicts the subtraction map obtained from subtracting the sample interferogram before and after the polishing, and a linear profile extracted from the subtraction map. Evidently the MR profile shapes, were very similar. The volume of removed material of the experimental outcome was about 4% higher than that predicted by convolution, which considering the measurement uncertainties, the differences were negligible. It should be noted that the discrepancy in the MR volumes in the external slurry delivery configuration was much smaller than that in the slurry bath (50%). This corroborates the notion that having similar slurry mixing conditions in both the spot test and the translation test, does indeed aid in better prediction of the convolution procedure.

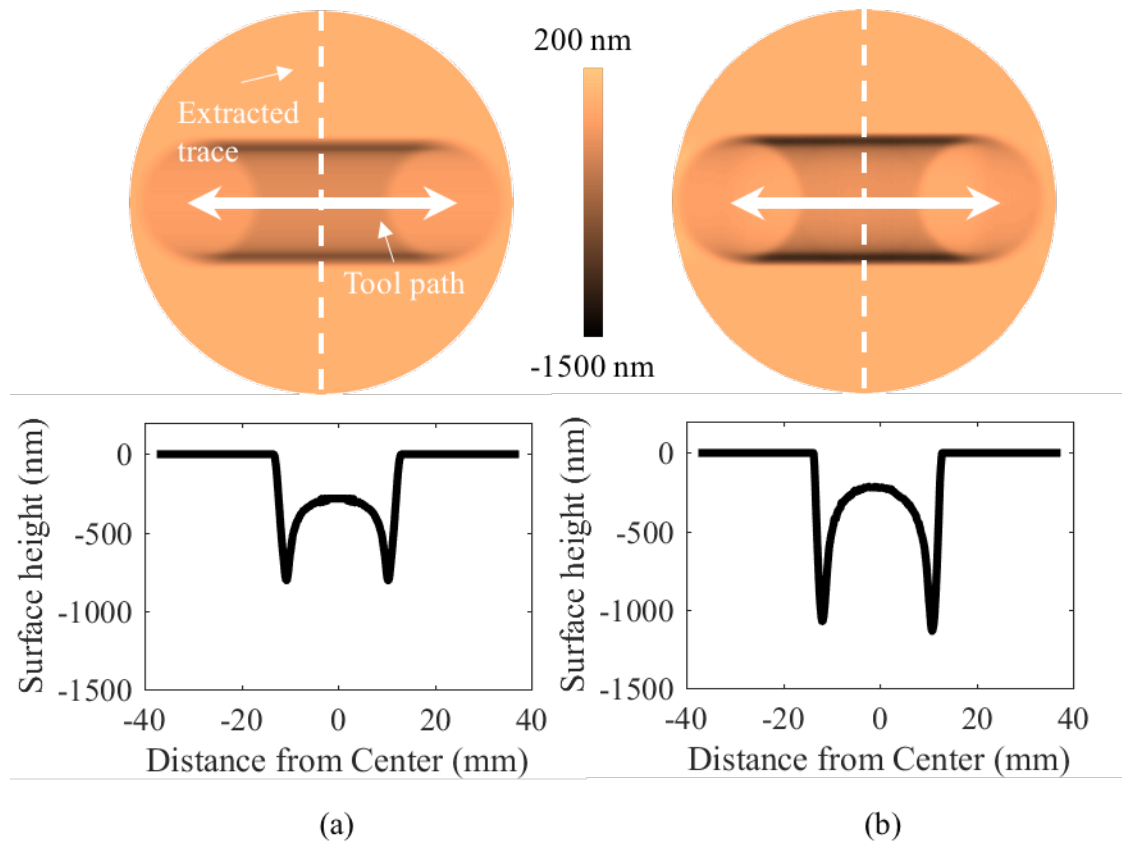


Figure 5-12 MR data and linear extracted profile of the Nylon 6/6 tool during translation on BK7 glass; (a) prediction from convolution (b) experimental outcome

5.8.4 Evaluation of MR volumes during spiral polishing on planar sample

The tool's stable footprint in the simple reciprocal test gave the motivation to further conduct a test with a spiral raster polishing path. Figure 5-13(a) shows the testing configuration of this spiral raster polishing tool path. As shown in the figure, Spindle 1, i.e. the spindle where the tool was attached to the machine, provided a linear motion as well as the rotation of the tool around its axis. Spindle 2, where the workpiece was fixed, only rotated around its central axis. The combination of the rotation on Spindle 2, and a linear motion on Spindle 1, produced a spiral tool path. The spiral stepover was the distance that

the tool traverses per one revolution of Spindle 2. The spiral stepover can be easily calculated by division of the linear feed (in mm/min) by the Spindle 2 RPM.

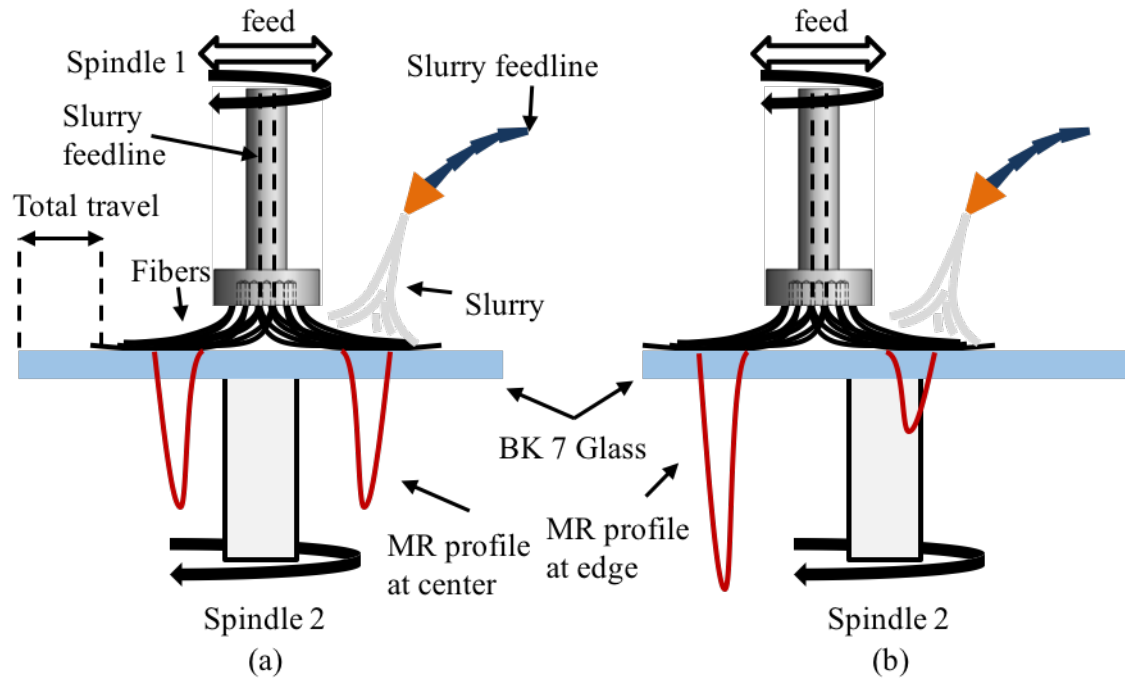


Figure 5-13 Spiral raster polishing configuration and MR profile change with tool position (a) tool at center (b) tool at the edge

As a consequence of this polishing configuration the absolute velocity of the fibers changed as the tool moved towards the edge, and hence change in the MR profile depth is expected. Figure 5-13(a), (b) shows two cases where the tool was located at the center and near the edge respectively. In order to include this change in the MR profile in the convolution calculation, the absolute velocity of a fiber can be stated as follows:

$$V_{fiber} = V_{workpiece} + V_{fiber/workpiece} \quad [mm/s] \quad (5-3)$$

where $V_{workpiece}$ is the product of the radial position of the fiber with respect to the workpiece center, times the rotational velocity of the workpiece, i.e. Spindle 2 RPM.

$V_{fiber/workpiece}$ is the velocity of the fiber relative to the workpiece, i.e. the tool's rotational

speed, i.e. Spindle 1 RPM, multiplied by the radial position of the fiber with respect to the tool center. The fiber velocity, V_{fiber} , is then derived from equation 5-3. Figure 5-14 illustrates a snapshot of the tool in operation and the graphical representation of the described relations. The last note that should be pointed out, is the variability of the tool dwell time at different radial positions of the workpiece. Clearly as the tool is traversed towards the edge the increase in the velocity of the tool center, translates into smaller dwell times, and thus lower volume of removed material.

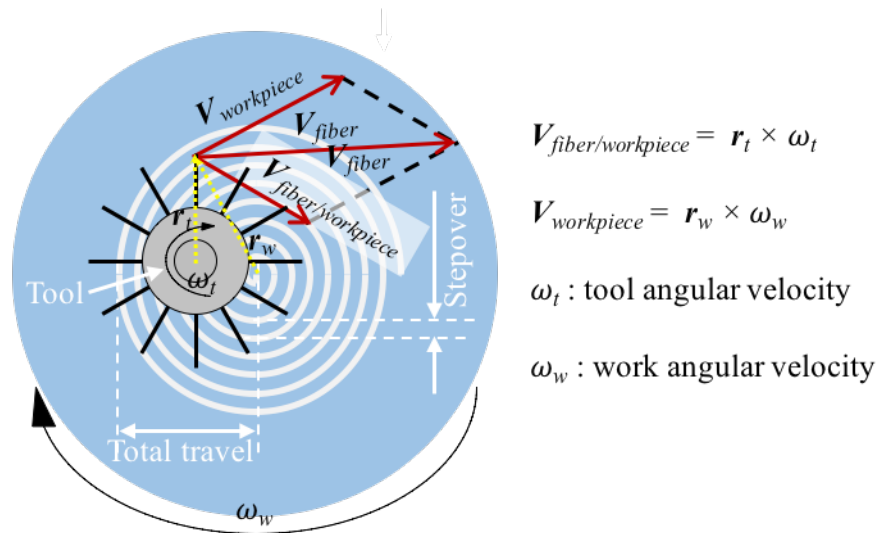


Figure 5-14 Top view of the spiral polishing configuration and the tool kinematics

For the testing, a piece of $\varnothing 75$ mm planar BK7 glass was used. the Spindle 1 was kept at 100 RPM. The spiral stepover was 0.5 mm with a linear feed of 3 mm/s. The work spindle (Spindle 2), was ran at 356 RPM. The total travel, i.e. the distance which the tool travels from the center of the part to the workpiece edge is 11.5 mm.

The predicted surface map by convolution and the subtraction MR map, i.e. after polishing interferogram minus before polishing interferogram, are depicted in Figure 5-15 (a) and (b) respectively. While the profiles of the linear traces extracted from the surface

maps resembled each other, the total MR from the convolution was 7% less than of that from the experimental data.

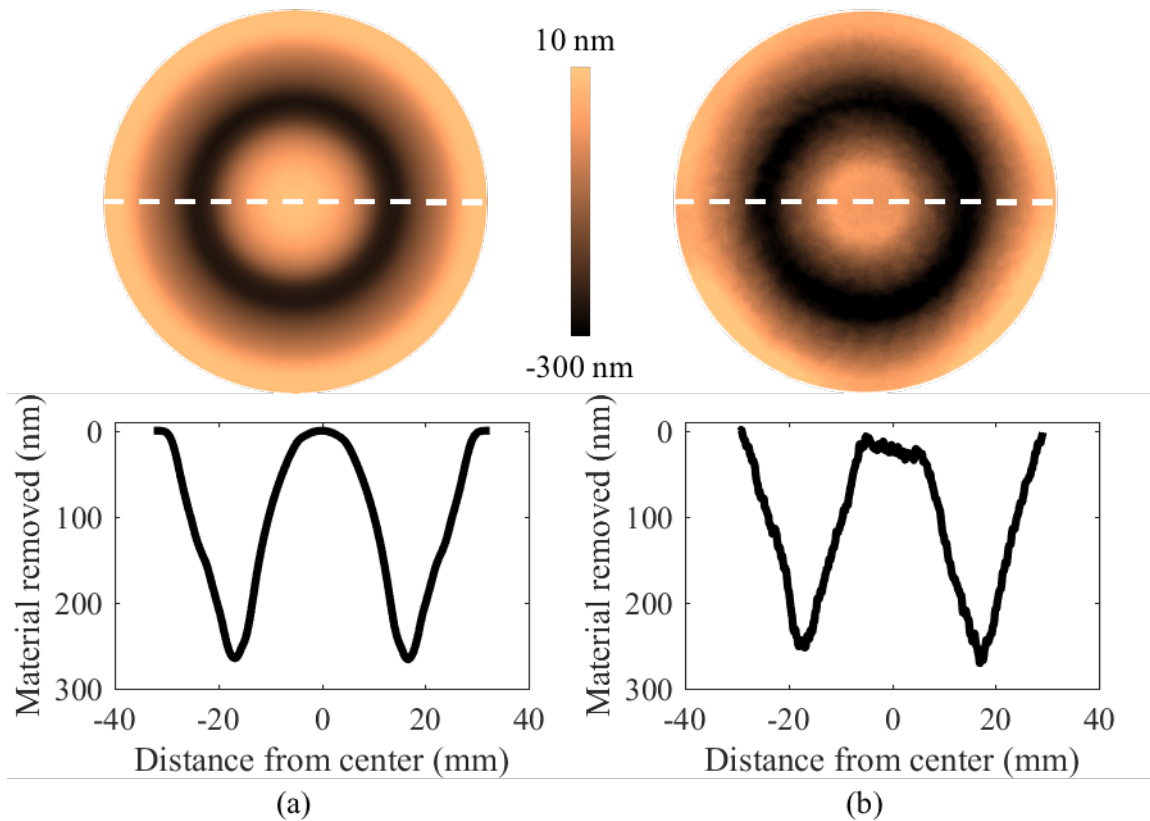


Figure 5-15 Spiral polishing of planar BK7 glass interferogram and extracted profiles; (a) predicted by convolution, (b) measured experimental outcome

The difference in the MR volumes between the testing and convolution can be attributed to the uncertainty in the measurement of the surface undergone the spiral polishing process, as well as uncertainty in the measurement of the spot of the tool used for obtaining the map through convolution. Numerical uncertainty due the subtraction process for obtaining the MR data can also be another element. In the convolution process, one can consider higher and higher resolution for the dwell points in the dwell time matrix.

Last but not least, it should be stated that this is a single test, and no further testing ensuring the repeatability of the results was done.

5.8.5 Evaluation of MR volumes during spiral polishing on non-planar sample

Next is a translation test on the concave part described in section 5.3. The polishing path is a spiral raster path. Similar to the test conducted on the planar surface, the raster stepover and Spindle 1 speed were set to 0.5 mm and 100 RPM respectively. The linear feedrate was 3 mm/s, and the Spindle 2 speed was 356 RPM. The dwell time and changes to the TIF of the tool are applied similar to that outlined in section 5.8.4.

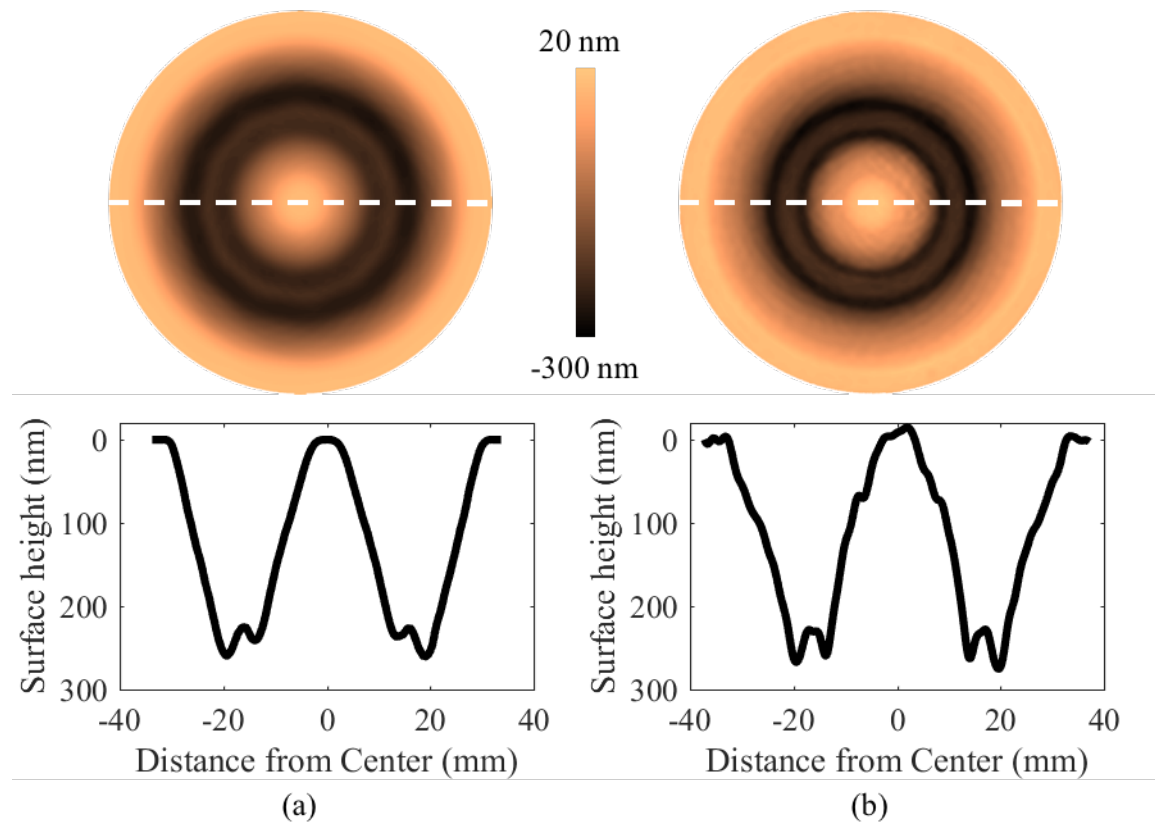


Figure 5-16 Spiral polishing of concave BK7 glass interferogram and extracted profiles;

(a) from convolution (b) experimental outcome

Figure 5-16(a), (b) depict the surface maps of the BK7 glass predicted from convolution and obtained during the testing respectively. The predicted and experimentally measured material removal profiles, looked reasonably similar. The volume of removed material was 3% less in the prediction from convolution. The result was promising, verifying the relatively stable tool footprint on a spherical surface. It should be also noted that the part had a relatively small ROC (≈ 75 mm). The same argument that a spot with similar slurry dynamics to that of the translation test, greatly helped in a better prediction surface map by convolution.

Last of note, the tool had been tested on a convex part as well. The test was only a demonstration of the ability of MR on such parts. Since no spot data was taken prior to the spiral polishing test, results with respect to convolution and predicting the polishing outcomes on such surface, are not presented here. Nevertheless, for full quantification of the performance of the tools on a convex surface, further testing should be carried out.

5.9 Measured Surface Finishes and a Predictive Model

The effect of tool translation on the final surface finish was investigated. It was discussed in Chapter 4 that the surface roughness RMS values are expected to be lower when tool translation is incorporated during the polishing.

The same BK7 glass sample that was used to evaluate the total MR of the tool translating back and forth in the slurry bath (see section 5.7.1), was measured with the 20 \times SWLI. The Zygo ZeGage SWLI, is equipped with an automated stage. This automated stage enables stitching multiple measurements and measuring a larger area than the FOV of the objective. The surface finish of this part was measured and a surface RMS of 0.94

$\text{nm} \pm 0.08 \text{ nm}$ over 200 different polished sites was calculated. The stitched interferogram of the 200 measurements showed a distinct tool signature, see Figure 5-17.

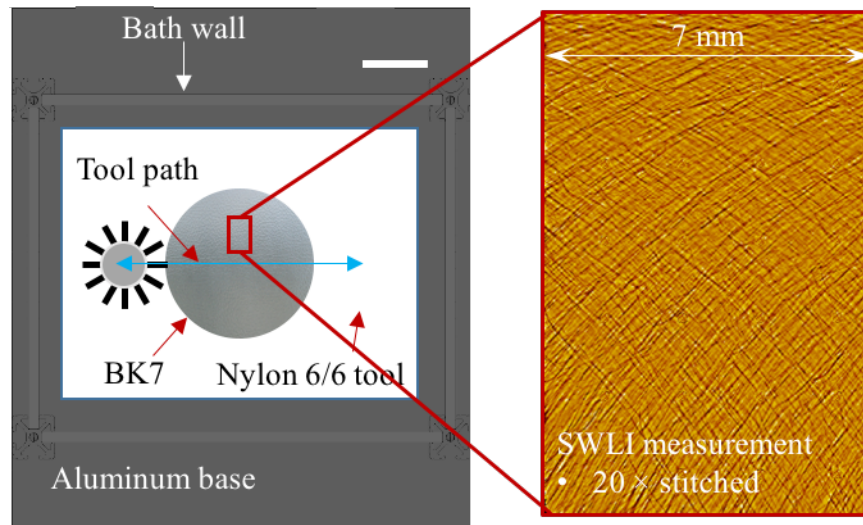


Figure 5-17 Stitched SWLI measurement of BK7 glass during reciprocal path polishing

Indeed, it is speculated that this signature is correlated to the position of a particle that is carried by the leading edge of the fiber. Considering this notion, one can assume that the position of a single particle, engaged with the fiber and the workpiece can be approximated at all times. Figure 5-18(a) shows an instantaneous snapshot of the tool engaged with a planar workpiece.

The abrasive particles are entrapped at the leading edge of the fiber in the removal zone. It is assumed that particles are next to each other without any gap between them, see Figure 5-18(b). Using the TIF of the tool (described in section 5.7), i.e. the V-shaped profile, each particle will have a distinct depth of cut per second, depending on its position in the removal zone. Evaluation of the locus of all the particles entrapped, for a given period of time will enable the calculation of the total removed material per point on the surface.

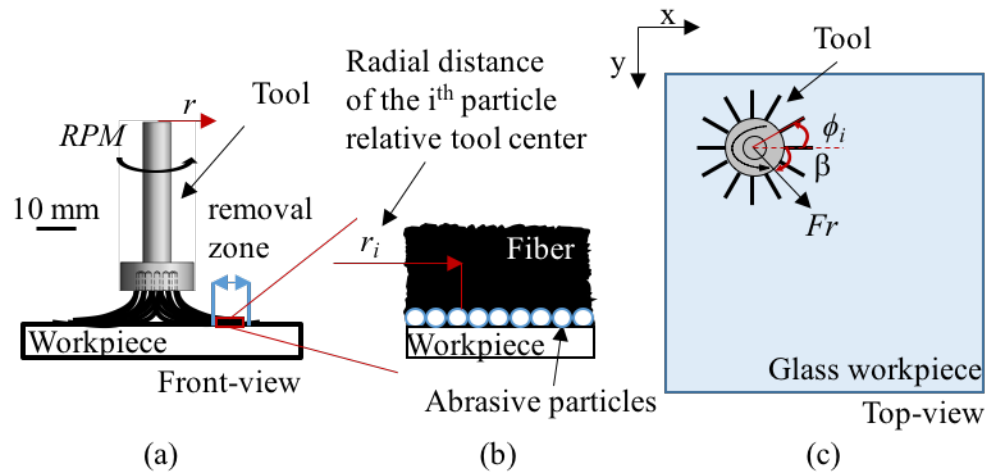


Figure 5-18 Fiber-abrasive-workpiece interaction snapshot; (a) front view of tool engaged with workpiece (b) close-up view of fiber particle engagement (c) top-view coordinates of the tool

The surface topography calculated from the outcome thereof will provide a first order estimation of the surface finish of BK7 glass polished with the Nylon 6/6 tool. It is admitted that this model is very simplistic and doesn't completely encompass the random nature of the polishing action. Nevertheless, it will be seen that it is yet capable of giving close estimates of the finish and texture of the polished surface.

An arbitrary set of tool kinematics are considered in Figure 5-18. The tool is spun with a spindle speed of RPM and a feedrate Fr in mm/s. Thus, for a particle that is entrapped by a fiber, at initial ($t = 0$ s) angle of ϕ_i and its radially distanced as much as r_i relative to the center at of the tool at x_0, y_0 , the coordinates of the particle at other given time t can be described as follows:

$$\begin{aligned}
x_t &= \int_0^t [r_i \omega \cos(\omega\tau + \phi_i) + V_x] d\tau + x_0 + r_i \cos(\phi_i) \quad [mm] \\
y_t &= \int_0^t [r_i \omega \sin(\omega\tau + \phi_i) + V_y] d\tau + y_0 + r_i \sin(\phi_i) \quad [mm]
\end{aligned} \tag{5-4}$$

where ω is the angular velocity of the tool obtained from the spindle speed. The components V_x and V_y , i.e. horizontal and vertical velocity components are:

$$\begin{aligned}
V_x &= Fr \cos(\beta) \quad [mm/s] \\
V_y &= Fr \sin(\beta) \quad [mm/s]
\end{aligned} \tag{5-5}$$

and β is the instantaneous angle of the tool path relative to the horizon, see Figure 5-18(c).

With the set of equations derived in 5-4, the position of any given particle can be found at any given time t . While the validity of this model was only verified for a planar surface, it can be easily modified for spherical surfaces (surfaces with constant ROC). For surfaces with non-uniform ROC's, however, some special considerations should be taken into account such as accounting for the change in the MR profile of the tool as a consequence of the varying ROC. The resolution to which this model can be implemented depends on the computer memory used. Figure 5-19(a) contains the same measured surface texture data of the BK7 glass depicted in Figure 5-17. Figure 5-19(b) contains a simulation result using a very coarse time vector resolution ($\Delta t = 1$ s). While numerically the result didn't provide insights, it was encouraging that the fiber traces evident in the measurement interferogram, were too, manifested in the simulated surface.

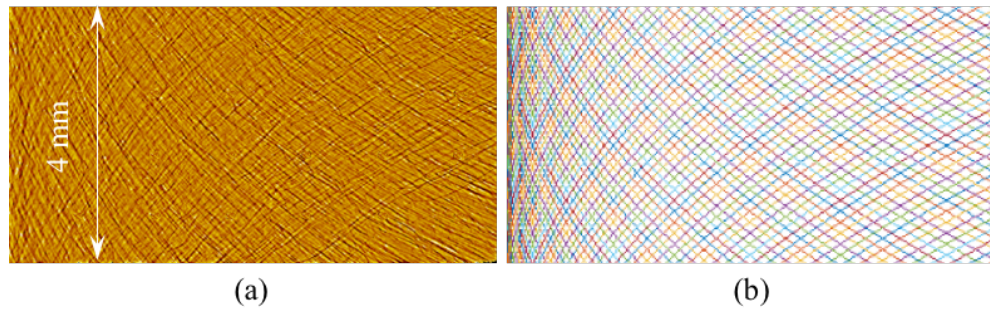


Figure 5-19 (a) actual surface measurement (b) fiber trace simulation

To numerically test this model, an FOV of the 20× objective was simulated on a 1024×1024 matrix. That will make the simulated map to have a spatial resolution of $0.4072 \mu\text{m}$. The minimum resolution for the time vector was obtained by calculating the maximum velocity of the fiber in the zone of simulation. With the assumption of an equal vertical and horizontal spacing, i.e. $\Delta x = \Delta y$, the expression for the minimum time resolution was the following:

$$\Delta t = \frac{\Delta x \sqrt{2}}{Fr + r_s \omega} \quad [s] \quad (5-6)$$

r_s , is the maximum radius of the fiber sweeping the zone of simulation. Using MATLAB parallel computing capabilities, the simulation process took around 60 hours.

For the case of a $Fr = 3 \text{ mm/s}$, $r_s = 14 \text{ mm}$, and $\omega = 10.5 \text{ rad/s}$. The zone of study is shown in Figure 5-20(a). The RMS value of the actual surface measurement was 0.9 nm . The RMS predicted from the simulation was 0.76 nm . The height maps of both the experimentally measured and numerically simulated surface are shown in Figure 5-20(b) and (c) respectively. Both maps show the existence of the fiber traces on their surfaces. This simulation result adds further support to the MR mechanism theory of the tools.

The main reasons for the discrepancy between the simulation result and the experimental outcome was conjectured to be not taking any consideration of the random motion of the abrasive particles during the polishing.

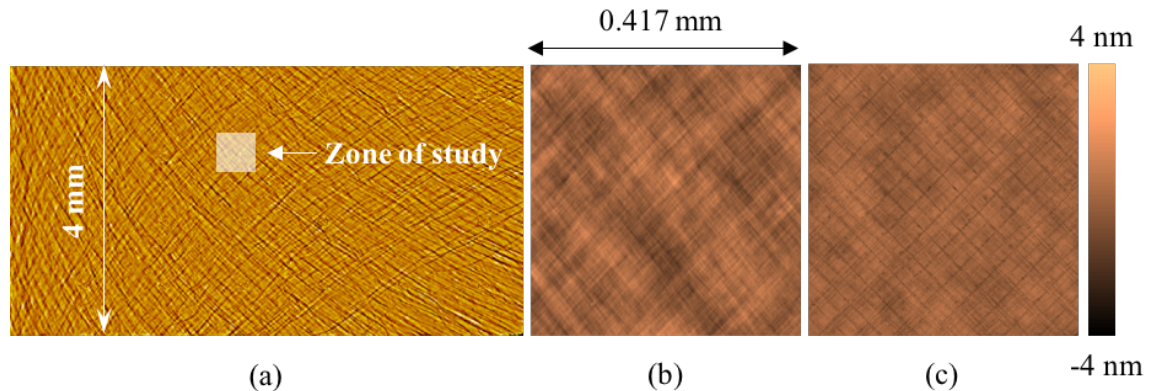


Figure 5-20 (a) Interferogram of BK7 sample polished with Nylon 6/6 tool (b) 20× SWLI measurement of the zone of study (c) simulated surface of the zone of study

5.10 Summary

In this chapter, initial attempts towards the integration of fiber based tools in a more practical setting was taken. Two different CNC machines and two different slurry delivery systems were investigated. The key takeaways of this chapter can be briefed as follows:

- It was shown that the addition of translation, did not impede the material removal capability of the Nylon 6/6 tool.
- It was also shown that the Nylon 6/6 tool, unlike conventional polishing tools, suffered from smaller edge roll off zones, whilst operating near the edge. Yet, the tool was limited by the fibers ability in reengaging with the workpiece. The fiber struggled to reengage with the workpiece when the fiber on the tool was beyond

the edge of the workpiece. The roll off lengths were predicted by the simple FEM, adding more value to the modeling efforts.

- The stability of the polishing footprint, over long polishing (times > 30 minutes) was investigated. It was seen that the total volume of MR and MR profiles closely matched to that predicted by convolution in the inline feed configuration. In the slurry bath configuration, although the MR profiles of the experimental polishing and that predicted by convolution resembled each other, the volume of MR during translation was 50% more than that predicted by convolution. The reason for the discrepancy between the MR volumes of the experimental polishing and prediction by convolution is thought to be mainly as a result of the different slurry mixing conditions during the spot test and the translation test in the bath.
- The stability of the polishing footprint, over long polishing times was investigated. It was shown that form and MSF errors imparted by these tools were very consistent with the prediction from convolution. These were both shown in a full raster polishing path and a spiral polishing path.
- A simple model to predict the surface finish of BK7 glass polished with the Nylon 6/6 tool was developed. The model predicted the surface finish RMS with an approximately 20% error to that obtained experimentally.

CHAPTER 6: MSF ERROR REDUCTION WITH FIBER BASED TOOLS

6.1 Introduction

This chapter is dedicated to a key aspect of this work, i.e. reduction of MSF features. The main topics in this chapter are as follows; (1) key principles behind the MSF reduction capability of fiber based tools are discussed, (2) an additional FEM for identifying fibers with the potential to reduce MSF features is created, (3) experimental MSF reduction polishing tests are done, and results are presented, and (4) an alternative fiber design with higher MSF reduction capabilities is introduced.

6.2 MSF Reduction of Fiber Based Tools Theory

For maximizing the opportunity of reducing MSF features with fiber based tools, two key principles were used. First and foremost, fibers that offer minimal local deflection to the MSF features were desirable. Figure 6-1(a) illustrates a fiber based tool engaged with a freeform workpiece. Figure 6-1(b) shows a close up of the fiber interacting with MSF's with large fiber deflection to the MSF features (undesired). Figure 6-1(c), however, demonstrates a scenario where the fibers have very small deflections to the MSF features (desired). The case in Figure 6-1(c) is considered favorable to promote preferential material removal from the peaks of the MSF's and not their valleys.

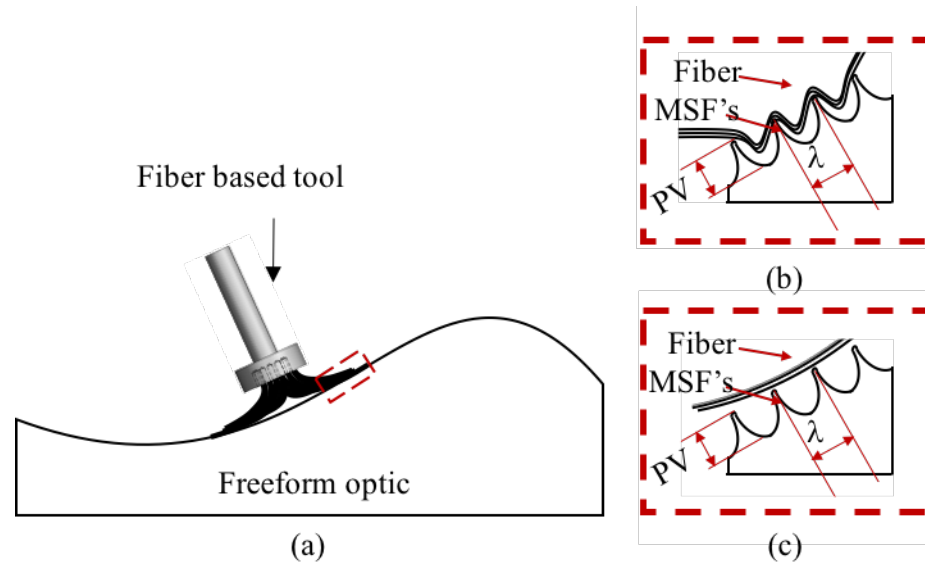


Figure 6-1 (a) Fiber based tool interaction with a freeform containing MSF features (b) close-up of scenario of a fiber with significant local deflection (undesired) (c) close-up of a scenario of a fiber with negligible deflection (desired)

Secondly, the use of a polishing slurry containing small abrasive particles to minimize processing of the lower regions of the MSF features. Particles smaller than the magnitude of the MSF feature are considered less likely to engage with both the fiber and the valley of the MSF feature and thus will not be as effective in removing material in the lower regions.

6.3 Fiber-MSF FE Modeling

To evaluate the amount of deflection of a fiber to MSF features, a two-step FE model was used. Step 1 of this model was similar to the model described in Chapter 3, on the fiber workpiece interaction, that was used to obtain the fiber pressure distribution on the workpiece. In step 2, a section of the fiber was taken, and placed on two MSF peaks. These peaks were defined as boundary conditions where the fiber had zero displacement.

The other boundary condition was the loading on the fiber when in contact with the MSF peaks. To approximate the exerted load on this portion of the fiber, due to the bending moment, the contact pressure distribution in step 1 of the model is used, see Figure 6-2(Step 1). A best fit triangular distribution was fitted to the contact pressure profile obtained in step 1. The approximated pressure profile was then used in the model in step 2, see Figure 6-2 (Step 2). The output of step 2 is the extent of fiber deflection between the MSF peaks as a result of the applied load.

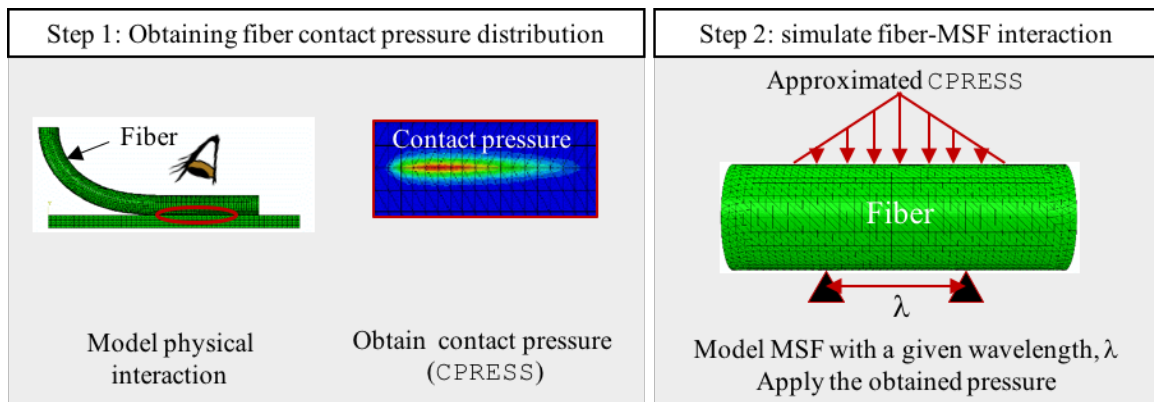


Figure 6-2 Fiber-MSF FEM; Step 1 and Step 2

This modelling approach was used to investigate the impact of three different fiber parameters on the amount of maximum fiber deflection between MSF's. The key fiber properties that were suspected to influence this deflection were the modulus of elasticity of the fiber material, the second moment of the cross section, and the geometry of the fiber's cross section. A range of the expected values of the aforementioned properties along with four cross-sectional geometries were selected. Table 6-1 contains the range of the properties that were opted for this group of models. A total number of twenty models were created using the parameters available in Table 6-1. An additional model was also created to investigate the impact of the wavelength of the MSF features on total fiber deflection.

Table 6-1 Fiber properties used for the two-step fiber-MSF FEM

Variable Property	Range of the variable property	Constant properties values
E (Young's modulus)	1 GPa \rightarrow 6 GPa	($I = 0.32 \text{ mm}^4$, Geometry: ●)
Geometry	● ■ ▲ ▬	($E = 2.3 \text{ GPa}$, $I = 0.32 \text{ mm}^4$)
I (second moment)	0.04 mm^4 , 0.32 mm^4 , 1.6 mm^4	($E = 2.3 \text{ GPa}$, Geometry: ●)

For all of the models used in this section, no plastic material behavior was included. All the elements used, were of the type C3D10M. The approximate element size in all models were 100 μm . The simulations for step 1 of the FEM were performed for fiber lengths of 25 mm and workpiece dimensions of 25 mm \times 4 mm \times 1 mm. The fiber section length in step 2, for the twenty models in Table 6-1, was 3 mm and the MSF spacing was at 2 mm. In the final model for studying the impact of the MSF spacing on fiber deflection, the fiber section length in step 2 was 2 mm and the MSF spacing was 1 mm. The results obtained from the models revealed four key findings. These results are discussed briefly in the sections that follow.

6.3.1 Fiber Young's modulus

The first parameter studied, was the Young's modulus associated with the fiber material. The modelling was done for the circular fiber with a diameter of 1.6 mm, see Table 6-1. The moduli values ranged from 1 GPa to 6 GPa with an increment of 0.5 GPa. The results showed that fiber deflection didn't change significantly with change in modulus of elasticity (<1%), nor did they follow a specific trend with change in the modulus values, see Figure 6-3. Based on the results detailed in chapter 4 and 5, the tools comply with Preston's law of MR, therefore a higher modulus induces higher polishing loads and

consequently MR. The higher modulus property can be leveraged for higher MRR's for a specific fiber geometry.

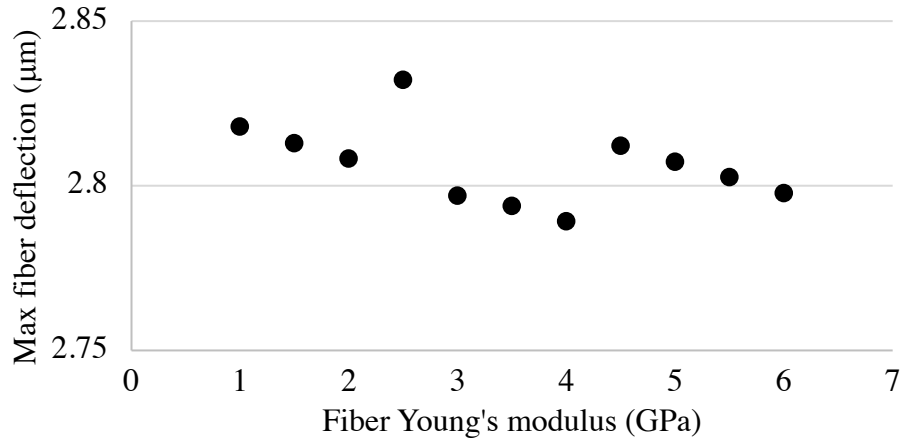


Figure 6-3 Ø1.6 mm fiber deflection to MSF's vs fiber Young's modulus

6.3.2 Fiber cross section geometry

The four fiber cross section geometries shown in Table 6-1, underwent the same modeling procedure. For each fiber, the Young's modulus and second moment of the cross section were kept at a constant value of 2.3 GPa and 0.32 mm^4 respectively. The modeling outcomes showed that geometry had a very significant effect on the fiber deflection, see Figure 6-4. As seen in the figure, deflection values vary about 2 μm across the different geometries. No obvious relationship between deflection and geometry was established; this highlights the need for modeling to reduce the large design space of these tools. Even then finding an optimal geometry, should one desire to minimize this deflection, is no trivial task.

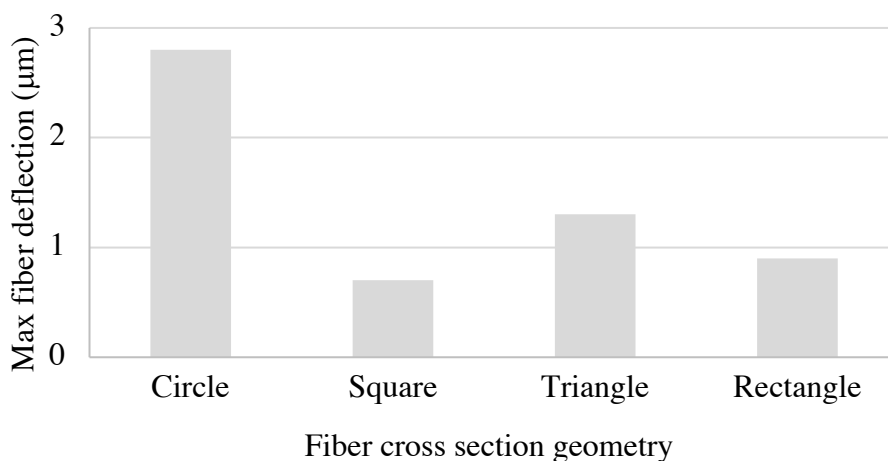


Figure 6-4 Fiber deflection to MSF's vs fiber cross section geometry

Different geometries, not surprisingly, exert very different pressure distributions on the workpiece in the contact zone. Figure 6-5 shows the contact pressure distributions of the fibers with different cross section geometries on a planar surface. These differences in pressure distributions can be leveraged in designing tools with different TIF's.

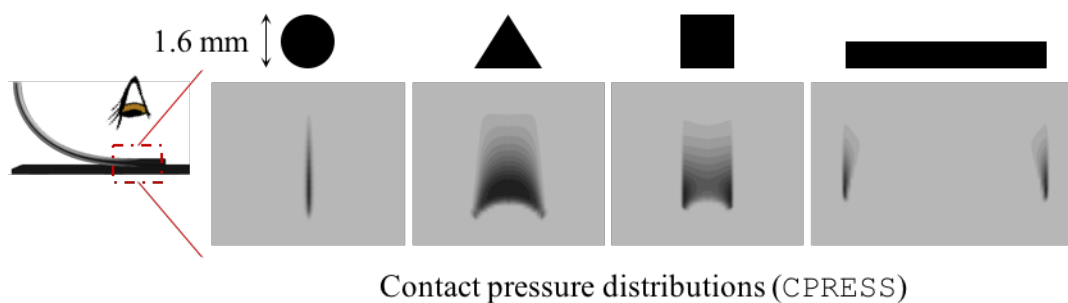


Figure 6-5 FE contact pressure distribution (CPRESS) for different fiber geometries

6.3.3 Fiber second moment of the cross section

The last fiber property investigated, was the second moment of the cross section of the fiber. While this is a function of geometry itself, the circular fiber was used for

modeling three different fibers with different second moment of the cross sections. The second moment of the circle geometry is calculated with the following relation:

$$I = \frac{1}{4}\pi r^4 \quad [mm^4] \quad (6-1)$$

where r is the radius of the circle.

As stated in Table 6-1 three different cases with second moment of 0.04 mm^4 , 0.32 mm^4 , and 1.6 mm^4 , were modeled. These values corresponded to fibers with diameters of 1 mm, 1.6 mm, and 2.4 mm. Figure 6-6 shows how the change in the second moment significantly changed the total fiber deflection to the MSF features. This was a very important result, on the grounds that could help in isolating optimal fiber dimensions associated with a specific geometry. From Figure 6-6, for the circular geometry, decrease in the second moment leads to decrease in the fiber deflection.

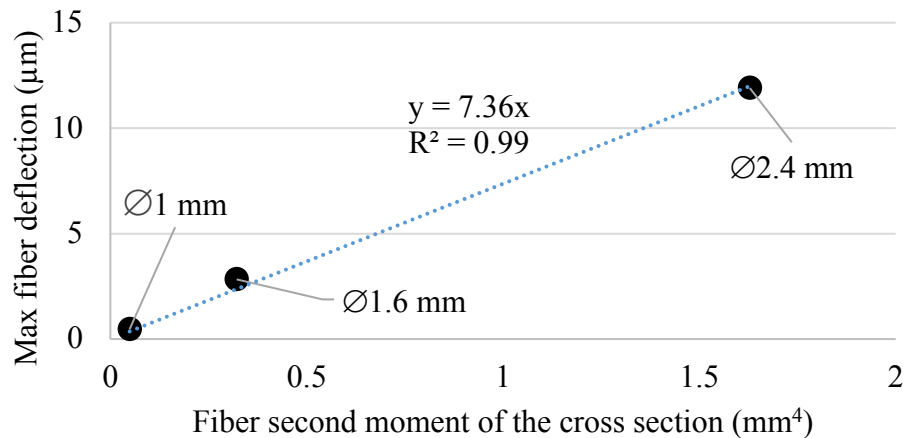


Figure 6-6 Max fiber deflection VS second moment of the cross section

In summary of this section, the key fiber properties that influence the fiber deflection across two MSF features, was mainly related to the fiber's geometry. The material of the fiber, didn't change the maximum deflection significantly. The simplicity

of this model is admitted, yet the knowledge gained from the results can be of great help in directing future tool/fiber design.

6.3.4 MSF feature wavelength

To study the impact of the wavelength of the MSF features on the maximum fiber deflection, the same model parameters in Step 1, i.e. fiber length of 25 mm, was used. In step 2 a model using an MSF wavelength of 1mm was created. The fiber had a diameter of 1.6 mm, and a fiber length of 25 mm. The fiber had a Young's modulus of 2.3 GPa, and the second moment of the cross section of the fiber was 0.32 mm. The fiber properties correspond to the Nylon 6/6 fiber. The fiber deflection value using the same two-step modeling scheme, with the 1 mm MSF wavelength, was approximately 80 nm. The deflection value for the same fiber on an MSF feature with 2 mm wavelength was approximately 2800 nm. As expected, the fiber had much smaller deflections to MSF features with a smaller wavelength.

6.4 Experimental Setups and Testing Samples

To verify the FE modeling results, experimental testing was carried out. As explained in section 6.3.4, for the Nylon 6/6 fiber, the model predicted a fiber deflection of approximately 80 nm to MSF features with $\lambda = 1$ mm. This number was deemed promising enough for testing the fiber on a sample containing MSF features with $\lambda = 1$ mm. For the same fiber, the expected magnitude of deflection when the MSF features were separated by 2 mm was evaluated as 2800 nm. This implies that the Nylon 6/6 fiber would struggle reducing MSF features with a wavelength larger than 2 mm. However, the potential of reducing MSF features of 1 mm wavelength, was sufficiently encouraging to

experimentally investigate. The experiments were done on samples with premade MSF features with a specific wavelength and amplitude (PV). Both of the experimental setups detailed in Chapter 5, i.e. slurry bath configuration on the 3-axis machine (Haas-TM1), and external delivery slurry configuration on the 5-axis system (OptiPro Triumph), were used.

Two different material samples were used. The first sample was a piece of $\varnothing 65$ mm germanium with a thickness of 12 mm. The workpiece had premade MSF features with an approximate wavelength of 1 mm and PV of 200 nm. The features were diamond turned on the surface with a Nanotech 350 FG, a 5-axis ultra-precision machine. MSF features with two different geometries were fabricated; concentric sinusoidal features, and concentric cusp shapes. For the polishing tests done in the slurry bath, the germanium sample was recessed into a planar polycarbonate sheet so that its surface was flush with the polycarbonate sheet. This was done to avoid any edge effects.

The second sample was a $\varnothing 75$ mm BK7 glass sample containing sinusoidal MSF features with an amplitude of 200 nm and wavelength of 2 mm. This sample was machined on a QED Q-22 XE MRF machine. This sample was tested in the inline slurry delivery system, i.e. OptiPro Triumph machine, and thus no sacrificial surface was included.

Two polishing slurries were used. For polishing germanium, the UltraSol[®] 556 manufactured by Eminess[®] Technologies was used. The slurry was a colloidal suspension containing silica particles as abrasives. The particles had an average size of 65 nm, which compared to the particle sizes used in the Hastilite PO[®] slurry (500 nm to 1000 nm), used in testing presented in Chapters 4 and 5, were much smaller. The reason behind opting for this slurry was that the smaller particles, intuitively, will have a lower chance of engaging with the lower regions of the MSF features, see section 6.2. The UltraSol[®] 556 slurry was

mixed with 3 Wt% of H_2O_2 , whereby the chemical reaction between the germanium surface and the hydrogen peroxide promotes material removal [140]. For polishing glass, the UltraSol[®] Optiq slurry was used. Details of this slurry can be found in Chapter 5.

Two polishing tools were used. Both tool configurations had the FT-1 design, see Chapter 4 for details of the tool designs. The first tool, had twelve Nylon 6/6 fibers ($\varnothing 1.6$ mm) with the length of 25 mm. The second tool had fifty-six PET fibers ($\varnothing 0.22$ mm) with the same 25 mm length. The reason for testing this tool was due to the smaller second moment of the PET fiber, and the possibility to enhance the local stiffness of the fibers to the MSF errors, see Figure 6-6. The simple two-step FEM predicted fiber deflections as small as 20 nm to MSF's with, $\lambda = 1$ mm. Even though, the material properties were not fully known, the model outcomes had shown that this should be of secondary importance, as far as the fiber stiffness to the MSF errors were concerned.

6.5 Metrology

The metrology tools used are similar to what was described in Chapter 4 and 5. Additionally, a mechanical profilometer, Talysurf 120-L was used. The mechanical probe had a diamond tip with diameter of 2.5 μm . A best fit plane was removed from all the measurements of the instruments, and a band-pass filter with cutoffs of 0.08 mm and 8 mm was applied. This instrument had a total lateral range of 100 mm and a vertical range of 6 mm. The lateral resolution of the instrument is limited by the diameter of the diamond tip. The reason for using this instrument was the existence of very steep zones on the MR profiles on the workpiece, after the polishing. The large slopes prevented the interferometric measurement of the samples.

6.6 MSF Reduction Spot Tests

6.6.1 Twelve fiber Nylon 6/6 tool MSF reduction (fiber diameter = 1.6 mm)

The initial tests, similar to the test detailed in Chapter 4, were done with the tool position fixed, i.e. spot test. In the first test, the testing conditions were at spindle speed of 100 RPM and load of approximately 7 N, using the twelve fiber Nylon 6/6 tool. The polishing slurry, as it was mentioned earlier, was the UltraSol[®] 556. The tool was run for 60 minutes on the germanium sample. Due to the significant amount of MR, the large induced slopes on the sample, voided the possibility of measuring the part with the interferometer. The Form Talysurf 120-L profilometer was used to measure 4 traces on the part.

In Figure 6-7 the results with respect to one of these traces, is depicted. The tool induced a V-shaped MR profile as expected. After removing the V-shaped from the measurement data, the profiles of the before and after polishing measurements are depicted in Figure 6-7(a) and (b) respectively. While it may appear that material has been added to the profile in some areas, this is only an artifact produced by the filtering process of the V-shape MR profile. That said, clearly the PV of the MSF features is reduced in the polishing zone. The PSD of the two profiles, before and after the polishing test showed a visible reduction in the peak of the PSD at the 1 mm wavelength, see Figure 6-7(c).

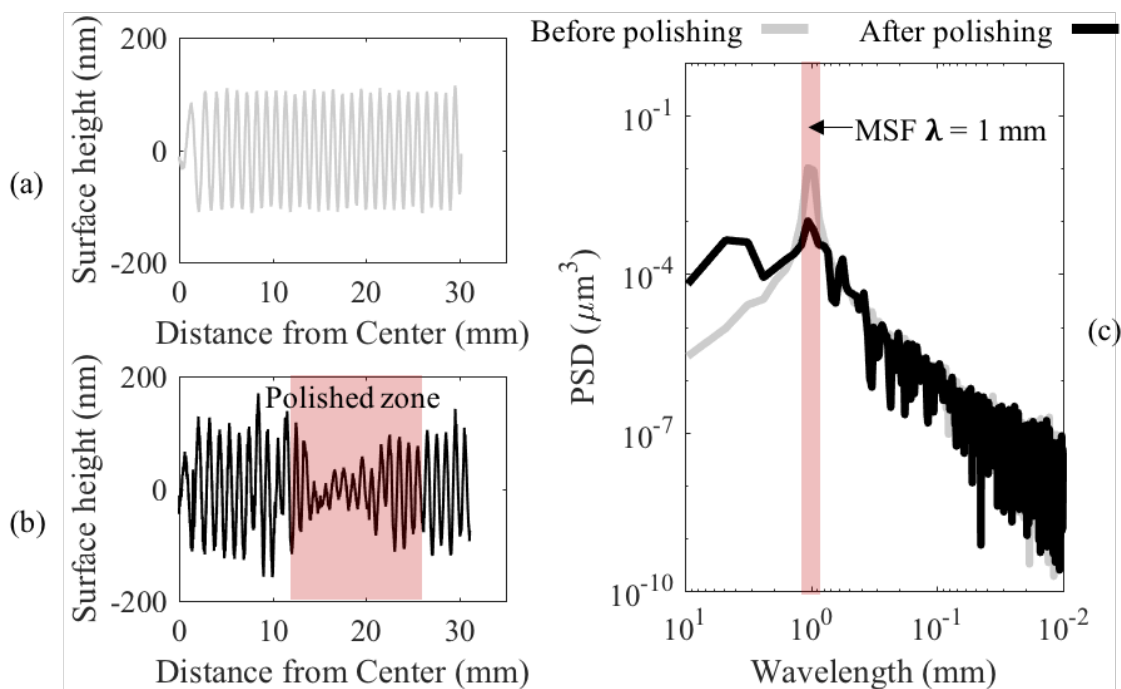


Figure 6-7 MSF reduction testing with the Nylon 6/6 tool with no tool translation; (a) before polishing surface profile (b) after polishing surface profile (c) PSD of the before and after polishing profiles

These results, verified the potential of the Nylon 6/6 tool in reducing MSF features with spatial periods of 1 mm. A quick scrutiny of the surface profiles of the part showed an approximate 130 nm reduction to the PV of the MSF features. A redo of this test with a shorter polishing time had verified the outcome. The combination of small fiber deflection and small abrasive particles, seemed to culminate into preferential material removal from the peaks of the MSF features, causing the PV to decrease over the course of the polishing operation.

6.6.2 Fifty-six fiber PET tool MSF reduction (fiber diameter = 0.22 mm)

The next test was done with the fifty-six fiber PET tool. The considerably slenderer fibers (\varnothing 0.22 mm), with an approximate Young's modulus of 3 GPa, implies much smaller

loads exerted by the PET tool. This in turn would result in lower MRR's. Therefore, the polishing time was kept at the longer 60-minute time interval, and the spindle speed remained at 100 RPM.

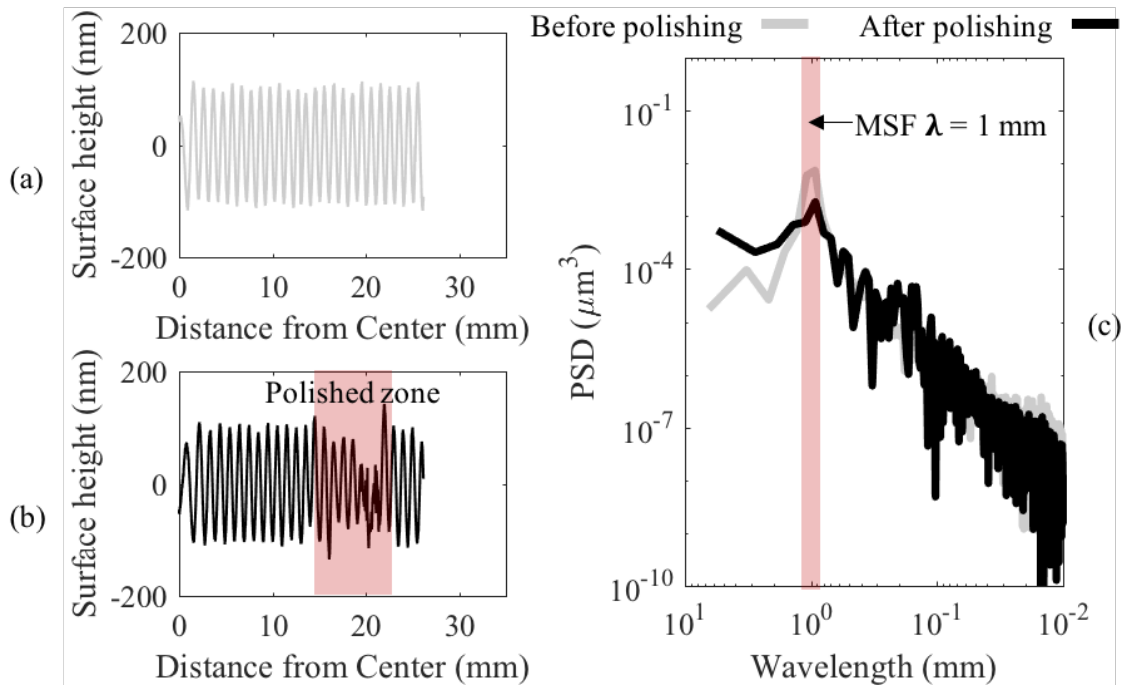


Figure 6-8 MSF reduction testing with the PET tool with no tool translation; (a) before polishing surface profile (b) after polishing surface profile (c) PSD of the before and after polishing profiles

The part was measured with the Talysurf profilometer. Figure 6-8 (a), (b) shows the before and after polishing surface profiles respectively. Both the reduction in the PV of the MSF features, as well as drop in the 1 mm spike of the after polishing PSD (see Figure 6-8 (c)) shows that the PET tool had successfully reduced the premade MSF features with the wavelength of 1 mm. This result, adds credibility to the two-step FEM.

6.7 MSF Reduction Tests Under Translational Conditions

Success in reducing the premade MSF features on germanium during the spot tests, gave the motivation to examine the tool's capability in reducing MSF's under translational conditions.

The PET tool, had very low MRR's in the spot test. This means that measurable MSF reduction with the PET tool, would require very long polishing times. Thus, the remaining polishing results presented will be exclusive to the Nylon 6/6 fiber.

6.7.1 MSF reduction from germanium with premade sinusoidal MSF features

In the first test the germanium sample had premade sinusoidal MSF features. The tool was translated over the workpiece back and forth in a straight line, similar to that described in sections 5.7.1 and 5.8.3. See Figure 5-7(a) for the testing setup. The spindle speed was 100 rpm and the tool was translated with a linear velocity of 3 mm/s. The tool made 107 passes which amounts to 200 minutes of polishing.

The sample was measured before and after the polishing on traces parallel and perpendicular to the polishing path, using the Talysurf profilometer. The results of such testing are depicted in Figure 6-9. As evident in Figure 6-9 (a), (b) both measurement traces showed reduction in the PV of the sinusoidal features. Figure 6-9(c), (d) contain the PSD of the measurement traces. Both PSD's showed the reduction of the peak of the PSD at 1 mm wavelength.

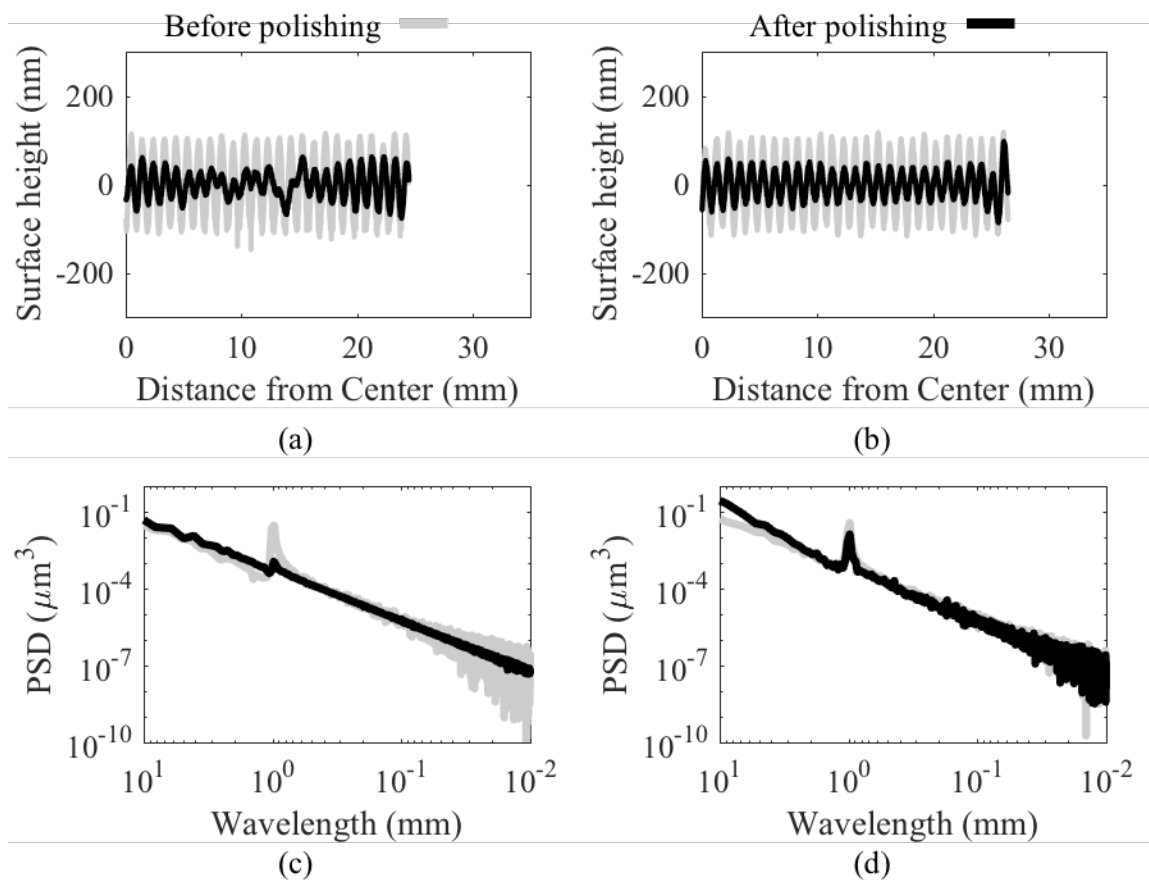


Figure 6-9 MSF reduction testing on germanium; measured profiles (a) perpendicular and (b) parallel to the polishing tool path. PSD of the measured profiles (c) perpendicular and (d) parallel to the polishing tool path

The reduction of the MSF features depicted in Figure 6-9, on the trace perpendicular to the tool path was larger. This can be explained through the fact that material was removed in larger quantities (predicted by the convolution model), and thus causing higher MSF reductions on that path. The higher MSF reduction on the trace where the part exhibited larger MR values, suggests that material is being removed from both the peaks and the valleys. However, the removal from the peaks is preferential. Microscopic

observations of the sample peaks and valleys confirms this conclusion, since the fiber traces were observed in both regions.

6.7.2 MSF reduction from germanium with premade cusp features

In the next test, on the same germanium sample, MSF features with cusp shape geometries were machined on the surface. As cusps are a typical tool signature of the diamond machining process. It was considered worthwhile to investigate the interaction of the Nylon 6/6 tool with such MSF features. The MSF wavelength was kept at 1 mm and the PV values were about 170 nm. For a more expected uniform removal, near the center of the sample, two perpendicular tool paths were chosen, and the tool was reciprocated along each path for 107 passes.

The more uniform material removal enabled the measurement of the part on the Fizeau interferometer. See Figure 6-10(a), (b) for the before and after polishing Fizeau interferograms of the sample. In Figure 6-11(a) depicts the linear profiles extracted from the Fizeau interferograms across the white dashed lines. It can be seen that the PV of the cusps had reduced approximately to an average of 70 nm. This reduction was further validated by the radially averaged PSD of the surface, see Figure 6-11(b). The linear profiles showed the existence of uneven zones of surface height. This was not a great concern, as the polishing tool path is not optimal and such irregularities were expected.

The results shown in this section, provide further proof that the Nylon 6/6 tool is able to reduce MSF's in the presence of tool translation. The next logical step was to verify this reduction capability in a full raster polishing test, which is the subject of the next section.

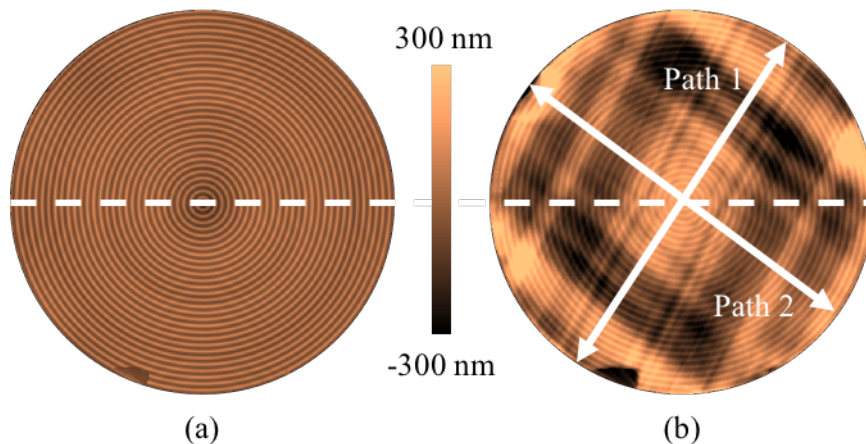


Figure 6-10 Fizeau interferogram of MSF sample with cusps; (a) pre polishing (b) post polishing

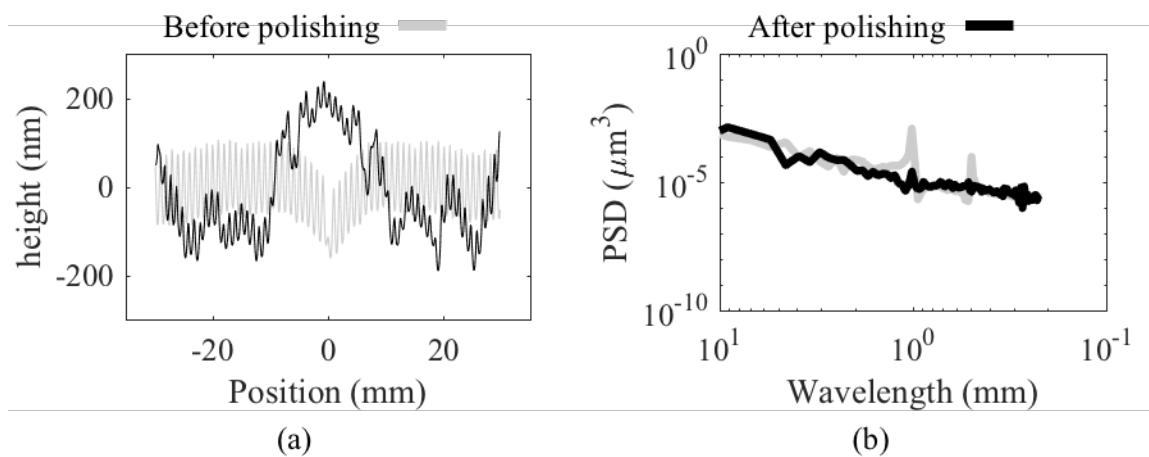


Figure 6-11 (a) Linear slice data off from the Fizeau interferograms (b) radially averaged PSD of the Fizeau interferograms

6.8 MSF Reduction During Full Raster Polishing

The germanium sample was remachined to impart sinusoidal MSF features on its surface (1 mm wavelength, and PV value of 180 nm). The test setup explained in detail in the previous chapter was used to polish the sample in a full raster polishing operation. See

Figure 5-7(b) for this test setup. Three tests were conducted on this sample. The testing conditions for the three tests are given in Table 6-2 below.

Table 6-2 Full raster MSF reduction testing with the twelve fiber Nylon 6/6 tool

Test Number	Spindle RPM	Stepover (mm)	Feed (mm/s)	Time (min)
1	100	0.5	3	200
2	100	0.5	3	200
3	340	0.5	1.5	400

Test 1 and test 2 had the same conditions. The goal of these two tests was to examine the evolution of the MSF reduction over the course of two different polishing operations under nominally identical conditions. In test 3, the spindle speed was increased to the maximum permissible of the testing setup, and the tool linear feedrate was decreased to half of that of test 1 and test 2. This, increased the dwell time of the tool on the part uniformly, resulting in a longer polishing test. The conditions of the testing were opted as such to increase the total MR of the tool, thereby study how these extreme parameters can increase the MSF reduction of the tool. The results of all three tests are illustrated in Figure 6-12. The sample was measured interferometrically before and after each test, using the Fizeau interferometer. The left-hand side of the figure shows the linear profiles extracted from the Fizeau interferograms before and after each test. The right hand side of the figure depicts the radially averaged PSD of the same interferograms before and after each test.

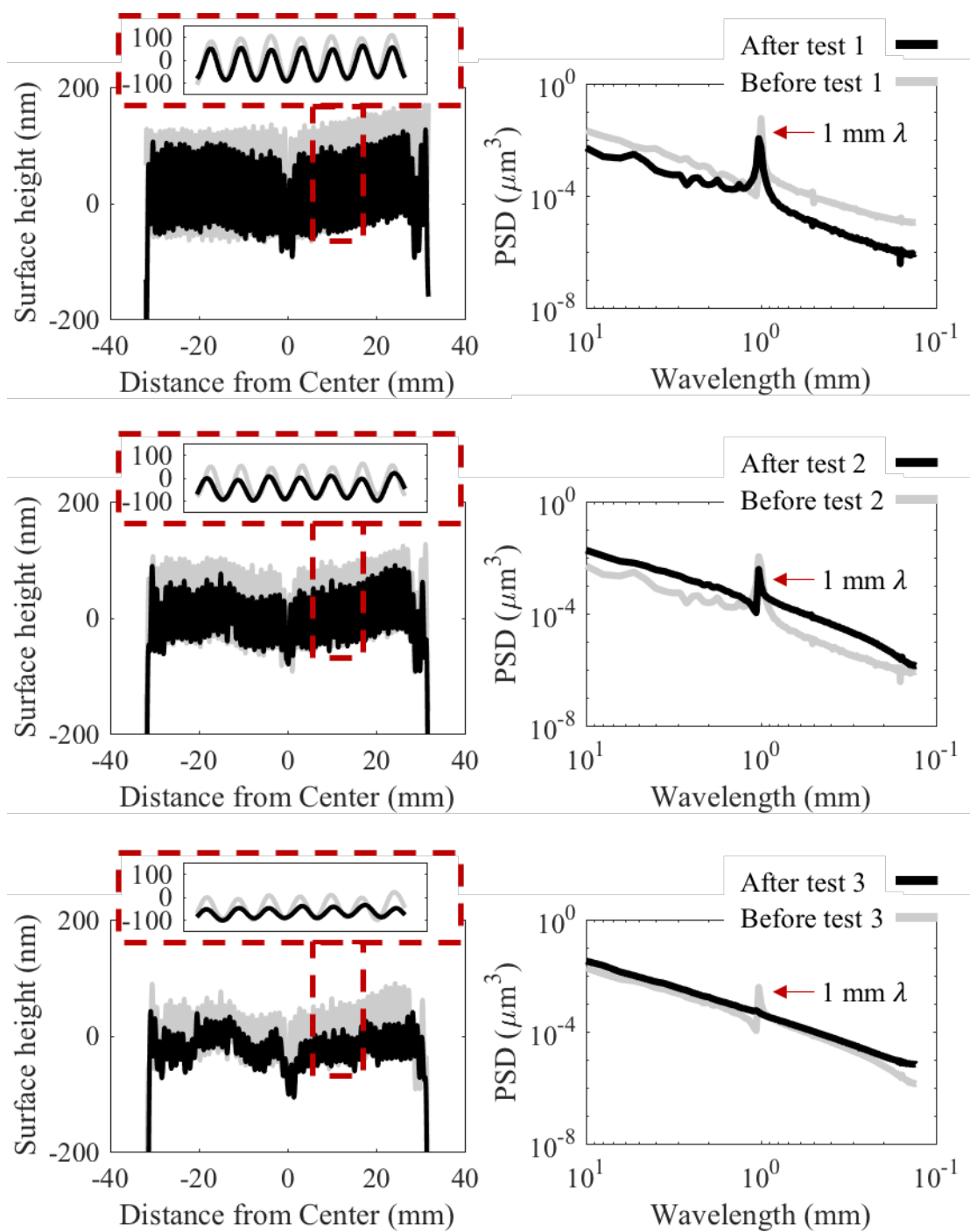


Figure 6-12 MSF reduction from germanium during full raster polishing (left) linear 1-D profiles from the from Fizeau measurements (right) radially averaged PSD of the Fizeau measurements

The results clearly show that the PV of the premade MSF features was reduced after each test. The average PV of the MSF features decreased about 60 nm in test 1. In test 2 this reduction was about 40 nm, and finally in test 3 the PV reduction was around 60 nm. The numbers indicated a non-linear reduction in the MSF's. This was expected as the decrease in PV of the sinusoidal features, implies larger contact lengths of the fiber on the peak of these features, reducing the polishing pressures. This result is in agreement with work published by Parks and Evans [111] where the reduction rate of MSF features from aluminum and electroless nickel dropped non-linearly. The reduction of the MSF features in each test was validated by the radially averaged PSD of the Fizeau measurements of the workpiece after each test. The drop in the peak of the PSD peak in the 1 mm wavelength is evident after each test, see Figure 6-12 on the right hand side.

It should be noted that relatively large form errors ($PV_{\text{form}} > 1 \mu\text{m}$) was induced on the sample, after test 3. While this issue is of importance in fabrication of optics, the test set up was not specifically designed to minimize potential sources of form error. The form control of the part can be achieved by better part fixturing as well as imposing temperature control units to the testing setup.

6.9 MSF Reduction Testing on MSF Features with $\lambda = 2 \text{ mm}$

The two-step FEM, detailed at the beginning of this chapter predicted that the Nylon 6/6 fiber should not be an effective means in reducing MSF features with a wavelength of 2 mm. Preliminary spot tests on BK7 glass with premade MSF features with $\lambda = 2 \text{ mm}$, in the slurry bath configuration verified this prediction. Nonetheless, it was suspected that different slurry dynamics on the inline slurry feed system on OptiPro

Triumph machine, as well as higher centrifugal forces using higher spindle RPM's may enhance the opportunity of reduction of such MSF's.

A polishing test using a spiral raster path configuration was undertaken, see. Figure 5-13 for the spiral path details. The BK7 sample containing MSF features with $\lambda = 2$ mm and PV of 200 nm was used. Spindle 1 was rotated with a speed of 500 RPM, and a raster stepover of 0.5 mm. The spindle was translated with 3 mm/s feedrate and the total polishing time was 30 minutes. Spindle 2 was rotated at 356 RPM.

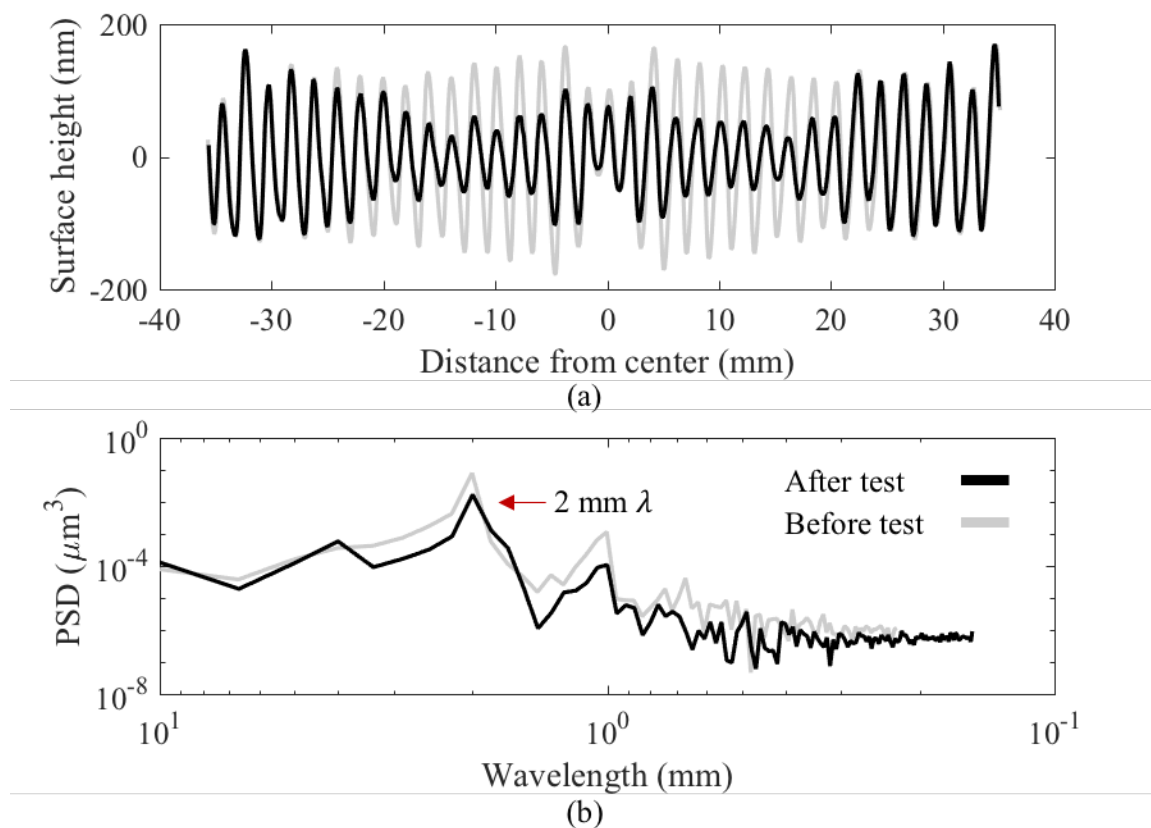


Figure 6-13 MSF reduction from BK7 glass; (a) linear profile from Fizeau measurement
(b) radially averaged PSD of the measurement

The sample was measured before and after the polishing using the Fizeau interferometer. Figure 6-13 shows the outcome of the polishing operation after the removal

of the imparted form error. As can be seen in Figure 6-13(a), the linear extracted slices from the Fizeau interferograms showed a modest reduction in the amplitude of the premade MSF features. This was also reflected in the radially averaged PSD of the measurement data, see Figure 6-13(b). The reduction of the amplitude of the MSF feature is only present in radial zone of about 20 mm. This is due to the limited traverse length of the tool on the workpiece.

In order to compare the efficiency of the MSF reduction of the Nylon 6/6 tool from samples with MSF features with $\lambda = 1$ mm $\lambda = 2$ mm, a metric is defined as follows:

$$\eta = \frac{\Delta PV}{\Delta H} \quad (6-2)$$

Where ΔPV is the reduction in the amplitude of the MSF features and ΔH is the depth of material removal in the reduction zone. The η value for the Nylon 6/6 tool in reducing MSF features from the sample with $\lambda = 1$ mm and the sample with $\lambda = 2$ mm, were 0.1 and 0.045 respectively. The lower MSF reduction efficiency for the sample with MSF features with $\lambda = 2$ mm was not surprising, since both modeling efforts and common sense predicted this.

6.10 Alternative Fiber Design for More Efficient MSF Reduction

In this section, a novel fiber design with the aim of enhancing the fiber based tools MSF reduction capabilities is introduced. The key to more efficient reduction of MSF features centers on the magnitude of the fiber's local stiffness, i.e. resistance to deformation across MSF features. Based on this principle, one approach that seemed feasible and worthy of investigation was a fiber with a non-homogenous structure along its length. Since the deflection of the fiber to the MSF features was driven by the exerted pressure of the

fiber on the workpiece, it can be inferred that for a given fiber stiffness a lower load will cause less deflection. That said, the exerted load by the fiber was determined by the fiber compliance, see Eq. 6.1. Thereby, a fiber with lower compliance at the region of bending than the region of contact would most likely fit this hypothesis the best, see Figure 6-14.

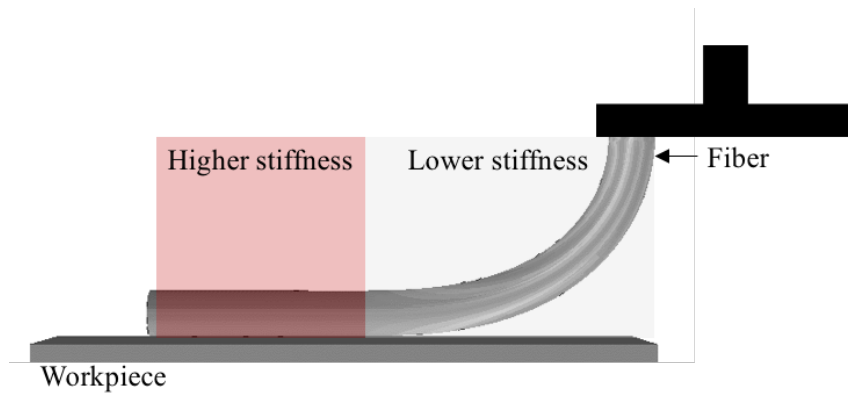


Figure 6-14 Fiber combo concept

Two immediate approaches for the realization of this fiber concept would be the use of a fiber with inhomogeneous material, i.e. varying Young's modulus, and a fiber with a non-uniform cross section. While the fabrication of a fiber with a composite material structure would require specialized fabrication equipment, that is not the case for reducing the cross-sectional area of a uniform fiber, on the side where the fiber is attached to the tool head.

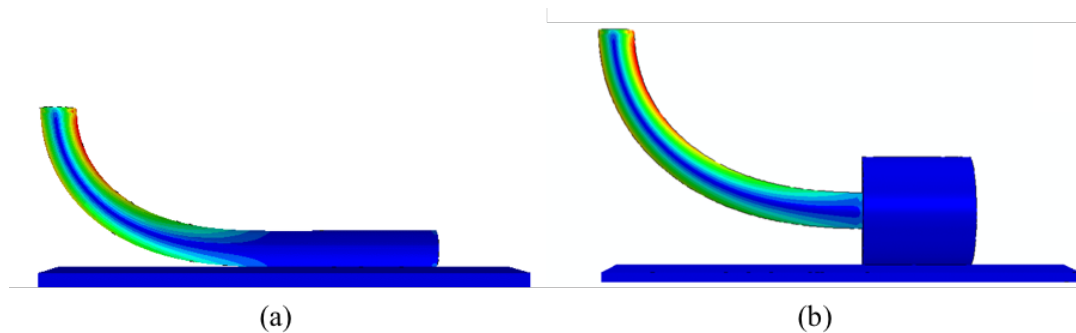


Figure 6-15 (a) Nylon 6/6 fiber (b) modified dumbbell Nylon 6/6 fiber

Figure 6-15(a) shows the FEM of the Nylon 6/6 fiber. In Figure 6-15(b) The Nylon 6/6 fiber FEM with an additional dumbbell section is depicted. The dumbbell diameter in this geometry was 6 mm. This fiber geometry was a sample design of a fiber with a non-uniform cross section that offers a higher stiffness than the fiber with the uniform cross section in the contact zone. The FE pressure profiles for the two fibers shown in Figure 6-15(a), (b), are depicted in Figure 6-16(a), (b) respectively.

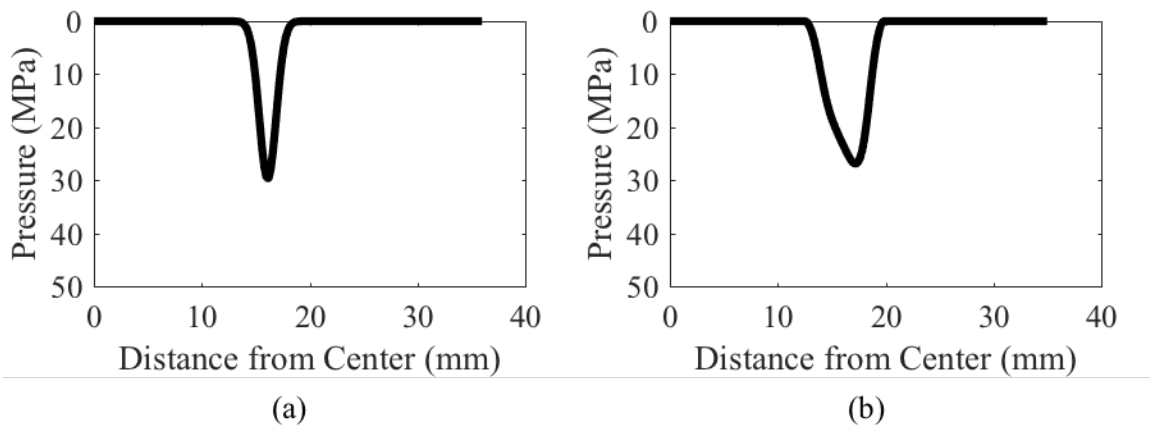


Figure 6-16 FEM pressure profiles (a) Nylon 6/6 fiber (b) Nylon 6/6 fiber with the dumbbell section

As shown in the figure the fibers almost have the same maximum contact pressure on the planar workpiece. This implies that increase in stiffness of the fiber at the dumbbell shaped section doesn't change the total loading significantly, and therefore it was expected that the dumbbell should have smaller deflection values, than the conventional fiber geometry. To evaluate the fiber deflection of the dumbbell fiber the same two-step FEM was used for various dumbbell diameters. In Table 6-3 the decrease in the deformation of the Nylon 6/6 fiber ($\varnothing 1.6$ mm) to a pair of MSF's with a wavelength of 2 mm with the increase in the dumbbell diameter of the fiber is provided.

Table 6-3 Fiber deflection VS dumbbell diameter

Max fiber pressure (MPa)	Dumbbell diameter (mm)	Max fiber deflection (nm)
30	1.6 (same as fiber)	2800
	3	34
	6	14
	12	1

The results in Table 6-3 reveals the great potential for this fiber design. No testing has been done with such fiber, nonetheless, the physics behind the concept strongly support the prediction of far more efficient MSF reduction using this fiber design.

6.11 Summary

In this chapter one of the key aspects of this dissertation was discussed. It was shown that fiber based tools have ability in reducing MSF features. The key results and highlights were the following:

- Fiber based tools can reduce the magnitude of pre-existing MSF features. The promising results demonstrated in this chapter provide proof of concept of the potential of fiber based tools in reducing MSF features.
- A new FEM was created that enabled the identification of fiber characteristics affecting the magnitude of deformation across two MSF features. It was shown that the fiber geometry and second moment of the cross-section had the largest impact on the fiber deformation.

- The MSF reduction capability of fiber based tools was demonstrated both in translation as well as in a spot test. All the test results were a proof of concept of the capability of fiber based tools in reduction of MSF features, and the process parameters weren't optimized.
- An alternative fiber design was introduced. This design showed the potential in enhancing the fiber ability in reduction of MSF's with wavelengths larger than 2 mm.

CHAPTER 7: CONCLUDING REMARKS AND FUTURE DIRECTIONS

In this dissertation, a novel polishing tool was presented that has the potential to reduce preexisting MSF features from freeform optic surfaces. The MSF errors are very common on freeforms and are a result of the sub-aperture finishing processes used to achieve the freeform geometry. Freeform optics currently are the frontier of research in the optics community. The merits of these optics are undeniable, as they expand the design space of optical systems on one hand and enable far more compact systems with comparable performance on the other. The fabrication technologies have not shown a significant breakthrough post the advent of robot polishing systems. Yet the need is necessary on the grounds that the current technologies limit the performance of freeform optics by inducing MSF errors on their final product. The polishing tool developed in this work offers a very different method of MSF feature reduction than of those implemented in industry. The main idea is that the fiber's global compliance to the varying ROC of freeforms, and at the same time local stiffness to the MSF features, can promote MSF reduction. In the foregoing chapters, numerous results are presented that characterize the behavior of these tools in a polishing application and their ability to reduce MSF features. It is admitted that the tool's performance is not optimized, and the results were mainly focused on verifying this core concept. Nevertheless, the tool's potential is sufficiently exciting that it should promote further work in optimization and full integration of such tools in multi axis commercial polishing machines. The key findings of this dissertation,

as well as guidelines on future directions in research and commercialization of such tools are provided.

7.1 Key Findings

7.1.1 Tooling and fibers

- Selection criteria for fibers that would qualify for use in polishing tools were outlined. It was shown that fibers that established a reasonably long contact length (> 5 mm) with the workpiece and were capable of applying sufficient polishing loads (> 3 N), were good candidates to remove material from optical materials.
- The majority of the polishing results were obtained with the simple tool design that resembled a paint brush with a low number of fibers. The simple design enabled the systematic study of the fibers in the polishing application. An alternative tool design was introduced that enabled the tool to achieve smaller tool foot prints. This design was achieved by tweaking the baseline design; reversing the direction of the fiber deflection, i.e. towards the tool axis.

7.1.2 Fiber based tools material removal mechanisms

- Fiber based tools appeared to behave in accordance with Preston's law of material removal; Testing with a selected tool, the Nylon 6/6 tool, showed that an increase in the tool's applied load and rotational speed, resulted in increased tool MRR.
- The fiber tool's material removal mechanism was proposed; The key component of the fiber tool's material removal mechanism is the entrainment of the abrasive particles at the leading edge of the fiber. The fiber holds the abrasives against workpiece surface, and that combined with the rotational motion of the fiber,

moving the abrasives along the surface, induces material removal. The processing width achievable with a fiber corresponds to the length of fiber that can entrain particles at its leading edge, i.e. the length of fiber in contact with the workpiece and the length of fiber whereby the gap between the fiber and workpiece is smaller than the abrasive particle size. Understanding the fiber's removal mechanism was of critical importance in understanding the key factors in MSF reduction, i.e. the use of a slurry with small abrasive particles.

- The Nylon 6/6 tool showed to have a stable exponential load decay over long polishing times. Although not explored here, this stable and repeatable load decay offers the potential to deterministically compensate for the drop-off in the applied load as the polishing progresses with time.
- Fiber based tools were shown to have a relatively stable TIF. Raster polishing tests with the Nylon 6/6 tool showed that the tools TIF remained relatively stable during the polishing operation. The result was verified by comparing the experimental polishing outcome with expected material removal profiles as predicted by convolution. The polishing removal predicted by convolution and the measured experimental removal were in better agreement when the testing was done with the inline slurry feed setup. This was speculated to be mainly attributable to the similar slurry mixing conditions in the spot test (used for the convolution), and the translation test, when using the inline slurry feed system over the slurry bath configuration.
- The extent of fiber wear (Nylon 6/6) over the course of 5.5 hours of polishing was quantified. It was shown that the fiber wear flats were less than 5 μm . This is

considered to be a relatively low value and is promising for implementation of the tools in long polishing runs.

7.1.3 Fiber based tools MSF reduction

- It was shown that fiber based tools have the ability to reduce preexisting MSF features with wavelengths of 1 mm and 2 mm. This key result, as the main contribution of this work, provides optical fabricators with an alternative approach that has never been used, in reducing MSF errors. The MSF reduction capability of the tools was confirmed under spot and translational testing conditions, as well as under different spindle speeds and tool feedrates.

7.1.4 Tool integration in multi axis CNC machines

- The Nylon 6/6 tool was fully integrated in commercial 3-axis (Haas TM-1) and 5-axis (OptiPro Triumph) CNC machines. The tool was successfully traversed on planar and non-planar surfaces without any fiber entanglement, or pull-out issues under a range of spindle speeds and feedrates. The tool was able to fully preserve its contact form during the polishing.

7.1.5 Predictive FE modeling

- A finite element model (FEM) for studying the fiber-workpiece fundamental interaction was created. Initially this FEM was leveraged to obtain the fiber contact pressure distributions on planar and non-planar samples. The contact pressure profiles from the FEM greatly resembled the material removal profile of the fiber based tools. This resemblance suggested that the fiber material removal is driven by the fiber's applied load, and thus supporting the Prestonian behavior of fiber based tools.

- The same FEM was used to understand and support the MR theory of fiber based tools. As a corollary of the MR mechanism of the fiber based tools, it was shown that the polishing process width should be larger than that of the physical contact length of the fiber on the workpiece. Two FE outputs, CPRESS and COPEN were used to compare the expected fiber contact length and expected process width respectively. The values of the aforementioned parameters supported the MR mechanism of the fiber based tool that polishing with larger abrasive particles correspond to larger tool processing widths.
- The same FEM was used to predict the interaction between the fiber and the edge of the workpiece, i.e. the extent of edge roll off. For the Nylon 6/6 fiber, the FEM predicted a roll off zone of 0.2 mm in width. This value compares reasonably well to that obtained experimentally, 0.5 mm. The small value of edge roll-off of the Nylon 6/6 tool when compared to conventional pad tools, 2-3 mm [24, 25, 137, 138], was very promising. The other promising result with respect to the behavior of the tool near edge was that the removal profile of the fibers on the surface were not affected by the fibers that were off the surface. This is not the case for conventional polishing pad tools.
- The original FEM was complemented with an additional model to evaluate the fiber deflection between MSF features; this FEM, referred to as the two-step FEM, used the pressure profile obtained from the first FEM on a portion of the fiber that was assumed to be in contact with a pair of MSF features. The results of the two-step FEM were of great help in identification of key fiber properties affecting the fiber

deformation to MSF features. i.e. fiber geometry. The FEM results supported the MSF reduction polishing outcomes.

- An alternative fiber design with the potential of higher MSF reduction efficiency was introduced. In this simple design, it was proposed that a fiber with a non-uniform cross-sectional area, that promoted higher fiber stiffness in the zone where the fiber was engaged with the MSF features, could not only increase the MSF reduction efficiency of fiber based tools, it can also enable the reduction of MSF's with longer wavelengths (> 2 mm). The FEM supported the advantage of this design by predicting very low fiber deformation values for the proposed design.

7.2 Future Directions

The work to date on the fiber based tools has focused on understanding the MR of the tools, as well as a demonstrating that the tools can reduce MSF features. It is believed that there are two areas that are worthy of future investigations; (1) alternative tool designs, and (2) optimization of the polishing process.

7.2.1 Tool and fiber design

- Not much of an attention was paid to the material of the fibers for the work presented here. The interaction of the fiber with the slurry's abrasive particles is of key importance in the removal mechanism. Changes in the fiber surface property that could impact this interaction could be of great interest. For instance, the effect of a having a hydrophilic vs a hydrophobic fiber. The majority of fibers tested in this work appeared hydrophobic in nature; this would not assist in retaining abrasives at the fibers leading edge, yet MR existed.

- In this dissertation, there was discussion about how different fiber geometries can significantly change the polishing outcomes. As a direction for pursuance of this path it is believed that the design of alternative fiber geometries could focus the application of a given tool. One example of such designs was discussed in chapter 6, the dumbbell. The large design space of the fibers, nonetheless, still allows for new configurations.
- As mentioned earlier, a limited number of tool designs were introduced in this dissertation, i.e. all the work in this dissertation was based on the simple paint brush tool design or some variation of that design. That said, the design space for alternative tooling configurations remains very large. Many other arrangements of fibers can give rise to different fiber tooling that could be pursued in the future.

7.2.2 Process optimization

- One of the issues raised with respect to the fiber based tools was the long polishing times associated with these tools. Exploring options for increasing the MR, and hence reducing this polishing time, would be of great interest for achieving higher process yields. Increasing the number of fibers per tool and exploring maximum tool operating speeds are two obvious approaches. Optimal slurry composition for the process should also be considered.
- Another limitation of the tools, was the exponential load decay of the fibers with process time. Investigation on solutions that would mitigate this issue will be another avenue that can be pursued.
- Investigation on the performance of the tools on freeform optics and their global compliance to such geometries. While the tools were successfully used on spherical

components, testing did not include surfaces with varying ROC. This could be a topic for future studies on the application of these tools in polishing freeform and aspherical optics. One effort that is currently underway, is the adoption of an analytical model for predicting the fiber loads and contact lengths at various ROC and tool ΔZ . The full implementation of this method will provide the expected MRR of the tool at any given position of the tool based on the geometry of part under process and the ΔZ of the tool. The expected varying MRR with the ROC can be incorporated into the dwell time matrix calculation. This means that with a given set of fiber properties, i.e. material, geometry, and length, the tool can be adjusted as such that would efficiently finish the freeform part.

- For full integration of these tools in an industrial market, intensive testing and optimization is required to maximize MRs and minimize processing induced form errors. The parameters for optimization include a range of process kinematics such as spindle RPM, and spindle feedrates, polishing tool paths, environmental control, slurry composition etc.

To summarize, the main factors affecting the fiber based polishing process are illustrated in Figure 7-1. Most of the items in this map were explored within this body work and a good understanding was established, nevertheless, the isolation of the most optimal parameters remains as future work. Currently a US patent application has been filed for the application of these tools in finishing optics [141].

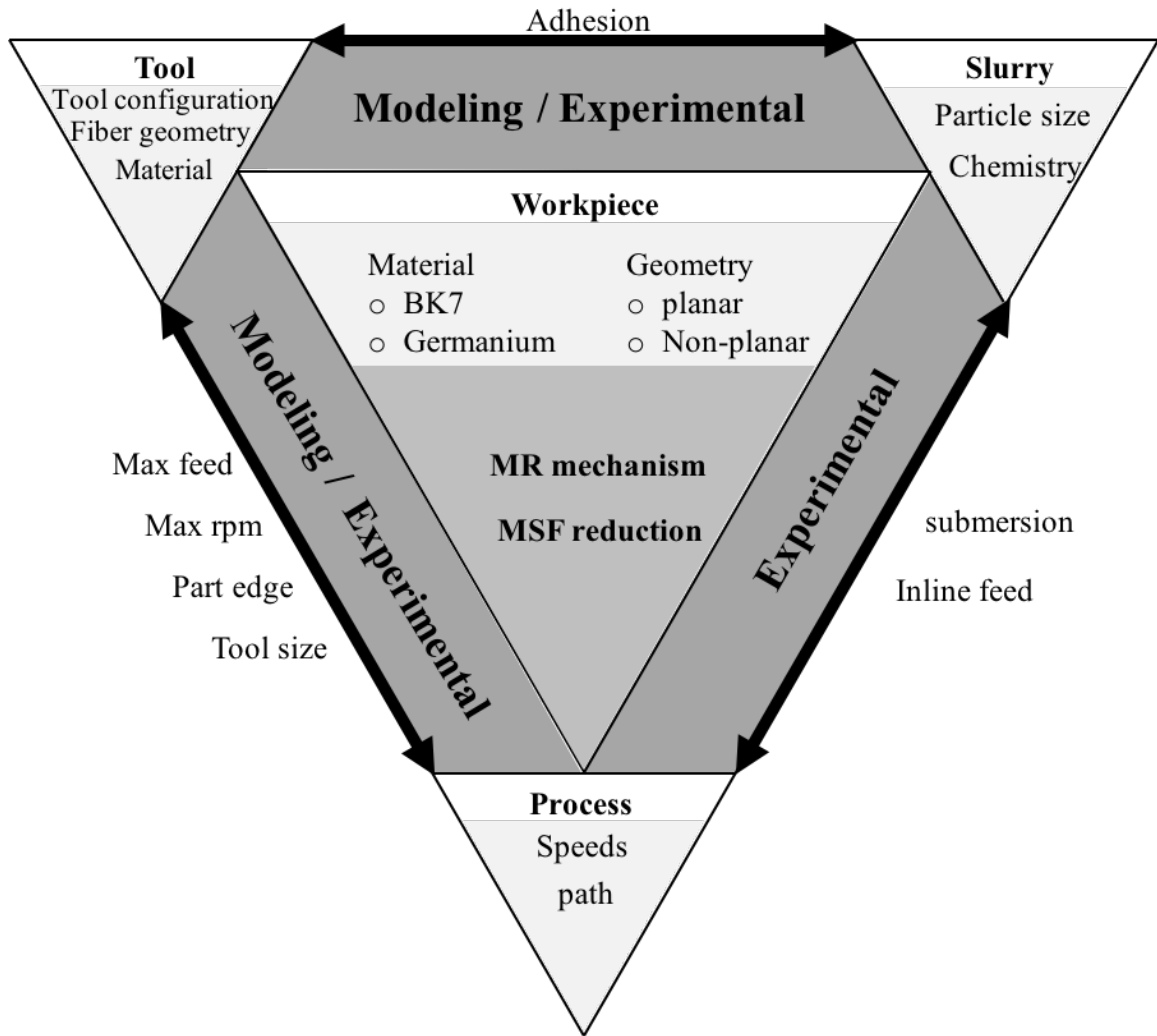


Figure 7-1 Fiber based polishing process map

REFERENCES

1. Enoch, J.M. *The fascinating early history of optics! Archaeological optics 2009: our knowledge of the early history of lenses, mirrors, and artificial eyes!* in *SPIE Optical Engineering+ Applications*. 2009. International Society for Optics and Photonics.
2. Mellaart, J., *Çatal Hüyük: a neolithic town in Anatolia*. 1967: McGraw-Hill.
3. Smethwick, F., *An Account of the Invention of Grinding Opticke and Burning Glass of a figure not-spherical, produced before the Royal Society*. *Philosophical Transactions*. **3**(33): p. 631-632.
4. *Aspheric*. [cited 2016 July 13]; Available from: <http://www.merriam-webster.com/dictionary/aspheric>.
5. Braunecker, B., R. Hentschel, and H.J. Tiziani, *Advanced optics using aspherical elements*. Vol. 173. 2008: Spie Press.
6. Bateau, J. and P.P. Clark. *The optics of miniature digital camera modules*. in *Contract Proceedings 2006*. 2007. International Society for Optics and Photonics.
7. Shannon, R.R., *CHAPTER 3 - Aspheric Surfaces*, in *Applied Optics and Optical Engineering*, S. Robert R and W. James C, Editors. 1980, Elsevier. p. 55-85.
8. Jiang, X., P. Scott, and D. Whitehouse, *Freeform surface characterisation-a fresh strategy*. *CIRP Annals-Manufacturing Technology*, 2007. **56**(1): p. 553-556.
9. Alvarez, L.W., *Two-element variable-power spherical lens*. 1967, Google Patents.
10. Thompson, K.P. and J.P. Rolland, *Freeform Optical Surfaces: A Revolution in Imaging Optical Design*. *Optics and Photonics News*, 2012. **23**(6): p. 30-35.

11. Fang, F., X. Zhang, A. Weckenmann, G. Zhang, and C. Evans, *Manufacturing and measurement of freeform optics*. CIRP Annals-Manufacturing Technology, 2013. **62**(2): p. 823-846.
12. Plummer, W.T., *Unusual optics of the Polaroid SX-70 Land camera*. Applied Optics, 1982. **21**(2): p. 196-202.
13. Boyce, P., C. Hunter, and S. Vasconez, *An evaluation of three types of gas station canopy lighting*. LRCRPIT, NY, 2001: p. 12180-3352.
14. Hicks, R.A., *Controlling a ray bundle with a free-form reflector*. Optics letters, 2008. **33**(15): p. 1672-1674.
15. Berggren, R.R. and R.A. Schmell. *Pad polishing for rapid production of large flats*. in *Optical Science, Engineering and Instrumentation'97*. 1997. International Society for Optics and Photonics.
16. Brown, N., *Optical polishing pitch*. 1977, California Univ., Livermore (USA). Lawrence Livermore Lab.
17. Martin, H., J. Angel, and A. Cheng. *Use of an actively stressed lap to polish a 1.8-m F/1 paraboloid*. in *European Southern Observatory Conference and Workshop Proceedings*. 1988.
18. Lubliner, J. and J.E. Nelson, *Stressed mirror polishing. 1: A technique for producing nonaxisymmetric mirrors*. Applied Optics, 1980. **19**(14): p. 2332-2340.
19. Nelson, J.E., G. Gabor, L.K. Hunt, J. Lubliner, and T.S. Mast, *Stressed mirror polishing. 2: Fabrication of an off-axis section of a paraboloid*. Applied Optics, 1980. **19**(14): p. 2341-2352.
20. Nelson, J. *The Proposed University of California Ten-Meter Telescope*. in *Proceedings, Conference on Optical Telescopes of the Future, December 1977*. 1978.
21. Beckstette, K., M. Küchel, and E. Heynacher, *Large mirror figuring and testing*. Astrophysics and Space Science, 1989. **160**(1): p. 207-214.

22. Martin, H.M., D.S. Anderson, J.R.P. Angel, R.H. Nagel, S.C. West, and R. Young. *Progress in the stressed-lap polishing of a 1.8-mf/1 mirror*. in *Astronomy'90, Tucson AZ, 11-16 Feb 90*. 1990. International Society for Optics and Photonics.
23. Anderson, D.S., J.R.P. Angel, J.H. Burge, W.B. Davison, S.T. DeRigne, B. Hille, D.A. Ketelsen, W. Kittrell, H.M. Martin, and R.H. Nagel. *Stressed-lap polishing of 3.5-mf/1.5 and 1.8-mf/1.0 mirrors*. in *8th Intl Symp on Gas Flow and Chemical Lasers*. 1992. International Society for Optics and Photonics.
24. Cai, G., Y. Lu, R. Cai, and H. Zheng, *Analysis on lapping and polishing pressure distribution*. CIRP Annals-Manufacturing Technology, 1998. **47**(1): p. 235-238.
25. Lo, S.-P., Y.-Y. Lin, and J.-C. Huang, *Analysis of retaining ring using finite element simulation in chemical mechanical polishing process*. The International Journal of Advanced Manufacturing Technology, 2007. **34**(5-6): p. 547-555.
26. Preston, F., *The theory and design of plate glass polishing machines*. J. Soc. Glass Tech., 1927. **11**: p. 214.
27. Evans, C., E. Paul, D. Dornfeld, D. Lucca, G. Byrne, M. Tricard, F. Klocke, O. Dambon, and B. Mullany, *Material removal mechanisms in lapping and polishing*. CIRP Annals-Manufacturing Technology, 2003. **52**(2): p. 611-633.
28. Newton, I., *Opticks, or, a treatise of the reflections, refractions, inflections & colours of light*. 1979: Courier Corporation.
29. Samuels, L.E., *Metallographic polishing by mechanical methods*. 2003: Asm International.
30. Beilby, G.T., *Aggregation and Flow of Solids: Being the Records of an Experimental Study of the Micro-structure and Physical Properties of Solids in Various States of Aggregation, 1900-1921*. 1921: Macmillan and Company, limited.
31. Izumitani, T. and S. Harada, *Polishing mechanism of optical glasses*. Glass Technology, 1971. **12**(5): p. 131-+.
32. Cook, L.M., *Chemical processes in glass polishing*. Journal of non-crystalline solids, 1990. **120**(1): p. 152-171.

33. Brown, N., *Some speculations on the mechanisms of abrasive grinding and polishing*. Precision Engineering, 1987. **9**(3): p. 129-138.
34. Paul, E., *A model of chemical mechanical polishing*. Journal of the Electrochemical Society, 2001. **148**(6): p. G355-G358.
35. Paul, E., *Application of a CMP model to tungsten CMP*. Journal of The Electrochemical Society, 2001. **148**(6): p. G359-G363.
36. Suratwala, T., W. Steele, M. Feit, N. Shen, R. Dylla-Spears, L. Wong, P. Miller, R. Desjardin, and S. Elhadj, *Mechanism and simulation of removal rate and surface roughness during optical polishing of glasses*. Journal of the American Ceramic Society, 2016. **99**(6): p. 1974-1984.
37. Suratwala, T., W. Steele, L. Wong, M.D. Feit, P.E. Miller, R. Dylla-Spears, N. Shen, and R. Desjardin, *Chemistry and formation of the Beilby layer during polishing of fused silica glass*. Journal of the American Ceramic Society, 2015. **98**(8): p. 2395-2402.
38. Suratwala, T., M. Feit, W. Steele, L. Wong, N. Shen, R. Dylla-Spears, R. Desjardin, D. Mason, P. Geraghty, and P. Miller, *Microscopic removal function and the relationship between slurry particle size distribution and workpiece roughness during pad polishing*. Journal of the American Ceramic Society, 2014. **97**(1): p. 81-91.
39. Arrasmith, S.R., I.A. Kozhinova, L.L. Gregg, A.B. Shorey, H.J. Romanofsky, S.D. Jacobs, D. Golini, W.I. Kordonski, S.J. Hogan, and P. Dumas. *Details of the polishing spot in magnetorheological finishing (MRF)*. in *SPIE's International Symposium on Optical Science, Engineering, and Instrumentation*. 1999. International Society for Optics and Photonics.
40. Westover, S., C. Hall, and M. DeMarco. *Improved MRF spot characterization with QIS metrology*. in *SPIE Optifab*. 2013. International Society for Optics and Photonics.
41. Aspden, R., R. McDonough, and F.R. Nitchie, *Computer assisted optical surfacing*. Applied optics, 1972. **11**(12): p. 2739-2747.
42. Jones, R.A., *Optimization of computer controlled polishing*. Applied optics, 1977. **16**(1): p. 218-224.

43. Jones, R.A. *Grinding and polishing with small tools under computer control*. in *Los Angeles Technical Symposium*. 1979. International Society for Optics and Photonics.
44. Namba, Y. and H. Tsuwa, *Ultrafine Finishing of Ceramics and Metals by Float Polishing*, in *Laser Induced Damage in Optical Materials: 1980*. 1981, ASTM International.
45. Ando, M., M. Negishi, M. Takimoto, A. Deguchi, N. Nakamura, M. Higomura, and H. Yamamoto. *Super-smooth surface polishing on aspherical optics*. in *Intl Symp on Optical Fabrication, Testing, and Surface Evaluation*. 1992. International Society for Optics and Photonics.
46. Kordonsky, W.I., I.V. Prokhorov, S.R. Gorodkin, G.R. Gorodkin, L.K. Gleb, and B.E. Kashevsky, *Magnetorheological polishing devices and methods*. 1995, Google Patents.
47. Jacobs, S.D., D. Golini, Y. Hsu, B.E. Puchebner, D. Strafford, I.V. Prokhorov, E.M. Fess, D. Pietrowski, and W.I. Kordonski. *Magnetorheological finishing: a deterministic process for optics manufacturing*. in *International Conferences on Optical Fabrication and Testing and Applications of Optical Holography*. 1995. International Society for Optics and Photonics.
48. Kordonski, W.I. and S. Jacobs, *Magnetorheological finishing*. *International Journal of Modern Physics B*, 1996. **10**(23n24): p. 2837-2848.
49. Föhnle, O.W., H. Van Brug, and H.J. Frankena, *Fluid jet polishing of optical surfaces*. *Applied optics*, 1998. **37**(28): p. 6771-6773.
50. Föhnle, O.W. and H.H. van Brug. *Fluid jet polishing: removal process analysis*. in *Optical Systems Design and Production*. 1999. International Society for Optics and Photonics.
51. Bingham, R.G., D.D. Walker, D.-H. Kim, D. Brooks, R. Freeman, and D. Riley. *Novel automated process for aspheric surfaces*. in *Current developments in lens design and optical systems engineering*. 2000. International Society for Optics and Photonics.
52. Walker, D.D., R. Freeman, G. McCavana, R. Morton, D. Riley, J. Simms, D. Brooks, E. Kim, and A. King. *Zeeko/UCL process for polishing large lenses and prisms*. in *Large lenses and prisms*. 2002. International Society for Optics and Photonics.

53. Tricard, M., W. Kordonski, A. Shorey, and C. Evans, *Magnetorheological jet finishing of conformal, freeform and steep concave optics*. CIRP Annals-Manufacturing Technology, 2006. **55**(1): p. 309-312.
54. Kordonski, W. and A. Shorey, *Magnetorheological (MR) jet finishing technology*. Journal of Intelligent Material Systems and Structures, 2007. **18**(12): p. 1127-1130.
55. Wilson, S., D. Reicher, and J. McNeil. *Surface figuring using neutral ion beams*. in *Advances in Fabrication and Metrology for Optics and Large Optics*. 1989. International Society for Optics and Photonics.
56. Mori, Y., K. Yamauchi, and K. Endo, *Elastic emission machining*. Precision Engineering, 1987. **9**(3): p. 123-128.
57. Mori, Y., K. Yamauchi, and K. Endo, *Mechanism of atomic removal in elastic emission machining*. Precision Engineering, 1988. **10**(1): p. 24-28.
58. Takino, H., N. Shibata, H. Itoh, T. Kobayashi, H. Tanaka, M. Ebi, K. Yamamura, Y. Sano, and Y. Mori, *Computer numerically controlled plasma chemical vaporization machining with a pipe electrode for optical fabrication*. Applied optics, 1998. **37**(22): p. 5198-5210.
59. Walker, D.D., A. Beaucamp, D. Brooks, R. Freeman, A. King, G. McCavana, R. Morton, D. Riley, and J. Simms. *Novel CNC polishing process for control of form and texture on aspheric surfaces*. in *International Symposium on Optical Science and Technology*. 2002. International Society for Optics and Photonics.
60. Walker, D., D. Brooks, A. King, R. Freeman, R. Morton, G. McCavana, and S.-W. Kim, *The ?? Precessions ?? tooling for polishing and figuring flat, spherical and aspheric surfaces*. Optics Express, 2003. **11**(8): p. 958-964.
61. Walker, D.D., A.T. Beaucamp, D. Brooks, V. Doubrovski, M.D. Cassie, C. Dunn, R.R. Freeman, A. King, M. Libert, and G. McCavana. *New results from the Precessions polishing process scaled to larger sizes*. in *SPIE Astronomical Telescopes+ Instrumentation*. 2004. International Society for Optics and Photonics.
62. Beaucamp, A., Y. Namba, and P. Charlton, *Corrective finishing of extreme ultraviolet photomask blanks by precessed bonnet polisher*. Applied Optics, 2014. **53**(14): p. 3075-3080.

63. *UFF 300*. [cited 2017 May 24]; Available from: <http://www.optipro.com/cnc-aspheric-uff300.html>.
64. Harris, D.C. *History of magnetorheological finishing*. in *SPIE Defense, Security, and Sensing*. 2011. International Society for Optics and Photonics.
65. Golini, D., W.I. Kordonski, P. Dumas, and S.J. Hogan. *Magnetorheological finishing (MRF) in commercial precision optics manufacturing*. in *SPIE's International Symposium on Optical Science, Engineering, and Instrumentation*. 1999. International Society for Optics and Photonics.
66. Shorey, A.B., S.D. Jacobs, W.I. Kordonski, and R.F. Gans, *Experiments and observations regarding the mechanisms of glass removal in magnetorheological finishing*. *Applied Optics*, 2001. **40**(1): p. 20-33.
67. Kordonski, W. and S. Gorodkin, *Material removal in magnetorheological finishing of optics*. *Applied Optics*, 2011. **50**(14): p. 1984-1994.
68. Whitehouse, D.J., *Handbook of surface and nanometrology*. 2010: CRC press.
69. Standard, A., *B46. 1 (2002) Surface Texture, Surface Roughness, Waviness and Lay*. The American Society of Mechanical Engineers, An American National Standard, 2002: p. 1-98.
70. Smith, W.J., *Modern optical engineering*. 1966: Tata McGraw-Hill Education.
71. Kingslake, R., *Optical system design*. 2012: Academic Press.
72. Greivenkamp, J.E., *Field guide to geometrical optics*. Vol. 1. 2004: SPIE Press Bellingham, WA.
73. von F, Z., *Beugungstheorie des schneidenver-fahrens und seiner verbesserten form, der phasenkontrastmethode*. *Physica*, 1934. **1**(7-12): p. 689-704.
74. Lakshminarayanan, V. and A. Fleck, *Zernike polynomials: a guide*. *Journal of Modern Optics*, 2011. **58**(7): p. 545-561.

75. Forbes, G., *Shape specification for axially symmetric optical surfaces*. Optics express, 2007. **15**(8): p. 5218-5226.
76. Kaya, I., K.P. Thompson, and J.P. Rolland, *Edge clustered fitting grids for φ -polynomial characterization of freeform optical surfaces*. Optics express, 2011. **19**(27): p. 26962-26974.
77. Forbes, G., *Characterizing the shape of freeform optics*. Optics express, 2012. **20**(3): p. 2483-2499.
78. *ISO 10110-5 Optics and Photonics: Preparation of Drawings for Optical Elements and Systems - Part 5: Surface form tolerances*. 2015, International Organization for Standardization.
79. *ISO 10110-12 Optics and Photonics: Preparation of Drawings for Optical Elements and Systems - Part 12: Aspheric Surfaces*. 2007, International Organization for Standardization.
80. *ISO 10110-19 Optics and Photonics: Preparation of Drawings for Optical Elements and Systems -Part 19: General description of surfaces and components*. 2015: International Organization for Standardization.
81. Barkas, W.W., *Analysis of light scattered from a surface of low gloss into its specular and diffuse components*. Proceedings of the Physical Society, 1939. **51**(2): p. 274.
82. Hunter, R.S., *A Glossmeter for Smoothness Comparisons of Machine-Finished Surfaces**. Journal of the Optical Society of America, 1946. **36**(3): p. 178-181.
83. Hasunuma, H. and J. Nara, *On the Sheen Gloss*. Journal of the Physical Society of Japan, 1956. **11**(1): p. 69-75.
84. Bennett, H.E. and J.O. Porteus, *Relation Between Surface Roughness and Specular Reflectance at Normal Incidence*. Journal of the Optical Society of America, 1961. **51**(2): p. 123-129.
85. Harvey, J.E., S. Schröder, N. Choi, and A. Duparré, *Total integrated scatter from surfaces with arbitrary roughness, correlation widths, and incident angles*. Optical Engineering, 2012. **51**(1): p. 013402-1-013402-11.

86. Raja, J., B. Muralikrishnan, and S. Fu, *Recent advances in separation of roughness, waviness and form*. Precision Engineering, 2002. **26**(2): p. 222-235.
87. *ISO 10110-8 Optics and Photonics: Preparation of Drawings for Optical Elements and Systems - Part 8: Surface Texture; Roughness and Waviness*. 2015: International Organization for Standardization.
88. *ISO 25178-2, Geometrical Product Specifications (GPS) - Surface texture: Areal - part 2: Terms, definitions and surface texture parameters*. 2012, International Organization for Standardization.
89. *ISO 16610-1, Geometrical Product Specifications (GPS) - Filtration: Areal - part 1: Overview and basic concepts*. 2015, International Organization for Standardization.
90. *ISO 16610-60, Geometrical Product Specifications (GPS) - Filtration: Areal - part 60: Linear areal filters - Basic concepts*. 2015, International Organization for Standardization.
91. *ISO 16610-61, Geometrical Product Specifications (GPS) - Filtration: Areal - part 61: Linear areal filters - Gaussian Filters*. 2015, International Organization for Standardization.
92. *ISO 16610-71, Geometrical Product Specifications (GPS) - Filtration: Areal - part 71: Robust areal filters - Gaussian regression filters*. 2014, International Organization for Standardization.
93. Hull, T., M.J. Riso, J.M. Barentine, and A. Magruder. *Mid-spatial frequency matters: examples of the control of the power spectral density and what that means to the performance of imaging systems*. in *SPIE Defense, Security, and Sensing*. 2012. International Society for Optics and Photonics.
94. Parks, R.E. *Specifications: Figure and Finish are not enough*. in *Optical Engineering+ Applications*. 2008. International Society for Optics and Photonics.
95. Noll, R.J., *Effect of mid-and high-spatial frequencies on optical performance*. Optical Engineering, 1979. **18**(2): p. 182137-182137-.

96. Harvey, J.E. and A.K. Thompson. *Scattering effects from residual optical fabrication errors*. in *International Conferences on Optical Fabrication and Testing and Applications of Optical Holography*. 1995. International Society for Optics and Photonics.
97. Goodman, J.W., *Introduction to Fourier optics*. 2005: Roberts and Company Publishers.
98. Rasigni, G., F. Varnier, M. Rasigni, J. Palmari, and A. Llebaria, *Spectral-density function of the surface roughness for polished optical surfaces*. JOSA, 1983. **73**(10): p. 1235-1239.
99. Church, E., T. Vorburger, and J. Wyant, *Direct comparison of mechanical and optical measurements of the finish of precision machined optical surfaces*. Optical Engineering, 1985. **24**(3): p. 243388-243388-.
100. Church, E.L. and P.Z. Takacs. *Optimal estimation of finish parameters*. in *San Diego, '91, San Diego, CA*. 1991. International Society for Optics and Photonics.
101. Lawson, J.K., C.R. Wolfe, K.R. Manes, J.B. Trenholme, D.M. Aikens, and R.E. English Jr. *Specification of optical components using the power spectral density function*. in *SPIE's 1995 International Symposium on Optical Science, Engineering, and Instrumentation*. 1995. International Society for Optics and Photonics.
102. Aikens, D. *The origin and evolution of the optics specifications for the National Ignition Facility [2536-01]*. in *PROCEEDINGS-SPIE THE INTERNATIONAL SOCIETY FOR OPTICAL ENGINEERING*. 1995. SPIE INTERNATIONAL SOCIETY FOR OPTICAL.
103. Aikens, D.M., C.R. Wolfe, and J.K. Lawson. *Use of power spectral density (PSD) functions in specifying optics for the National Ignition Facility*. in *International Conferences on Optical Fabrication and Testing and Applications of Optical Holography*. 1995. International Society for Optics and Photonics.
104. Lawson, J.K., D.M. Aikens, R.E. English Jr, and C.R. Wolfe. *Power spectral density specifications for high-power laser systems*. in *Optical Instrumentation & Systems Design*. 1996. International Society for Optics and Photonics.

105. Aikens, D.M., A. Roussel, and M. Bray. *Derivation of preliminary specifications for transmitted wavefront and surface roughness for large optics used in inertial confinement fusion*. in *Solid State Lasers for Application to Inertial Confinement Fusion (ICF)*. 1995. International Society for Optics and Photonics.
106. Takacs, P.Z. *Minimizing artifacts in analysis of surface statistics*. in *Optical Fabrication and Testing*. 2012. Optical Society of America.
107. Youngworth, R.N., B.B. Gallagher, and B.L. Stamper. *An overview of power spectral density (PSD) calculations*. in *Optics & Photonics 2005*. 2005. International Society for Optics and Photonics.
108. Youngworth, R.N. and B.D. Stone, *Simple estimates for the effects of mid-spatial-frequency surface errors on image quality*. *Applied optics*, 2000. **39**(13): p. 2198-2209.
109. Tamkin, J.M., T.D. Milster, and W. Dallas, *Theory of modulation transfer function artifacts due to mid-spatial-frequency errors and its application to optical tolerancing*. *Applied optics*, 2010. **49**(25): p. 4825-4835.
110. *ISO 10110-8 Optics and Photonics: Preparation of Drawings for Optical Elements and Systems - Part 8: Surface Texture; Roughness and Waviness*. 2015, International Organization for Standardization.
111. Parks, R. and C. Evans, *Rapid post-polishing of diamond-turned optics*. *Precision engineering*, 1994. **16**(3): p. 223-227.
112. Klinger, C., *Vibe: A new process for high speed polishing of optical elements*. *Optifab: Technical Digest*, SPIE Technical Digest TD04, 2007.
113. Nelson, J., A. Gould, C. Klinger, and M. Mandina. *Incorporating VIBE into the precision optics manufacturing process*. in *Proc. SPIE*. 2011.
114. Wang, T., H. Cheng, W. Zhang, H. Yang, and W. Wu, *Restraint of path effect on optical surface in magnetorheological jet polishing*. *Applied Optics*, 2016. **55**(4): p. 935-942.
115. Dunn, C.R. and D.D. Walker, *Pseudo-random tool paths for CNC sub-aperture polishing and other applications*. *Optics express*, 2008. **16**(23): p. 18942-18949.

116. Wang, C., Z. Wang, and Q. Xu, *Unicursal random maze tool path for computer-controlled optical surfacing*. Applied optics, 2015. **54**(34): p. 10128-10136.
117. Dong, Z., H. Cheng, and H.-Y. Tam, *Modified dwell time optimization model and its applications in subaperture polishing*. Applied optics, 2014. **53**(15): p. 3213-3224.
118. Wang, T., H. Cheng, H. Yang, W. Wu, and H. Tam, *Controlling mid-spatial frequency errors in magnetorheological jet polishing with a simple vertical model*. Applied optics, 2015. **54**(21): p. 6433-6440.
119. Dong, Z., H. Cheng, and H.-Y. Tam, *Further investigations on fixed abrasive diamond pellets used for diminishing mid-spatial frequency errors of optical mirrors*. Applied Optics, 2014. **53**(3): p. 327-334.
120. Taylor, J.S., M.A. Piscotty, N.Q. Nguyen, C.S. Landram, and L.C. Ng, *Efficient polishing of aspheric optics*. 1997, Lawrence Livermore National Lab., CA (United States).
121. Namba, Y. and H. Tsuwa, *Ultrafine Finishing of Ceramics and Metals by Float Polishing*. Laser Induced Damage in Optical Materials, 1980: p. 171-179.
122. Beaucamp, A. and Y. Namba, *Technological Advances in Super Fine Finishing*.
123. Mark, J.E., *Physical properties of polymers handbook*. 1996: Springer.
124. Gazonas, G.A., *Implementation of a finite strain plasticity model for Nylon 6/6 into DYNA3D*. Structures and Materials, 2000: p. 523-535.
125. Store, T.C. *Comparison Data for Pultruded Shapes*. [Web Page] 2017 July 23, 2017]; Available from: http://www.cstsales.com/rod_comp.html.
126. Gaylord, N.G. and P.M. Kamath, *Analytical chemistry of polymers, Vol. XII, Part III. Identification Procedures and Chemical Analysis*, G. M. K. APP Journal of Applied Polymer Science, 1964. **8**(3): p. 1500.
127. LTD, X.T.C. *Xebec Crosshole Deburring Tools*. [Web Page] 2017 Dec 21, 2017]; Available from: <https://www.xebec-tech.co.jp/en/support/dpdi6o0000000cmi-att/a1491788261424.pdf>.

128. Aghan, R. and L.E. Samuels, *Mechanisms of abrasive polishing*. Wear, 1970. **16**(4): p. 293-301.
129. Xie, Y. and B. Bhushan, *Effects of particle size, polishing pad and contact pressure in free abrasive polishing*. Wear, 1996. **200**(1): p. 281-295.
130. *ABAQUS, Version 6.13-4*. Dassault Systèmes Simulia Corp., Providence, RI.
131. *Hastilite PO Technical Data*. Universal Photonics Inc., Hicksville, New York, USA.
132. Li, Y., J. Hou, Q. Xu, J. Wang, W. Yang, and Y. Guo, *The characteristics of optics polished with a polyurethane pad*. Optics express, 2008. **16**(14): p. 10285-10293.
133. Marcos Piña, M.D., C. University of North Carolina at E. Department of Mechanical, and S. Engineering, *Development and evaluation of a deterministic computer controlled polishing system*. 2013.
134. Jabbar, A., J. Militký, B. Madhukar Kale, S. Rwawiire, Y. Nawab, and V. Baheti, *Modeling and analysis of the creep behavior of jute/green epoxy composites incorporated with chemically treated pulverized nano/micro jute fibers*. Industrial Crops and Products, 2016. **84**: p. 230-240.
135. Krempl, E. and F. Khan, *Rate (time)-dependent deformation behavior: an overview of some properties of metals and solid polymers*. International Journal of Plasticity, 2003. **19**(7): p. 1069-1095.
136. Lai, J. and A. Bakker, *An integral constitutive equation for nonlinear plasto-viscoelastic behavior of high-density polyethylene*. Polymer Engineering & Science, 1995. **35**(17): p. 1339-1347.
137. Kimura, M., Y. Saito, H. Daio, and K. Yakushiji, *A new method for the precise measurement of wafer roll off of silicon polished wafer*. Japanese journal of applied physics, 1999. **38**(1R): p. 38.
138. Enomoto, T., U. Satake, T. Miyake, and N. Tabata, *A newly developed polishing pad for achieving high surface flatness without edge roll off*. CIRP Annals-Manufacturing Technology, 2011. **60**(1): p. 371-374.

139. *Ultra-Sol Optiq.* [cited 2017 11/18]; Available from: http://www.eminess.com/products/polishing_slurries/cerium_oxide/ultra-sol_optiq.
140. Peddeti, S., P. Ong, L. Leunissen, and S. Babu, *Chemical mechanical polishing of Ge using colloidal silica particles and H₂O₂*. *Electrochemical and Solid-State Letters*, 2011. **14**(7): p. H254-H257.
141. Mullany, B. and H. Shahinian, *FIBER BASED FINISHING TOOLS*. 2016: United States Patent and Trademark Office.

Appendix A: Metrology Instruments

A variety of instruments for the measurement of the testing samples used in this dissertation, were employed. A brief introduction of such instruments is given in this appendix.

A.1 Taylor Hobson Talysurf 120-L

This instrument is a mechanical profiler, where the tactile probe is dragged across a single trace on the surface and the surface variations are registered with a high level of repeatability. The tip of the mechanical probe is made of a 2.5 μm radius diamond, setting the limit for minimum lateral feature size detection. The height resolution is limited mainly by the noise floor in the detector that measures the motion of the probe. Typically features with larger values than 12 nm are detectable by this instrument, which makes it a good fit for measuring the MSF features in the scope of this work. The lump tilt in the stage and workpiece are not nulled out before the measurement. Therefore, a best fit line is always subtracted from the measurements of planar surfaces.

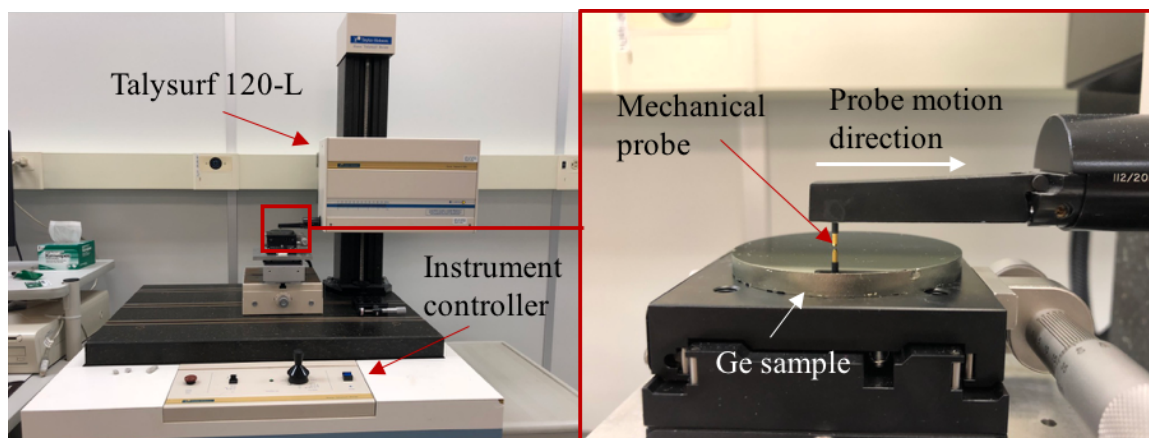


Figure A.1 Talysurf 120-L profilometer measuring the germanium sample

Figure A.1 shows the Talysurf 120-L profilometer measuring the germanium sample, described in Chapter 6.

A.2 Zygo Laser Fizeau Interferometer AT1000

This instrument uses a He-Ne laser at 632.5 nm wavelength for illumination of the target surface and reference surface. Figure A.2 shows a basic Fizeau interferometer setup for measuring a planar surface.

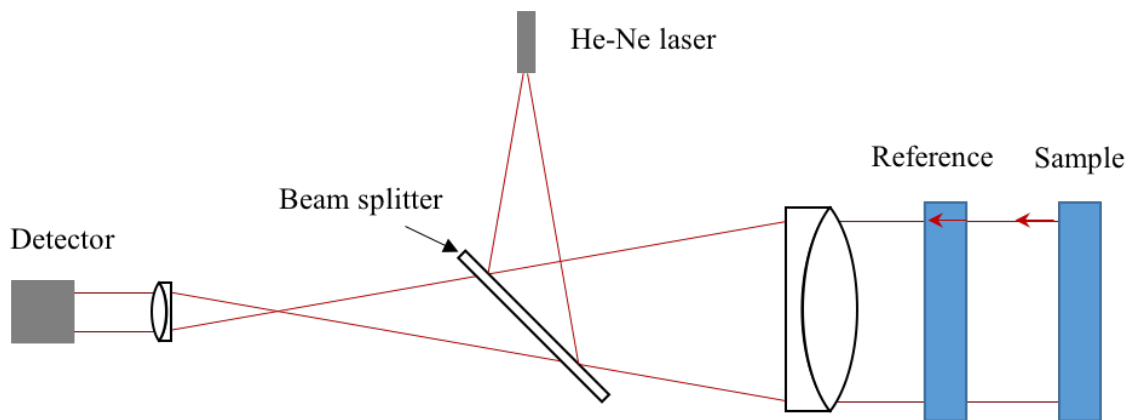


Figure A.2 Laser Fizeau interferometer setup

The laser produces a highly coherent light. This implies that the tolerance for sample placement in front of the interferometer are very forgiving. The reflected wavefront off the reference and the sample, interfere on the detector. The interference fringes created on the detector are then interpreted, and since the wavelength of the laser is known the height map representing the surface can be generated. The Fizeau interferometer used for the measurement of samples in this work is a Zygo Verifire AT1000. The instrument has a full aperture size of 101.6 mm. The detector size is 1000×1000 pixels. The instrument is also equipped with a magnification system up to 6 times of its original viewing. For the sake of the measurement of the MSF's even with the systems default magnification, the

spatial resolution is approximately $100\ \mu\text{m}$, limited by Nyquist. This value is an order of magnitude smaller than the premade MSF's tested ($1\ \text{mm}$).

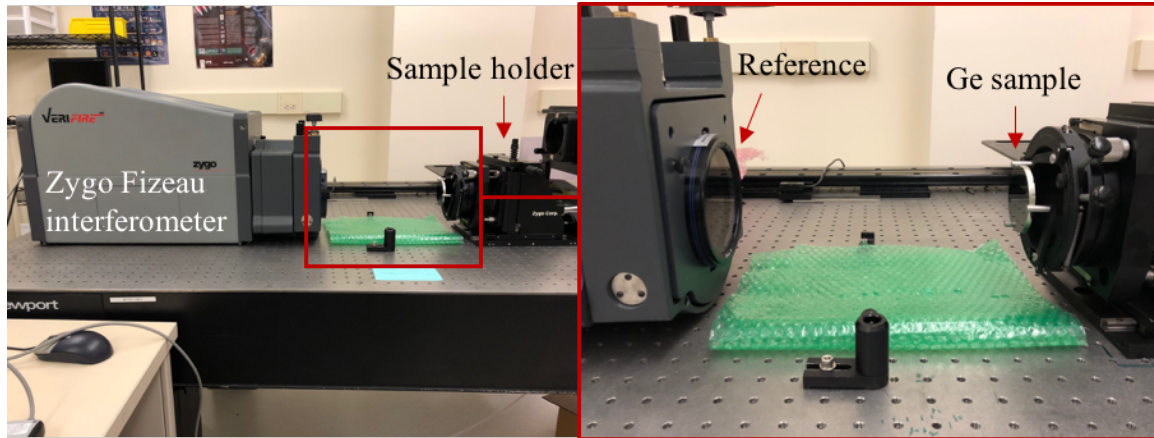


Figure A.3 Zygo Verifier AT1000 measuring germanium sample

Figure A.3 depicts the measurement of the germanium sample with the Zygo Verifire AT1000 laser Fizeau interferometer.

A.3 Zygo ZeGage

The last set of instruments presented, is the scanning white light interferometer (SWLI), mainly used for the measurement of finer surface features. The SWLI instruments, contrary to the Fizeau interferometer, use incoherent light. This limits the working range for this instrument to a very narrow space. Figure A.4 depicts a simple sketch of a SWLI. Essentially the light reflected from the sample and reference are correlated, only when the difference in the path traversed by the light from the “Beam splitter 2” to and from the sample and to and from the reference is less than the speed of light times the temporal coherence length of the light source. The coherence length for light sources in typical SWLI instruments is approximately $10\ \mu\text{m}$.

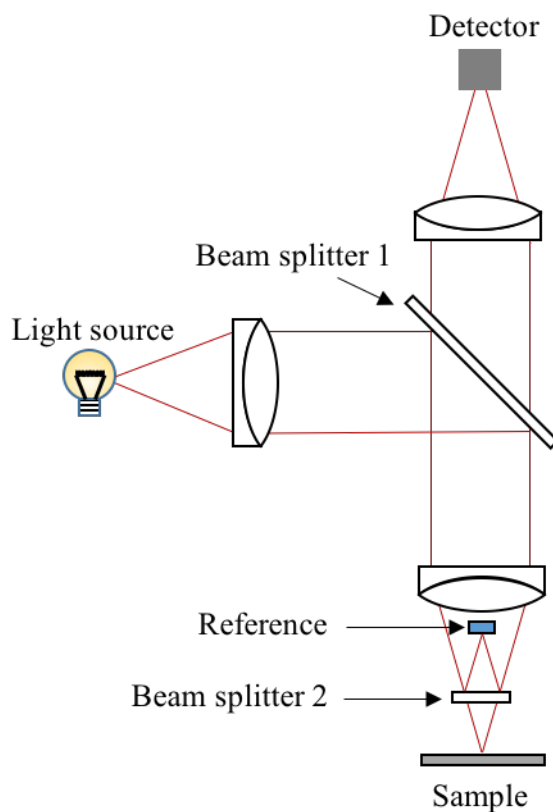


Figure A.4 SWLI basic setup

The SWLI used in this dissertation are designed and manufactured by Zygo. The instrument is equipped with electronically controlled stages, giving the ability to automatically acquire measurements from different segments. The Zygo ZeGage instrument has 1024×1024 camera size and noise levels below 0.1 nm. The field of view of the measurement depends on the magnifying objective used. For the scope of this work the majority of measurements are acquired with a 20 \times objective with a FOV of $417 \mu\text{m} \times 417 \mu\text{m}$. Figure A.5, shows the Zygo ZeGage SWLI measuring the germanium sample.

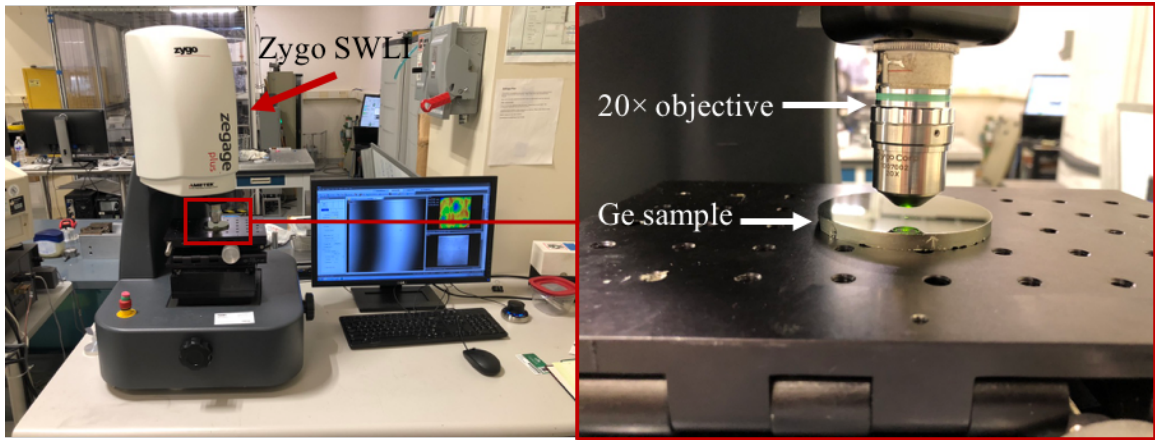


Figure A.5 Zygo ZeGage measuring Ge sample

Appendix B: ZERNIKE Polynomials

In this part of the appendix a brief introduction on the mathematical form of the Zernike polynomials, discussed in Chapter 2, is provided. View graphs of the first twenty-eight terms of the Zernike polynomials is also illustrated.

B.1 Mathematical Form

As mentioned in the introduction, the Zernike polynomials are orthogonal in the polar coordinate system. This property makes them a good candidate in expressing the wavefront error transmitted from optical components with circular apertures. As with any orthogonal set of base polynomials, the linear independence of the terms from one another, enables the expression of the total wavefront error as a linear combination of all the terms. Thus, the following can be stated:

$$W(r, \theta) = \sum_{m,n} C_n^m Z_n^m(r, \theta)$$

Where $W(r, \theta)$, is the total induced wavefront error, $Z_n^m(r, \theta)$ are the Zernike polynomials, C_n^m are the linear coefficients associated with each term. The Zernike polynomials have the general form as follows:

$$\begin{aligned} Z_n^m(r, \theta) &= R_n^m(r) \cos(m\theta) & m \geq 0 \\ Z_n^m(r, \theta) &= R_n^m(r) \sin(m\theta) & m < 0 \end{aligned}$$

Where $R_n^m(r)$ is expressed with the equation below:

$$R_n^m(r) = \sum_{l=0}^{\binom{n-m}{2}} \frac{(-1)^l (n-l)!}{l! [\frac{1}{2}(n+m) - l]! [\frac{1}{2}(n-m) - l]!} r^{n-2l}$$

Figure B.1 illustrates the first twenty-eight Zernike terms normalized to a PV of λ , where λ is the wavelength of the wavefront used.

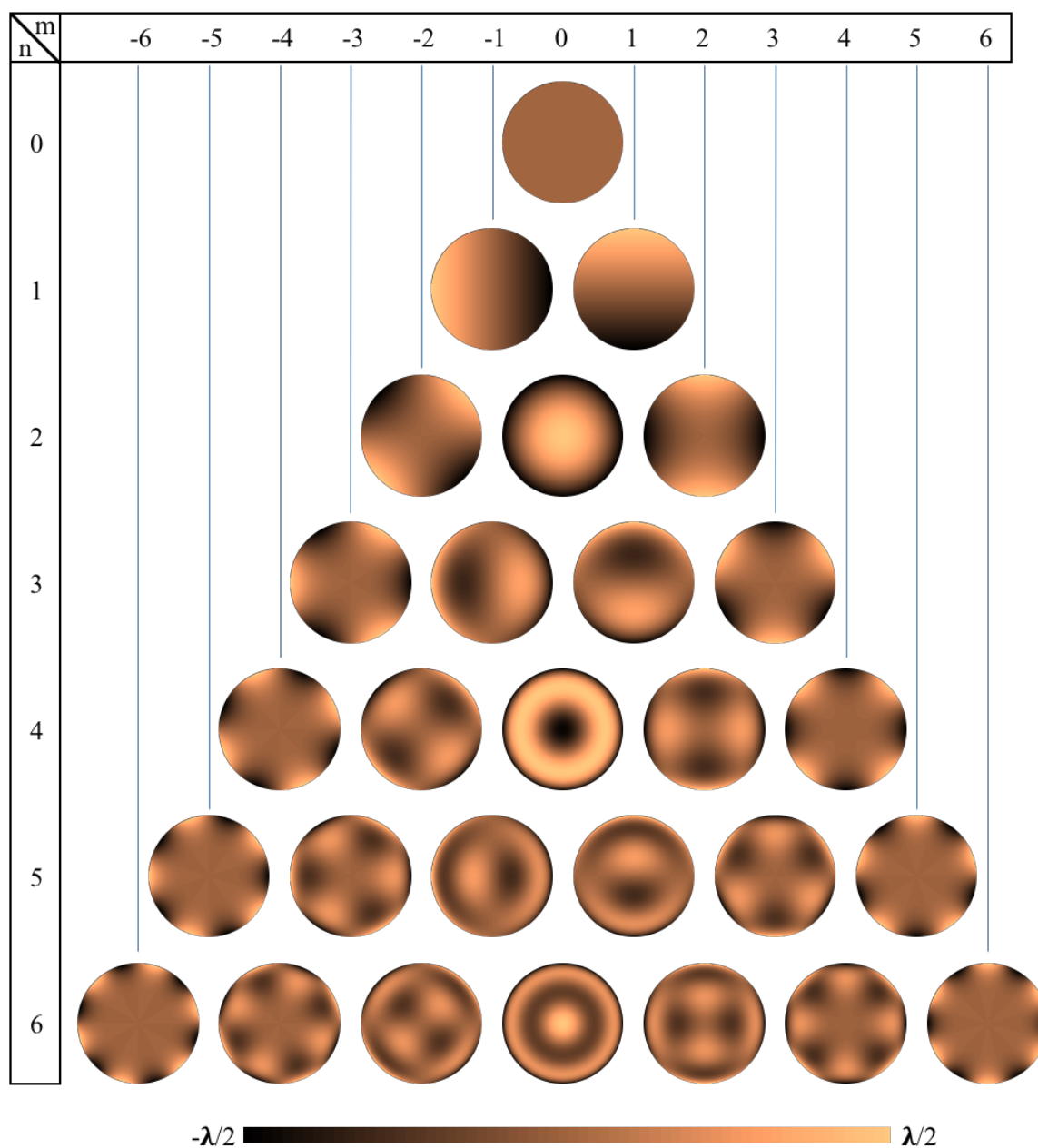


Figure B.1 First twenty eight Zernike terms, $Z_n^m(r, \theta)$, graphical representation

The power term used in Chapter 5 for the removal of system defocus is the Z_2^0 term, whereas the terms Z_0^0 , Z_1^{-1} , and Z_1^1 are used for the removal of best fit plane from the interferograms, acquired on the Fizeau interferometer. It should also be noted that the

rotationally varying (RV) terms, are them terms with $m \neq 0$, whereas the rotationally invariant terms are the terms with $m = 0$.

Appendix C: DR. Cherukuri and Dr. Hassan's Model

Through working with Dr. Cherukuri (UNCC ME Faculty) and Dr. Hassan (UNCC Post-doctoral student), an improved FE model was created. Their model is complimented with Euler's beam theory for evaluation of fiber deflection to multiple MSF features. In the new FEM, for inducing the initial bent to the fiber, instead of applying an angular displacement to the tip of the free end of the fiber, a linear load is applied. The magnitude of the load is set as such that the stresses induced in the fiber, as a result of the bending caused by this load, is less than the yield stress of the fiber. The linear load is then maintained on the tip, while simultaneously the fiber is moved down towards the workpiece. Once contact is initiated, the load is removed, and the fiber is bent further by the evolution of the contact between the workpiece and the fiber, by moving the fiber lower. The modeling steps described is illustrated in Figure C.1.

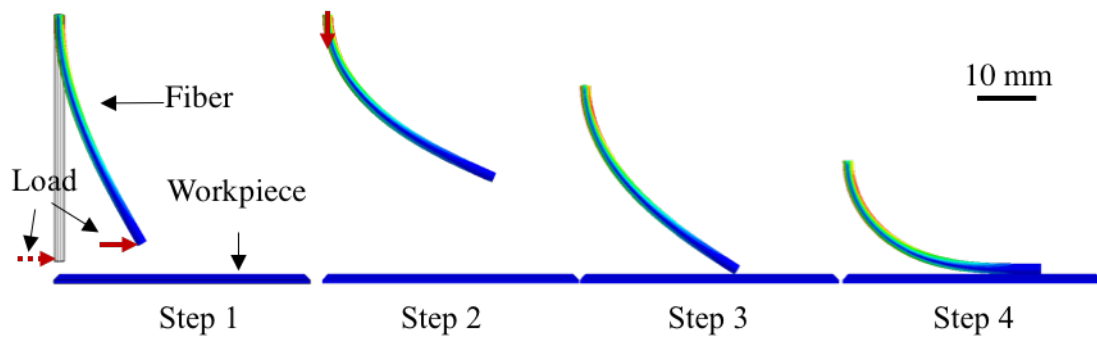


Figure C.1 Dr. Cherukuri and Dr. Hassan FEM steps

Once the model is fully converged, the reaction loads and moments on the fiber end not in contact with the workpiece, is evaluated. Next a section of the fiber, in contact with the workpiece, is modeled in a simple Euler beam configuration in contact with simple constraints. Each constraint represents a MSF feature peak. Therefore, the spacing between

these constraints are equal and set by the MSF wavelength of interest. Those values are applied to a simple beam model shown in Figure C.2 below.

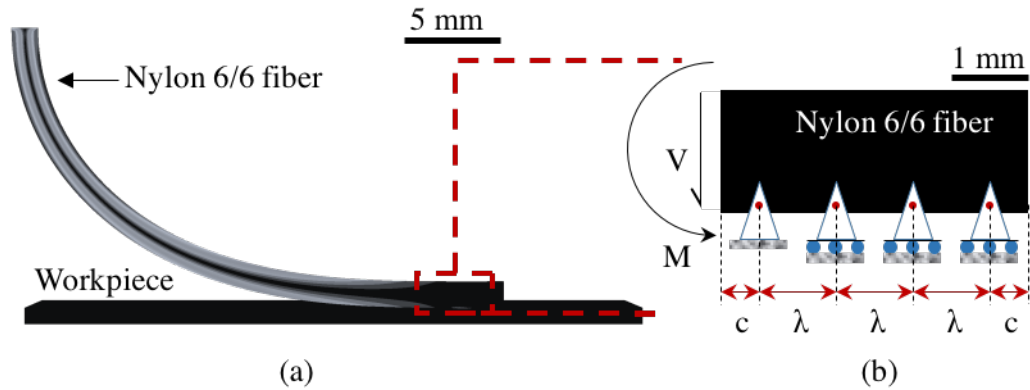


Figure C.2 (a) FEM model (b) Euler beam model using load (V) and moment (M) obtained from the FEM

The MSF wavelengths (λ) simulated are 1 mm and 2 mm. The Nylon 6/6 fiber with a diameter of 1.6 mm and fiber length of 37.5 mm was modeled. The material property of the fiber was set as the elastoplastic behavior with a Young's modulus of 2.27 GPa.

The maximum fiber deflection for two scenarios with MSF $\lambda = 1$ mm and MSF $\lambda = 2$ mm, were evaluated to be 10 nm and 40 nm respectively. These deflection values are much less than of those obtained in Chapter 6. The principle of higher efficiency in reducing MSF's with shorter wavelengths, nonetheless, is still valid. While it is believed that this model offers a sounder physics and thus more reliable results, it is believed that the absence of consideration for the relatively larger fiber cross section area – to fiber length, should be included in the future modeling efforts.

Appendix D: MATLAB codes guide

A large number of MATLAB codes for synthesis of the measurement data has been created. These codes can be found in the link below:

https://drive.google.com/open?id=0B_8KKwB5Qm54Nzc3TEEwNXdoZmM

For access to the codes please email: hshahinian86@gmail.com with the subject line Access to UNCC MATLAB codes. Below is a short guide on how the codes should be used. Each directory containing the codes has the main scripts as well as external functions.

D.1 Zygo Fizeau Measurement Data Processor (.dat)

This script and its sub functions provide tools for reading .dat measurement files from the Zygo Verifire AT1000. The key scripts are the following three:

Fizeau_p: This script contains the parameters associated with the processing of data. One of the critical parameters is the diameter of the measured optic (for lateral calibration purposes). The assumption is the sample is circular and it is fully within the FOV of the instrument. The other critical parameter is whether filtering is needed, and the low pass and high pass cut-offs associated with the filtering.

Fizeau_reader_s: Running this script will prompt the user for selecting a .dat file and the codes will start to generate the plots and graph related to the selected files. These graphs include, 3D height map, radial average profile, PSD of the radial average profile, and a diameter trace from the measurement data.

Fizeau_reader: This script is very similar to the previous script with the exception that running the code will ask the user for selecting a directory. Any Fizeau measurement data in that directory will then be processed similarly. It is important to have

a numbering index in the file name spaced with the ‘_’ character. That way the code will associate a number accordingly to each measurement, which will be very handy for further processing and/or comparison of the results.

D.2 Subtractor

This code is used for subtracting measurement interferogram of a sample post and pre-polishing. This script should be used after the `Fizeau_reader` script has been run in advance. Once the data are processed and produced from the `Fizeau_reader` code, the index number of the data that going to be subject to subtraction should be specified in this script. This index is the variable `iter`. So, for instance, for `iter=3`, the measurement data with the index 2 will be subtracted from the measurement data with the index 3. The subtraction involves finding the angle which the two samples were measured on the instrument. For details of this operation look at Chapter 5.

D.3 Zygo SWLI Measurement Data Processor (.dat)

The group of codes set forth below are for the analysis of measured data on the Zygo ZeGage SWLI and Zygo NewView SWLI.

`SWLI_p`: Similar to the codes described in C.1, this script contains the main constant parameters for processing the measurement files. These parameters include form removal degree, filtering type and cutoffs, and also the FOV of the objective for lateral calibration of the data. Furthermore, statistical parameters for quantitative analysis of the data can also be specified in this script. By default, 4 height parameters are scripted and ready as an external function to be called out. If any additional parameters are needed the function should be written.

`SWLI_reader_s`: Again, similar to the section C.1, running this script will prompt the user for selection of a single measurement file. The code will then call the appropriate external functions for reading the data and importing it as matrix. The proper form removal, filtering and spike clipping will be carried out, and finally graphs and statistical parameters are created.

`SWLI_reader_s`: This code has a very similar function as the one given above. The only difference is that this script will prompt the user for selecting a directory that contains SWLI measurement data. The processing is then applied to all the available data within the selected directory.

D.4 Profilometer Measurement Data Processor (.MOD)

This group of scripts, process the Talysurf/OptiTrace profilometer measurement data. The Talysurf data file extracted from the instrument should be with the “.MOD” file extension, whereas the OptiTrace profilometer has files with the “.nc” extension.

The codes follow the same trend for reading Fizeau and SWLI measurement data, where both single file and group file processors are available.

`Profilometer_p`: This script includes the constant parameters used for importing the data into MATLAB. Some of these parameters are file extension, filtering, form removal degree, data height scale, and if need for calculation of MR is needed.

`Profilometer_reader_s`: This script is the single file processor, whereby the user will be asked to select a file depending on the file extension specified in the previous script. The code will then call a variety of functions to do multiple operations. Some of these operations include form removal, manual removal of regions of data that are outlier, and also calculation of MR if the measurement contains reference zones, whereby can be

used for that purpose. The operations also provide the PSD of the data as well as the plot for the PSD.

`Profilometer_reader`: Very similar to the previous script, running this code will prompt the user for selection of a directory that has multiple `.MOD` or `.nc` measurement files. The code will apply all the operations detailed above on the measurements and will produce the relevant graphics thereof.

D.5 Convolution code

The convolution code is used for prediction of material removal from an optic given the spot is known. The spot can be created from measurements obtained on the Fizeau interferometer and or mechanical profilometers. As mentioned in Chapter 5 the measured data is radially averaged. The radially averaged profile is the rotated about the center of the tool and a 3D tool footprint, is whereby, generated.

Appendix E: Publications, Patent, and Presentations

E.1 Publications from Dissertation Work

Hossein Shahinian, Mohammed Hassan, Harish Cherukuri, and Brigid A. Mullany, "Fiber-based tools: material removal and mid-spatial frequency error reduction," *Appl. Opt.* 56, 8266-8274 (2017)

Hossein Shahinian, Harish Cherukuri, and Brigid Mullany, "Evaluation of fiber-based tools for glass polishing using experimental and computational approaches," *Appl. Opt.* 55, 4307-4316 (2016)

Hossein Shahinian and Brigid Mullany, "Fiber Based Polishing Tools for Optical Applications," in *Optical Design and Fabrication 2017* (Freeform, IODC, OFT), OSA Technical Digest (online) (Optical Society of America, 2017), paper OTu2B.4.

Hossein Shahinian, Brigid Mullany, *Optical Polishing Using Fiber Based Tools*, In *Procedia CIRP*, Volume 45, 2016, Pages 183-186, ISSN 2212-8271.

Hossein Shahinian, Mohammed Hassan, Harish Cherukuri, and Brigid A. Mullany, "Fiber Based Tools for Precision Polishing Applications." In *ASPE 32nd annual meeting*, Charlotte, NC, USA. 2017.

E.2 Presentations on Dissertation Work

Center for Freeform Optics (CeFO) IAB meeting, in May 2014, Nov 2014, June 2015, Dec 2015, June 2016, Nov 2016

3rd CIRP conference on Surface Integrity, Charlotte, NC, USA, June 2016

UNCC Mechanical Engineering and Engineering Science PhD symposium, Dec 2016

UNCC Graduate Research Symposium, Feb 2017

OSA Optical Design and Fabrication Congress, Denver, CO, USA, July 2017

E.3 Patent

Brigid Mullany, Hossein Shahinian. *Fiber Based Finishing Tools*. US Patent Application No. 15/723,372. October 2017.

E.4 Other Publications in UNCC

Brigid Mullany, Hossein Shahinian, Jayesh Navare, Farzad Azimi, Eric Fleischhauer, Peter Tkacik, & Russel Keanini, (2017). The application of computational fluid dynamics to vibratory finishing processes. *CIRP Annals-Manufacturing Technology*.

Russel Keanini, Peter Tkacik, Eric Fleischhauer, Hossein Shahinian, Jody Sholar, Farzad Azimi, & Brigid Mullany, B. (2017). Macroscopic liquid-state molecular hydrodynamics. *Scientific Reports*, 7, 41658.

Jerry Dahlberg, Peter T. Tkacik, Brigid Mullany, Eric Fleischhauer, Hossein Shahinian, Farzad Azimi, Jayesh Navare, Spencer Owen, Tucker Bisel, Tony Martin, Jodie Scholar, Russell G. Keanini (2017). An Analog Macroscopic Technique for Studying Molecular Hydrodynamic Processes in Dense Gasses and Liquids. *Journal of Visual Experiments*, to be Published

Clark Hovis, Zachary Reese, Hossein Shahinian, and Christopher Evans, " Observations on Stitching Interferometry on Parts with Radically Different Surface Topographies." In ASPE 32nd annual meeting, Charlotte, NC, USA. 2017.

Hossein Shahinian, Todd Noste, Nicholas Sizemore, Clark Hovis, Prithviraj Shanmugam, Nicholas Horvath, Dustin Gurganos, "See-through smart glass with adjustable focus." to be published in the proceedings of the SPIE Photonics Europe 2018